Excited State Photoemission Momentum Mapping of Organic Molecules from Time-Dependent Density Functional Theory

Masterarbeit

zur Erlangung des akademischen Grades eines
Master of Science

an der Karl-Franzens-Universität Graz und der Technischen
Universität Graz

vorgelegt von
Hodžić, Melvin, BSc

Betreuer: Puschnig Peter, Univ.-Prof. Dr.

Graz, 2024

Acknowledgement

I would like to express my sincere gratitude to my supervisor, Peter Puschnig, for his guidance, valuable insight, and time invested throughout the course of this thesis. Further, I am deeply grateful to my colleagues Christian Kern, Andreas Windischbacher, Dominik Brandstetter, Siegfried Kaidisch, Masoud Hamidi and Diana Shakirova for our engaging discussions, both on- and off-topic. A heartfelt thank you to my friends Paul Schnabl, Nina Kainbacher, Barbara Messner, Markus Baier, and Christoph Schuster. Meeting them thanks to studying physics has made this journey infinitely more enjoyable. And last but certainly not least, I am profoundly thankful to my parents and my sister Enela for their constant and unwavering support. Hvala vam svima!

Abstract

In photoemission orbital tomography (POT), one measures the angular-distribution of the photoelectron intensity of oriented organic molecules and interprets these so-called momentum maps as the Fourier transform of the molecular orbital from which the electron has been emitted. Recently, photoemission orbital tomography has been extended to not only describe electron emission from the electronic ground state, but from optically excited states, so-called excitons. This approach, dubbed exPOT [Phys. Rev. B. 108, 085132 (2023)] allows to visualize, in momentum space, the dynamics of excited states in molecular systems in real time by measuring the angle-resolved momentum distribution of photoelectrons ejected by a laser pulse in the extreme ultraviolet.

In this work, we validate the exPOT formalism for a series of organic molecules. Specifically, we focus on organic molecules that exhibit excited states which are characterized by a transition density matrix containing more than one dominant contribution. To this end, we introduce a computationally efficient prescreening method to identify candidate molecules exhibiting such non-trivial excited states. For a chosen set out of these molecules, we solve Casida's equation to quantify the particle-hole contributions, which enables the application of exPOT to compute momentum maps. These findings are cross-checked by directly simulating pump-probe angle-resolved photoemission spectroscopy using time-dependent density functional theory. Thereby, we confirm the predictions of exPOT for excitons with multiple contributions in the transition density matrix in terms of the energy and momentum distribution of the resulting photoemission signatures.

Zusammenfassung

Photoemissions-Orbitaltomographie (POT) misst die Winkelverteilung der Photoelektronenintensität von orientierten organischen Molekülen und interpretiert diese sogenannten Impulskarten als Fourier-Transformation des Molekülorbitals, aus dem das Elektron emittiert wurde. Kürzlich gelang es die Photoemissions-Orbitaltomographie zu erweitern, so dass nicht nur die Elektronenemission aus dem elektronischen Grundzustand, sondern auch aus optisch angeregten Zuständen, sogenannten Exzitonen, beschrieben werden kann. Dieser Ansatz, genannt exPOT [Phys. Rev. B. 108, 085132 (2023)], ermöglicht es, die Dynamik angeregter Zustände in molekularen Systemen in Echtzeit im Impulsraum zu visualisieren, indem die winkelaufgelöste Impulsverteilung von Photoelektronen gemessen wird, die durch einen Laserpuls im extremen Ultraviolettbereich emittiert werden.

In dieser Arbeit validieren wir den exPOT-Formalismus für eine Reihe organischer Moleküle. Insbesondere konzentrieren wir uns auf organische Moleküle, die angeregte Zustände aufweisen, die durch eine Übergangsdichtematrix gekennzeichnet sind, die mehr als einen dominanten Beitrag enthält. Zu diesem Zweck führen wir eine numerisch effiziente Vorauswahlmethode ein, um Kandidatenmoleküle zu identifizieren, die geeignete, das heißt, nicht-triviale angeregte Zustände aufweisen. Für einen ausgewählten Satz dieser Moleküle lösen wir anschließend die Casida-Gleichung, um die Teilchen-Loch-Beiträge zu quantifizieren, was die Anwendung von exPOT zur Berechnung von Impulskarten ermöglicht. Diese Ergebnisse werden durch direkte Simulation der winkelaufgelösten Pump-Probe-Photoemissionsspektroskopie unter Verwendung der zeitabhängigen Dichtefunktionaltheorie gegengeprüft. Dadurch bestätigen wir die Vorhersagen von exPOT für Exzitonen mit mehreren Beiträgen in der Übergangsdichtematrix in Bezug auf die Energie- und Impulsverteilung der resultierenden Photoemissionssignaturen.

Contents

1   Introduction

The emergence of photoemission orbital tomography (POT) has transformed our ability to bridge theory and experiment in understanding the electronic structure of organic molecular layers [1, 2, 3]. In this technique, momentum maps, the angular dependence of the photoelectron intensity at constant initial state binding energy, are linked to the Fourier transform of the electron-emitting molecular orbitals. This provides a direct connection between angle-resolved photoemission spectroscopy (ARPES) experiments and theoretical models. ARPES thus serves as the backbone of POT, revealing the momentum-resolved electronic structure of thin films and organic interfaces.

POT has been successfully applied to explore a range of phenomena, from charge transfer mechanisms at organic/metal interfaces [4] and the aromaticity of large π-conjugated molecules [5]. However, its extension to optically excited states has remained a challenge. Recent advances in femtosecond pump-probe ARPES have made it possible to track the momentum distribution of optically excited electrons in real-time, thereby opening new avenues for studying ultrafast electron dynamics [6]. To address this gap, a simple approach that describes the excited state momentum map as the Fourier transform of the coherent sum of the electronic part of the exciton wave function. This recently proposed approach is called exPOT and provides a theoretical link between the momentum maps and exciton structures [7]. In this thesis, we validate this approach for a series of organic molecules in the gas phase by directly simulating the optical excitation and the subsequent photoemission within real-time time-dependent density functional theory. In particular, we investigate molecules, which exhibit excited states characterized by a superposition of several single-particle transitions, as this allows to demonstrate the full potential of exPOT. In order to find suitable candidate molecules, we develop a prescreening method based on ground state density functional theory (DFT) properties, which enables the prediction of exciton structures described by particle-hole contributions with low computational cost.

The thesis is organized as follows. Initially, the methods used throughout this thesis are outlined. This includes an introduction to DFT together with essential approximations to exchange-correlation functionals. Next, an overview of time-dependent density functional theory (TDDFT) is given as a framework for modeling excited states in the real-time (RT-TDDFT) fashion but also linear response (LR-TDDFT) regime by addressing Casida's equation. This is followed up by the theoretical description of photoemission introducing the exPOT formalism, natural transition orbitals (NTOs) and the time-dependent surface flux method to capture angle-resolved photoemission. The chapter is concluded with a brief discussion of group theory and transition dipole moments explaining the role of molecular symmetry and selection rules in electronic transitions.

Then, we focus on the development of the prescreening method. By using information that is readily available from ground state DFT computations, such as the symmetry of Kohn-Sham orbitals, transition dipole moments, and energy differences between occupied and unoccupied orbitals, we examine the properties of excited states that feature a mixing of electron transitions. Focusing on molecules

in the gas phase, we apply this method to small organic molecules consisting of less than 40 atoms. In this process, we select molecules with large energy differences between the orbitals involved in the transition and distinguishable momentum map features for further analysis. The chosen molecules are suitable for momentum map calculations, given their manageable computational requirements and experimental practicality.

Subsequently, we solve Casida's equation to obtain the optical absorption spectra and exciton compositions of the selected molecules. Two methods are employed for the calculation of optical spectra: real-time time-dependent density functional theory (RT-TDDFT) and linear response time-dependent density functional theory (LR-TDDFT). In RT-TDDFT, the system is perturbed by a δ-pulse and allowed to evolve over time, while in LR-TDDFT, Casida's equation is solved directly to obtain the excitation spectra. Convergence tests are conducted to ensure the reliability of both methods, and their results are compared to ensure consistency.

Eventually, we use the calculated exciton contributions to compute momentum maps employing the exPOT formalism and validate these predictions using RT-TDDFT simulations of angle-resolved photoemission spectra performed within the time-dependent surface flux (t-SURFF) framework. This method describes the photoemission process without assumptions on the final state, by modeling the flux of emitted electrons as they are tracked through a detector surface. By comparing these two computational approaches, we confirm that the excited molecular states correspond to a superposition of multiple single-particle excitations. This highlights the importance of exPOT for future studies on ultrafast electron dynamics in organic molecules. By linking ARPES, POT, and TDDFT, we aim to further our understanding of exciton dynamics and contribute to the emerging field of "orbital cinematography", which promises to reveal real-time electron movement in molecular systems.

2 Theory

2.1 Density Functional Theory

This chapter provides a concise overview of density functional theory (DFT) to familiarize the reader with the fundamental terminology used throughout this thesis. For a more comprehensive introduction, the devoted readers are referred to the literature [8, 9, 10, 11].

2.1.1 Introduction to Density Functional Theory

The electronic and optical properties of matter are fundamentally determined by the behavior of electrons, which must be described using quantum mechanics. At the molecular level, the quantum state of a system containing N electrons is governed by the Hamiltonian operator

$$\hat{H} = \hat{T} + \hat{U} + \hat{V}, \tag{1}$$

with the kinetic energy part

$$\hat{T} = \frac{1}{2} \sum_{i=1}^{N} \hat{p}_i^2, \tag{2}$$

the Coulomb interaction

$$\hat{U} = \sum_{j>i}^{N} \frac{1}{|\mathbf{r}_i - \mathbf{r}_j|}, \tag{3}$$

and the external potential

$$\hat{V} = \sum_{i=1}^{N} v(\mathbf{r}_i). \tag{4}$$

Many-body quantum mechanics is typically expressed through the wave function $\Psi(\mathbf{r}_1, \mathbf{r}_2, \ldots, \mathbf{r}_N)$. Formally, possible wave functions are given as the eigenfunctions of the non-relativistic, stationary, and non-magnetic N-electron Schrödinger equation

$$\hat{H}\Psi = E\Psi. \tag{5}$$

Although the wave function contains all the necessary information, no closed-form solution exists for systems with more than one electron. Moreover, the complexity of the problem increases exponentially with the number of electrons, and for $N \gtrsim 10^3$, the wave function approach becomes an insufficient theoretical description [12].

In DFT, on the contrary, the electron density corresponding to the ground state wavefunction, Ψ_0, is employed as the primary variable, which reduces the number of spatial coordinates from $3N$ to 3 and the complexity of the problem from 3^N to N^3 :

$$n_0(\mathbf{r}) = n \int d\mathbf{r}_2 \cdots \int d\mathbf{r}_N \, |\Psi_0(\mathbf{r}, \mathbf{r}_2, \ldots, \mathbf{r}_N)|^2. \tag{6}$$

For the electronic ground state of a finite system of interacting electrons, Hohenberg and Kohn demonstrated in 1964 that a one-to-one correspondence exists between the external potential $v(\mathbf{r})$ and the ground state electron density $n(\mathbf{r})$ [13]. This result indicates that all observables can be expressed as functionals of the ground state electron density. The significant advancement in DFT was achieved with the work of Kohn and Sham, who provided a practical methodology for approximating the ground state electron density [14]. As the Hohenberg-Kohn theorem is valid for any form of the electron-electron interaction, one could theoretically consider a scenario with zero interaction, i.e., $U = 0$. The Kohn-Sham (KS) approach constructs a system of N non-interacting electrons that effectively approximates the interacting system. This KS system is described by the following Hamiltonian:

$$\hat{H}_{\mathrm{KS}} = \hat{T}_{\mathrm{KS}} + \hat{V}_{\mathrm{KS}} = \sum_{i=1}^{N} \left(\frac{\hat{p}_i^2}{2} + v_{\mathrm{KS}}(\mathbf{r}_i) \right) \tag{7}$$

Here, it is essential that the non-interacting system is constructed in a way to yield the same ground state electron density as the interacting system. The ground state of this non-interacting system can be expressed as a Slater determinant

$$\Psi_0(x_1, \ldots, x_N) = \frac{1}{\sqrt{N!}} \begin{vmatrix} \varphi_N(\mathbf{r}_1) & \varphi_N(\mathbf{r}_2) & \cdots & \varphi_N(\mathbf{r}_N) \\ \vdots & \vdots & \ddots & \vdots \\ \varphi_1(\mathbf{r}_1) & \varphi_1(\mathbf{r}_2) & \cdots & \varphi_1(\mathbf{r}_N) \end{vmatrix}. \tag{8}$$

The KS orbitals φ_i need to satisfy the one-body Schrödinger equation

$$\hat{H}_{\mathrm{KS}}\varphi_i(\mathbf{r}) = \epsilon_i\varphi_i(\mathbf{r}), \tag{9}$$

and allow the calculation of the ground state density

$$n_{\mathrm{KS}}(\mathbf{r}) = \sum_j |\varphi_j(\mathbf{r})|^2. \tag{10}$$

As it is required that the KS system must replicate the exact ground state electron density, the potential v_{KS} needs to be adjusted. In essence, the distinction between the interacting and non-interacting electron systems, and thus all many-body effects, must be incorporated into the difference between v and v_{KS}. Thereby, a connection between the two systems can be established through the ground state energy of the interacting system

$$\begin{aligned} E[n] &= \langle \Psi[n] | \hat{T} + \hat{U} + \hat{V} | \Psi[n] \rangle \\ &= \hat{T}[n] + \hat{U}[n] + \int \mathrm{d}^3r\, n(\mathbf{r})v(\mathbf{r}) \\ &= \hat{T}_{\mathrm{KS}}[n] + \int \mathrm{d}^3r\, n(\mathbf{r})v(\mathbf{r}) + E_H[n] + E_{xc}[n]. \end{aligned} \tag{11}$$

Hereby, we define the exchange-correlation energy as the crucial quantity that accounts for the differences between the true interacting electron system and the non-interacting Kohn-Sham system. Specifically, it accounts for the difference between

the true kinetic energy T and the Kohn-Sham kinetic energy T_{KS}, as well as the electron-electron interactions beyond the mean-field approximation, where the latter is described by the Hartree energy

$$E_H[n] = \frac{1}{2} \int \mathrm{d}^3r\, \mathrm{d}^3r'\, \frac{n(\mathbf{r})n(\mathbf{r}')}{|\mathbf{r} - \mathbf{r}'|}. \tag{12}$$

With that, it is now possible to calculate the total ground state energy as a functional of a density, which in turn is obtained from single-particle orbitals. Further, provided E_{xc} is known, this framework represents an exact mapping of the many-body problem onto an effective single-particle system. In practice, the ground state density can then be obtained self-consistently from the KS scheme:

1. Begin with an initial guess for the density $n^{(0)}$.

2. Calculate $v_{\mathrm{KS}}^{(0)}[n]$.

3. Construct the KS Hamiltonian $H_{\mathrm{KS}}^{(0)}$.

4. Solve the KS equations $H_{\mathrm{KS}}^{(0)}\varphi_i^{(1)} = \epsilon_i \varphi_i^{(1)}$.

5. Compute the electron density $n^{(1)} = \sum_i |\varphi_i^{(1)}|^2$ and the total energy $E_{\mathrm{tot}}^{(1)}$.

This procedure is repeated until a convergence criterion, e.g. $\epsilon = \left| E_{\mathrm{tot}}^{(j)} - E_{\mathrm{tot}}^{(j-1)} \right|$, is met. However, as the exact form of E_{xc} is not known, we are limited to approximations for exchange-correlation effects, which are discussed in the following section.

2.1.2 Exchange-Correlation Functionals

The KS approach establishes a theoretical framework for determining the electronic structure based on the electron density, but to apply it effectively, an approximation for the exchange-correlation energy or its corresponding potential, as specified in Eq. 11, must be developed. The first and simplest example, already proposed by Kohn and Sham, is called local density approximation (LDA) [13]. This name stems from the assumption that for a slowly varying density the exchange-correlation functional at each point in space depends only on the local electron density, treating each point as if it is part of the homogeneous electron gas (HEG). It can be written as an integral over the exchange and correlation components of the HEG energy per electron [11]:

$$E_{\mathrm{xc}}^{\mathrm{LDA}}[n] = \int \mathrm{d}^3r\, n(\mathbf{r}) \left(e_{\mathrm{x}}^{\mathrm{HEG}}[n] + e_{\mathrm{c}}^{\mathrm{HEG}}[n] \right) = \int \mathrm{d}^3r\, n(\mathbf{r}) \left(-\frac{3}{4\pi} \frac{(9\pi/4)^{1/3}}{\mathbf{r}_s} + e_{\mathrm{c}}^{\mathrm{HEG}}(n(\mathbf{r})) \right).$$
$$\tag{13}$$

Results obtained using the LDA approximation often show unexpectedly good agreement with experimental data, even for non-metallic systems with electronic structures that significantly deviate from the uniform electron gas model. In this work its

time-dependent counterpart, the adiabatic LDA, plays a vital role and is presented in Sec. 2.2.1.

However, to improve upon the LDA, several steps for a better description of exchange-correlation effects can be undertaken. This hierarchy of approximations is often referred to as Jacob's ladder of DFT, where the first rung is represented by the LDA [15]. The next rung on Jacob's ladder is the generalized gradient approximation (GGA), which extends beyond the local density by also considering the density's spatial gradient, which may be written as:

$$E_{\text{xc}}^{\text{GGA}}[n] = \int \text{d}^3r\, n(\mathbf{r}) F_{\text{xc}}\left(n(\mathbf{r}), \nabla n(\mathbf{r})\right). \tag{14}$$

The most widely-used functional in this framework is the formulation of Perdew, Burke and Ernzerhof [16] with more accurate predictions of binding energies and ionization energies for molecules.

A major limitation of local and semi-local exchange-correlation functionals like LDA and PBE is their inaccurate prediction of energy levels. This issue can be mitigated by incorporating a fraction of Fock-exchange, also known as exact-exchange from Hartree-Fock theory, into the DFT energy expression as

$$E_x^{\text{HF}} = -\sum_{j>i} \int \text{d}^3r\, \text{d}^3r'\, \frac{\varphi_i^*(\mathbf{r})\varphi_j^*(\mathbf{r}')\varphi_j(\mathbf{r})\varphi_i(\mathbf{r}')}{|\mathbf{r} - \mathbf{r}'|}. \tag{15}$$

Various functionals arise through different mixing ratios of semi-local exchange-correlation functionals with exact exchange, with one of the most common being B3LYP [17]:

$$E_{xc}^{\text{B3LYP}} = (1 - \alpha)E_x^{\text{LDA}} + \alpha E_x^{\text{HF}} + \beta E_x^{\text{B88}} + \gamma E_c^{\text{LYP}} + (1 - \gamma)E_c^{\text{LDA}} \tag{16}$$

with $\alpha = 0.2$, $\beta = 0.72$, $\gamma = 0.81$, and the GGA functionals E_x^{B88} from Becke [18] and E_c^{LYP} from Lee, Yang, and Parr [19]. However, including Fock-exchange increases the computational cost as solving the two-body integrals is expensive and scales quadratically with the size of the system. Heyd, Scuseria, and Ernzerhof (HSE) [20] proposed a solution to this issue by modifying the Coulomb interaction

$$\frac{1}{r} \rightarrow \frac{1 - \text{erf}(\omega r)}{r} + \frac{\text{erf}(\omega r)}{r} \tag{17}$$

with the help of the error function

$$\text{erf}(x) = \frac{2}{\sqrt{\pi}} \int_0^x \text{d}x'\, e^{-x'^2}. \tag{18}$$

Eq. 17 can now be evaluated using distinct exchange-correlation methods for each term, incorporating an effective range-separation parameter ω to control the spatial range at which Fock exchange is included. This approach reduces the computational complexity by minimizing the number of non-local integrals that must be computed. The HSE energy functional is expressed as

$$E_x^{\text{HSE}}(\omega) = (1 - \alpha)E_x^{\text{PBE,SR}}(\omega) + \alpha E_x^{\text{HF,SR}}(\omega) + E_x^{\text{PBE,LR}}(\omega) + E_c^{\text{PBE}}, \tag{19}$$

where PBE is used for both the long-range exchange energy and the correlation energy. In progressing from B3LYP to HSE, we move from a global hybrid functional to a range-separated hybrid (RSH) functional, with α and ω serving as parameters that govern the mixing and separation of exchange contributions.

2.2 Time-dependent Density Functional Theory

In this section we extend density functional theory to the time-dependent regime and show how time-dependent external potentials can be used to take into account light-matter interaction. For further details on the following discussion, please refer to [21, 22, 23].

2.2.1 Introduction to Time-dependent Density Functional Theory

For a system of N electrons under the influence of a time-dependent potential $v(\mathbf{r}, t)$, the potential operator is given by

$$\hat{V}(t) = \sum_{i=1}^{N} v(\mathbf{r}_i, t) \tag{20}$$

Thus, the Hamiltonian $\hat{H}(t)$ becomes explicitly time-dependent. Consequently, we seek a solution to the time-dependent many-body Schrödinger equation (SE):

$$i\frac{\partial}{\partial t}\Psi = \hat{H}(t)\Psi \tag{21}$$

For similar reasons as in the static case, we aim to replace the many-body wavefunction $\Psi(\{\mathbf{r}_i\}, t)$ with the electron density $n(\mathbf{r}, t)$ and introduce single-particle Kohn-Sham orbitals $\varphi_i^{\text{KS}}(\mathbf{r}, t)$, analogous to ground state DFT. While the Rayleigh-Ritz variational principle can be used to ensure that the density is a valid replacement in the static case, this is not possible for the time-dependent case.

Runge-Gross Theorem

The proof of the one-to-one correspondence between time-dependent potentials and densities, up to a time-dependent additive term, was given by Runge and Gross [23]. This theorem replaces the Hohenberg-Kohn theorems in TD-DFT and establishes that the external potential $v(\mathbf{r}, t)$ is uniquely determined by the density $n(\mathbf{r}, t)$, for a given initial state Ψ_0 at time t_0, which will be summarized in the following.

Consider the Heisenberg equation of motion for the expectation value $j(\mathbf{r}, t)$ of the current-density operator $\hat{J}(\mathbf{r})$:

$$j(\mathbf{r}, t) = \langle \Psi(t)|\hat{J}(\mathbf{r})|\Psi(t)\rangle \tag{22}$$

with

$$\hat{J}(\mathbf{r}) = -\frac{i}{2}\sum_{i=1}^{N}\left[\nabla_i\delta(\mathbf{r} - \mathbf{r}_i) + \delta(\mathbf{r} - \mathbf{r}_i)\nabla_i\right]. \tag{23}$$

This leads to

$$\frac{\partial}{\partial t}j(\mathbf{r}, t) = i\langle\Psi(t)|[\hat{H}, \hat{J}(\mathbf{r})]|\Psi(t)\rangle. \tag{24}$$

Assuming two external potentials $v(\mathbf{r}, t)$ and $v'(\mathbf{r}, t)$ differ by more than a time-dependent term

$$w(\mathbf{r}, t) := v(\mathbf{r}, t) - v'(\mathbf{r}, t) \neq w(t), \tag{25}$$

and further assuming a common initial state Ψ_0, we have

$$\frac{\partial}{\partial t}\left(j(\mathbf{r}, t) - j'(\mathbf{r}, t)\right)\bigg|_{t=t_0} = i\langle\Psi_0|[v(\mathbf{r}, t) - v'(\mathbf{r}, t), \hat{J}(\mathbf{r})]|\Psi_0\rangle = n(\mathbf{r}, t_0)\nabla w(\mathbf{r}, t_0). \tag{26}$$

If the condition in Eq. 25 is satisfied, the two current densities will evolve differently for $t > 0$. Using the continuity equation

$$\frac{\partial}{\partial t}n(\mathbf{r}, t) = -\nabla j(\mathbf{r}, t), \tag{27}$$

we can express the result from Eq. 26 in terms of the electron density as

$$\frac{\partial^2}{\partial t^2}[n(\mathbf{r}, t) - n'(\mathbf{r}, t)]\bigg|_{t=t_0} = -\nabla[n(\mathbf{r}, t_0)\nabla w(\mathbf{r}, t_0)] \tag{28}$$

To demonstrate that the right-hand side of Eq. 28 cannot vanish under the assumption of Eq. 25, we consider the integral

$$\int d^3r\, w(\mathbf{r}, t)\nabla\cdot[n(\mathbf{r}, t_0)\nabla w(\mathbf{r}, t)] = \int d^3r\, \nabla\cdot[w(\mathbf{r}, t)n(\mathbf{r}, t_0)\nabla w(\mathbf{r}, t)] - \int d^3r\, n(\mathbf{r}, t_0)[\nabla w(\mathbf{r}, t)]^2. \tag{29}$$

The first term on the right can be rewritten as a surface integral using Gauss's theorem, which vanishes for reasonable densities that decay sufficiently fast. The second term has a strictly positive integrand, meaning the right-hand side of Eq. 28 cannot vanish. This confirms that the densities for two different external potentials evolve differently, supporting the one-to-one mapping $n \to v$ promised by the Runge-Gross theorem. However, this only proves the uniqueness, not the existence, of the external potential for a given density. This concern is known as the "v-representability problem" [22], which, howeverm turns out not to limit practical applications of the Runge-Gross theorem.

Time-dependent Kohn-Sham Equations

In analogy to the static case, we introduce a Kohn-Sham system of N non-interacting electrons influenced by a potential $v_{\mathrm{KS}}[n_{\mathrm{KS}}, \Phi_0](\mathbf{r}, t)$, which yields an identical electron density $n_{\mathrm{KS}}(\mathbf{r}, t)$ as the fully interacting system:

$$n_{\mathrm{KS}}(\mathbf{r}, t) = \sum_{i=1}^{N}|\varphi_i(\mathbf{r}, t)|^2. \tag{30}$$

These time-dependent Kohn-Sham orbitals $\varphi_i(\mathbf{r}, t)$ then satisfy the time-dependent Schrödinger equations

$$i\frac{\partial}{\partial t}\varphi_i(\mathbf{r}, t) = \left(-\frac{1}{2}\nabla^2 + v_{\mathrm{KS}}[n_{\mathrm{KS}}, \Phi_0](\mathbf{r}, t)\right)\varphi_i(\mathbf{r}, t), \tag{31}$$

where the potential depends on the initial state Φ_0, typically constructed from single-particle wavefunctions via a Slater determinant as in Eq. 8. The time-dependent Kohn-Sham (TDKS) potential can be expressed as

$$v_{\text{KS}}[n_{\text{KS}}, \Psi_0, \Phi_0](\mathbf{r}, t) = v(\mathbf{r}, t) + \int d^3 r' \frac{n_{\text{KS}}(\mathbf{r}', t)}{|\mathbf{r} - \mathbf{r}'|} + v_{xc}[n_{\text{KS}}, \Psi_0, \Phi_0](\mathbf{r}, t). \quad (32)$$

All entities present in the TDKS potential are functionals of the time-dependent density $n(\mathbf{r}, t)$, except for the external potential $v(\mathbf{r}, t)$. Similar to ground state DFT, the equation defines the time-dependent exchange-correlation potential v_{xc}, as v_{KS} must reproduce the same time-dependent density as the fully interacting system.

In real-time TD-DFT, the initial state Φ_0 is obtained from a converged DFT ground state calculation. The individual Kohn-Sham orbitals are then propagated in time according to Eq. 31 using a numerical scheme for the time derivative, eliminating the need for a self-consistency cycle.

Adiabatic Local Density Approximation

Many TDDFT applications rely on the adiabatic approximation of the respective ground state DFT functionals. Given a ground state density $n_0(\mathbf{r})$ and ground state exchange-correlation functional $v_0^{\text{xc}}[n_0](\mathbf{r})$, the adiabatic approximation is defined as

$$v_{\text{xc}}^{\text{a}}(\mathbf{r}, t) = v_{\text{xc}}^0[n_0](\mathbf{r}) \Big|_{n_0 \to n(\mathbf{r}, t)}. \quad (33)$$

This means that the adiabatic exchange-correlation potential depends only on the current density $n(\mathbf{r}, t)$, at a given time t and that there is no memory of the system's past. In this work, the adiabatic local density approximation (ALDA) is used for time-dependent calculations, based on the homogeneous electron gas exchange-correlation energy density

$$v_{\text{xc}}^{\text{ALDA}}(\mathbf{r}, t) = \frac{de_{\text{xc}}^{\text{HEG}}(n)}{dn} \Big|_{n=n(\mathbf{r}, t)}. \quad (34)$$

However, the ALDA inherits the limitations of the static LDA, along with the drawbacks of the adiabatic approximation.

Optical Excitations from Real-Time TDDFT

To explore the electronic response to an electromagnetic perturbation an efficient method is to use a Dirac delta pulse, which instantaneously excites all eigenmodes of the system [24]. In this scenario, the electric field component in the ν-direction, is represented as

$$E_\nu(t) = E_\nu^0 \delta(t). \quad (35)$$

Its Fourier transform

$$E_\nu(\omega) = E_\nu^0 \quad (36)$$

is frequency-independent. The system's response to the pulse can be captured through the polarizability tensor $\alpha_{\mu\nu}(t)$, which relates the induced dipole moment $p_\mu(t)$ in direction μ with the applied electric field:

$$p_\mu(t) = \sum_\nu \alpha_{\mu\nu}(t) E_\nu(t). \tag{37}$$

The tensor's diagonal components capture the response of the induced dipole along the same direction as the applied electric field, while the off-diagonal components describe how perturbations in one direction influence the response in another. In the frequency domain, the polarizability is given by

$$\alpha_{\mu\nu}(\omega) = \frac{1}{E_\nu^0} \int dt\, e^{i\omega t} p_\mu(t), \tag{38}$$

Importantly, the imaginary part of the polarizability $\alpha_{\mu\nu}$ is directly related to the photoabsorption cross-section $\sigma_{\mu\nu}(\omega)$, which provides a direct link to experimental data

$$\sigma_{\mu\nu}(\omega) = \frac{4\pi\omega}{c} \operatorname{Im}\left[\alpha_{\mu\nu}(\omega)\right]. \tag{39}$$

From this approach the excitation spectrum can be efficiently computed, allowing for comparison with experimental photoabsorption measurements.

2.2.2 Linear Response TDDFT

In the framework of DFT, the results of a calculation can include both occupied and unoccupied Kohn-Sham eigenstates, with corresponding eigenenergies ϵ_i from the static Kohn-Sham Hamiltonian $\hat{H}_{\mathrm{KS}}$. However, according to Janak's theorem, these Kohn-Sham eigenvalues do not represent the true excitation energies of the interacting system. Rather, they serve as auxiliary quantities within the DFT formalism, since DFT is fundamentally a ground state theory [?]. Within linear response theory, TD-DFT simulates the dynamics of many-body effects during excitation by describing excited states through time-dependent changes in electron density. In this context, linear response theory refers to the approximation that the electron density responds linearly to small external perturbations, allowing for accurate calculations of excitation energies and transition properties. In the following, we briefly outline linear response TDDFT (LR-TDDFT) [21] and Casida's equation [25], which is widely implemented in quantum chemistry software.

Consider a time-dependent external potential

$$v(\mathbf{r}, t) = v_0(\mathbf{r}) + v_1(\mathbf{r}, t)\theta(t - t_0), \tag{40}$$

where for $t < t_0$, the system experiences only the time-independent potential $v_0(\mathbf{r})$, typically representing the static nuclei's electrostatic influence. At $t = t_0$, the time-dependent potential $v_1(\mathbf{r}, t)$ is applied leading to excitation. Due to the Runge-Gross theorem the electron density can be written as

$$n(\mathbf{r}, t) = n[v_{\mathrm{KS}}](\mathbf{r}, t). \tag{41}$$

For weak perturbations, the density can be expanded in powers of v_1 as

$$n(\mathbf{r}, t) = n_0(\mathbf{r}) + n_1(\mathbf{r}, t) + n_2(\mathbf{r}, t) + \dots \tag{42}$$

The first-order response $n_1(\mathbf{r}, t)$ can be expressed as

$$n_1(\mathbf{r}, t) = \int dt' \int d^4 r' \, \chi_{\text{KS}}(\mathbf{r}, t, \mathbf{r}', t') v_{\text{KS},1}(\mathbf{r}', t'), \tag{43}$$

where $\chi_{\text{KS}}[n_0](\mathbf{r}, t, \mathbf{r}', t')$ is the linear density-density response function:

$$\chi_{\text{KS}}(\mathbf{r}, t, \mathbf{r}', t') = \left. \frac{\delta n[v_{\text{KS}}](\mathbf{r}, t)}{\delta v_{\text{KS}}(\mathbf{r}', t')} \right|_{v_{\text{KS}}[n_0]}. \tag{44}$$

The integral $\int d^4 r$ represents an integration over real space $\mathbf{r}$ and a summation over the spin coordinate σ, $\sum_\sigma \int d^3 r$. The Kohn-Sham potential corresponding to the first-order density response can be written as

$$v_{\text{KS},1}(\mathbf{r}, t) = v_1(\mathbf{r}, t) + \int d^3 r' \frac{n_1(\mathbf{r}', t)}{|\mathbf{r} - \mathbf{r}'|} + v_{\text{xc},1}(\mathbf{r}, t). \tag{45}$$

Here, the first-order exchange-correlation potential $v_{\text{xc},1}(\mathbf{r}, t)$ is expressed as

$$v_{\text{xc},1}(\mathbf{r}, t) = \int dt' \int d^4 r' \, f_{\text{xc}}[n_0](\mathbf{r}, t, \mathbf{r}', t') n_1(\mathbf{r}', t'), \tag{46}$$

and $f_{\text{xc}}[n_0](\mathbf{r}, t, \mathbf{r}', t')$ is the time-dependent exchange-correlation kernel, a functional of the ground state density n_0. This kernel, along with the response function $\chi_{\text{KS}}(\mathbf{r}, t, \mathbf{r}', t')$, depends only on the time difference $t - t'$. Switching to frequency space via Fourier transform introduces the Hartree-xc kernel

$$f_{\text{Hxc}}[n_0](\mathbf{r}, \mathbf{r}', \omega) = \frac{1}{|\mathbf{r} - \mathbf{r}'|} + \int d(t - t') e^{i\omega(t - t')} f_{\text{xc}}[n_0](\mathbf{r}, t, \mathbf{r}', t'). \tag{47}$$

Substituting this into Eq. 43, the expression for the first-order density response, yields

$$n_1(\mathbf{r}, \omega) = \int d^4 r' \, \chi_{\text{KS}}(\mathbf{r}, \mathbf{r}', \omega) \left(v_1(\mathbf{r}', \omega) + \int d^4 r'' \, f_{\text{Hxc}}[n_0](\mathbf{r}', \mathbf{r}'', \omega) n_1(\mathbf{r}'', \omega) \right), \tag{48}$$

which must be solved self-consistently for $n_1(\mathbf{r}, \omega)$ and contains information about the system's resonant frequencies.

Casida's Equation

In Casida's approach a more computationally feasible matrix formulation of the problem in Eq. 48 is achieved by focusing on a finite subspace of occupied or valence, $\varphi_{0,v}$ and unoccupied or conduction, $\varphi_{0,c}$, Kohn-Sham orbitals. This is enabled through the Kohn-Sham response function in frequency space, which in terms of these orbitals is written as

$$\chi_{\text{KS}}(\mathbf{r}, \mathbf{r}', \omega) = \delta_{\sigma, \sigma'} \sum_{v,c} \frac{(f_{c\sigma} - f_{v\sigma}) \varphi_{0,v}(\mathbf{r}) \varphi_{0,c}^*(\mathbf{r}) \varphi_{0,v}^*(\mathbf{r}') \varphi_{0,c}(\mathbf{r}')}{\omega - \omega_{vc\sigma} + i\eta}, \tag{49}$$

where $\omega_{vc\sigma} = \epsilon_{v\sigma} - \epsilon_{c\sigma}$ are the excitation energies of the Kohn-Sham ground state, distinct from the true excitation energies Ω_m, which are given by the poles $\omega = \Omega_m$ in the density response $n_1(\mathbf{r}, \omega)$. Detailed derivations are out of the scope of this work and are provided in the literature [25, 22, 21].

The resonance energies Ω and matrices $\mathbf{X}$ and $\mathbf{Y}$ are obtained by solving the following eigenvalue equation known as Casida's equation

$$\begin{pmatrix} \mathbf{B} & \mathbf{K} \\ \mathbf{K} & \mathbf{B} \end{pmatrix} \begin{pmatrix} \mathbf{X} \\ \mathbf{Y} \end{pmatrix} = \Omega \begin{pmatrix} -1 & 0 \\ 0 & 1 \end{pmatrix} \begin{pmatrix} \mathbf{X} \\ \mathbf{Y} \end{pmatrix} \tag{50}$$

The matrix elements are defined through the real ground state orbitals as

$$B_{vc,v'c'}(\omega) = \delta_{vv'}\delta_{cc'}(\varepsilon_v - \varepsilon_c) + K_{vc,v'c'}(\omega) \tag{51}$$

and

$$K_{vc,v'c'}(\omega) = \int \mathrm{d}^4 r \int \mathrm{d}^4 r' \, \varphi_{0,v}^*(\mathbf{r})\varphi_{0,c}(\mathbf{r}) f_{Hxc}(\mathbf{r}, \mathbf{r}', \omega)\varphi_{0,v'}(\mathbf{r}')\varphi_{0,c'}^*(\mathbf{r}'). \tag{52}$$

Here, the matrices $\mathbf{X}$ and $\mathbf{Y}$ are associated with the particle-hole contributions to the excited states, describing the mixing of states during electronic transitions. Specifically, $\mathbf{X}$ provides information for the forward excitation from occupied to unoccupied states, while $\mathbf{Y}$ represents the reverse process, essential for capturing the configuration interaction that arises from correlated electron motion. In the evaluation of this work, the Tamm-Dancoff approximation is not applied, as both matrices are calculated. However, we only make use of $\mathbf{X}$, which will be referred to as transition density matrix.

The first term in matrix $\mathbf{B}$, $\delta_{vv'}\delta_{cc'}(\epsilon_v - \epsilon_c)$, corresponds to the energy difference between an occupied state v and an unoccupied state c. This component captures the direct contributions of the energy levels to the excitation process. In contrast, the second term, $K_{vc,v'c'}(\omega)$ accounts for the coupling between different excitation modes, arising from the exchange-correlation interactions represented through the kernel f_{Hxc}. This coupling term is critical for accurately incorporating electron-electron interactions that affect the excited-state structure. Note that, the indices v, v' and c, c' label summations over all occupied and unoccupied Kohn-Sham states, respectively, including continuum states. As a result, this leads to an infinite-dimensional eigenvalue problem in theory. However, in practical applications, only a finite number of unoccupied states is considered to ensure computational feasibility.

2.3 Theoretical Description of Photoemission

In this chapter, we explore the theoretical framework underlying the study of photoemission processes, particularly focusing on photoemission angular distributions (PADs). First, the technique named "exPOT" expands photoemission orbital tomography (POT) to study excited states by directly mapping angular distributions from the electronic structures of these excited states [7]. Second, we describe the time-dependent surface flux (t-SURFF) method within real-time TDDFT (RT-TDDFT), which captures outgoing electron waves without assuming a final state [26].

2.3.1 Photoemission from Excitons

In photoemission experiments, both the kinetic energy and momentum of an emitted photoelectron are measured, leading to a three-dimensional data set $I(E_{\text{kin}}, k_x, k_y)$. This data serves as a distinct fingerprint for each electronic state, which is crucial for understanding the electronic structure of molecules. To theoretically describe the photoemission process, we start with Fermi's golden rule

$$W_{i \to f} \propto |\langle \Psi_f^N | \hat{H}_{\text{int}} | \Psi_i^N \rangle|^2 \delta(\omega + E_i^N - E_f^N), \tag{53}$$

which provides the transition probability $W_{i \to f}$ between the initial state Ψ_i^N with energy E_i^N and the final state Ψ_f^N with energy E_f^N of the N-electron system. Next, under the dipole approximation, the interaction Hamiltonian $\hat{H}_{\text{int}}$ simplifies to

$$W_{i \to f} \propto |\langle \Psi_f^N | \mathbf{A} \hat{P} | \Psi_i^N \rangle|^2 \delta(\omega + E_i^N - E_f^N), \tag{54}$$

which is known as the one-step-model of photoemission. For the final state Ψ_f^N, the "sudden approximation" allows to factorize the wavefunction into a free electron γ_k and an $(N-1)$-electron term with a hole in the j-th electronic level, assuming no correlation with the remaining system. With this approximation and through energy conservation, the kinetic energy E_{kin} of the emitted electron is related to the energies of the initial and final states as

$$E_{\text{kin}} = \omega + (E_{i,0}^N - E_{f,j}^{N-1}) = \omega - \varepsilon_j, \tag{55}$$

where ε_j denotes the ionization potential of the j-th state, from which the electron is removed. Further, utilizing the Dyson orbital D_j, which describes the overlap of the initial state and the remaining $(N-1)$ final state, allows us to express the matrix element as

$$\langle \Psi_f^N | \mathbf{A} \hat{P} | \Psi_i^N \rangle = \int d^3r \, \gamma_{\mathbf{k}}^*(\mathbf{r}_N) \, \mathbf{A} \hat{P} \, D_j(\mathbf{r}) \ . \tag{56}$$

As the next crucial step, a free-electron plane wave approximation for $\gamma_{\mathbf{k}}$ is applied, which allows to relate the photoemission intensity $I(\mathbf{k})$ to the Fourier transform of the Dyson orbital via

$$I(\mathbf{k}) \propto |\mathbf{A}\mathbf{k}|^2 \, |\mathcal{F}[D_j](\mathbf{k})|^2 \, \delta(\omega - E_{\text{kin}} - \epsilon_j). \tag{57}$$

This theoretical framework of photoemission facilitates the technique known as photoemission orbital tomography (POT) [1], which effectively combines angle-resolved photoemission data with quantum mechanical predictions, creating a powerful tool for visualizing and understanding electronic states.

Next, we examine the extension of POT to include excitons named "exPOT", expanding its application beyond the study of occupied molecular orbitals through ground-state electron photoexcitation. For a detailed derivation, see [7]. Excitons, which are bound electron-hole pairs, represent fundamental optical excitations occurring below the band gap in molecules and non-metallic solids. The wave function

of the m-th exciton, with excitation energy Ω_m, can be expanded in terms of electron $\{\chi_c(\mathbf{r}_e)\}$ and hole $\{\phi_v(\mathbf{r}_h)\}$ basis states as

$$\Psi_m(\mathbf{r}_h, \mathbf{r}_e) = \sum_{v,c} X_{vc}^{(m)} \varphi_v^*(\mathbf{r}_h) \chi_c(\mathbf{r}_e). \tag{58}$$

Here, $X_{vc}^{(m)}$ represents the transition density matrix as obtained by solving Casida's equation [Eq. 50] which characterizes the exciton. Utilizing the sudden approximation again, one can express the Dyson orbital $D_{j,m}(\mathbf{r})$ that describes electron detachment as

$$D_{j,m}(r) = \sum_{v'} \langle \Psi_{i,m}^N | \hat{a}_{v'}^\dagger | \Psi_{f,j}^{N-1} \rangle \varphi_{v'}(r) + \sum_{c'} \langle \Psi_{i,m}^N | \hat{a}_{c'}^\dagger | \Psi_{f,j}^{N-1} \rangle \chi_{c'}(r). \tag{59}$$

In this equation, $a_v^\dagger$ and a_c are the creation and annihilation operators for a hole in the valence state v and an electron in the conduction state c, respectively. Approximating $\Psi_{i,0}^N$ by a single Slater determinant and taking into account that all integrals in the sum over v' and for $c \neq c'$ vanish due to orthogonality allows to write

$$\begin{aligned}
D_{j,m}(\mathbf{r}) &= \sum_{v,c} X_{vc}^{(m)} \langle \Psi_{i,0}^N | \hat{a}_v^\dagger \hat{a}_c \hat{a}_c^\dagger \hat{a}_j | \Psi_{i,0}^N \rangle \chi_c(\mathbf{r}) \\
&= \sum_c X_{jc}^{(m)} \langle \Psi_{i,0}^N | \hat{a}_j^\dagger \hat{a}_j \hat{a}_c \hat{a}_c^\dagger | \Psi_{i,0}^N \rangle \chi_c(\mathbf{r}) \\
&= \sum_c X_{jc}^{(m)} \chi_c(\mathbf{r}).
\end{aligned} \tag{60}$$

Inserting this into Eq. 53 reduces the photoemission matrix element to

$$\langle \Psi_f^N | \mathbf{A}\hat{P} | \Psi_i^N \rangle \propto (\mathbf{A}\mathbf{k}) F[D_{j,m}](\mathbf{k}). \tag{61}$$

Here, $F[D_{j,m}](\mathbf{k})$ signifies the Fourier transform of the Dyson orbital. The photoemission intensity from the m-th exciton can be obtained by taking energy conservation into account via

$$\omega = E_f^N - E_i^N = E_{f,j}^{N-1} + E_{\text{kin}} - E_0^N - \Omega_m = E_{\text{kin}} + \varepsilon_j - \Omega_m \tag{62}$$

and summing over all possible final hole configurations, resulting in

$$I_m(\mathbf{k}) \propto |\mathbf{A}\mathbf{k}|^2 \sum_j \left| \sum_c X_{jc}^{(m)} F[\chi_c](\mathbf{k}) \right|^2 \delta(\omega - E_{\text{kin}} - \epsilon_j + \Omega_m). \tag{63}$$

This expression, referred to as "exPOT" (exciton POT), predicts that the photoemission signal from a general exciton will exhibit contributions at multiple kinetic energies, consistent with energy conservation and dependent on the hole's position following electron detachment, characterized by the ionization energy ε_j. At each allowed kinetic energy, momentum maps are represented as Fourier transforms of the coherent sum over unoccupied states, weighted by the corresponding transition density matrix elements.

2.3.2 Natural Transition Orbitals

Natural transition orbitals (NTOs) [27] enhance the physical understanding of excitons, particularly in the context of the photoemission intensity for exPOT, as expressed in Eq. 63. Let N_v denote the number of occupied orbitals φ_v and N_c the number of unoccupied, or virtual, orbitals χ_c. Then, the transition density matrix X_{vc} can be represented by a matrix of size $N_v \times N_c$ that can be factorized by means of a singular value decomposition

$$X = V\Lambda C^T. \tag{64}$$

Here, V and C are square matrices of sizes $N_v \times N_v$ and $N_c \times N_c$, respectively, and Λ is a rectangular matrix of size $N_v \times N_c$ with non-zero diagonal elements $\lambda_1, \lambda_2, \ldots, \lambda_{N_v}$. These singular values are ordered by magnitude, satisfying the normalization condition:

$$\sum_{i=1}^{N_v} \lambda_i^2 = 1. \tag{65}$$

Assuming $N_v < N_c$, we define new orbitals $\tilde{\varphi}_\lambda$ and $\tilde{\chi}_\lambda$ via the transformations:

$$\tilde{\varphi}_\lambda = \sum_{v=1}^{N_v} V_{\lambda v}^T \varphi_v, \tag{66}$$

$$\tilde{\chi}_\lambda = \sum_{c=1}^{N_c} C_{\lambda c}^T \chi_c. \tag{67}$$

The exciton wave function can then be expressed in the electron-hole basis as follows:

$$\Psi(\mathbf{r}_h, \mathbf{r}_e) = \sum_{\lambda=1}^{N_v} \Lambda_\lambda \tilde{\varphi}_\lambda^*(\mathbf{r}_h) \tilde{\chi}_\lambda(\mathbf{r}_e). \tag{68}$$

Incorporating Eq. 64 into the photoemission intensity expression from Eq. 63, we can reformulate the exPOT intensity in terms of the NTO basis:

$$I_m(\mathbf{k}) \propto |\mathbf{A}\mathbf{k}|^2 \sum_j \sum_\lambda V_{j\lambda} \Lambda_\lambda |F[\tilde{\chi}_\lambda](\mathbf{k})|^2 \delta\left(\omega + E_{\text{kin}} - \epsilon_j + \Omega_m\right). \tag{69}$$

This transformation simplifies exciton representation using a few significant NTOs, allowing for controlled accuracy by setting a threshold for Λ_λ. NTOs also provide meaningful insights into transition character, enriching the analysis of excited-state photoemission experiments.

2.3.3 Description of Photoemission in RT-TDDFT

In the RT-TDDFT approach, the system is perturbed with an external light field whose frequency lies above the ionization threshold. This leads to the time-dependent emission of charge density into the vacuum, which is detected using a method based on flux integrals. This approach records the photoelectron flux

through a detector surface, placed sufficiently far from the system so that only quasi-free electrons are captured [28]. The flux per unit area provides the photoelectron intensity, which can be described as a function of kinetic energy, parallel momentum, photon energy, and observation time T. This method, named time-dependent surface flux method (t-SURFF), adapted for real-time simulations of photoemission, has been integrated into the OCTOPUS code [29] and applied to both molecular and periodic systems [26, 30]. The photoelectron intensity is expressed as

$$I(\mathbf{k}, \omega, T) = I(E_{\text{kin}}, \mathbf{k}_{\parallel}, \omega, T), \tag{70}$$

where E_{kin} is the kinetic energy, $\mathbf{k}_{\parallel}$ the parallel momentum, and ω the photon energy.

Within an inner region $\mathcal{A}$, where the electrons interact with the light field and the atomic nuclei, the system is governed by the Kohn-Sham (KS) Hamiltonian given by

$$\hat{H}_{\text{KS}}(t) = \frac{1}{2}\left(\hat{p} - \frac{\mathbf{A}(t)}{c}\right)^2 + v_{\text{ext}}(\mathbf{r}, t) + \int d\mathbf{r}' \frac{n(\mathbf{r}', t)}{|\mathbf{r} - \mathbf{r}'|} + v_{\text{xc}}[n](\mathbf{r}, t). \tag{71}$$

In contrast, in an outer region $\mathcal{B}$, where photoelectrons behave as nearly free particles, their motion is described by the Volkov Hamiltonian expressed as

$$\hat{H}_{\text{V}}(t) = \frac{1}{2}\left(\hat{p} - \frac{\mathbf{A}(t)}{c}\right)^2 \tag{72}$$

Therefore, the system is governed by two Hamiltonians depending on the region

$$\hat{H}(t) = \begin{cases} \hat{H}_{\text{KS}}(t) & \text{if } \mathbf{r} \in \mathcal{A}, \\ \hat{H}_{\text{V}}(t) & \text{if } \mathbf{r} \in \mathcal{B}. \end{cases} \tag{73}$$

Assuming that after some time T, the charge density between regions $\mathcal{A}$ and $\mathcal{B}$ becomes spatially separated, the photoelectrons can be described by the analytical solutions of the Volkov Hamiltonian. These solutions take the form of plane waves with an additional phase factor due to the photon field

$$\gamma_{\mathbf{k}}(\mathbf{r}, t) = (2\pi)^{-3/2} e^{i\chi(\mathbf{k}, t)} e^{i\mathbf{k}\cdot\mathbf{r}}, \tag{74}$$

where $\chi(t)$ is the time-dependent phase factor given by

$$\chi(t) = \frac{1}{2}\int_0^t d\tau \left(\mathbf{k} - \frac{\mathbf{A}(t)}{c}\right)^2. \tag{75}$$

In this context, the photoelectrons' wave functions in region B can be expanded as

$$\varphi_j^{\mathcal{B}}(\mathbf{r}, t) = \int dk^3\, b_j(\mathbf{k}, t)\, \gamma_{\mathbf{k}}(\mathbf{r}, t). \tag{76}$$

The density in region $\mathcal{B}$, $n_{\mathcal{B}}(\mathbf{r}, t) = \sum_j |\phi_j^{\mathcal{B}}(\mathbf{r}, t)|^2$, measures the photoelectrons that have passed through the detector surface after time T. The total number of photoelectrons is given by

$$N_{\text{photo}}(T) = \sum_j \int dk^3\, |b_j(\mathbf{k}, T)|^2, \tag{77}$$

and the photoemission intensity can be determined from the momentum- and energy-resolved emission probability. The intensity $I(\mathbf{k})$ is related to the derivative of the number of photoelectrons with respect to $\mathbf{k}$

$$I(\mathbf{k}) \propto \frac{\partial N_{\text{photo}}(T)}{\partial \mathbf{k}}. \tag{78}$$

Alternatively, using the continuity equation, the number of photoelectrons can be expressed as the electron flux through the detector surface $\mathcal{S}$, where the flux is computed from the current density $\mathbf{j}(\mathbf{r}, t)$

$$N_{\text{photo}}(T) = -\int_0^T dt \oint_{\mathcal{S}} d\mathbf{s}\, \mathbf{j}(\mathbf{r}, t). \tag{79}$$

Here, the current density $\mathbf{j}(\mathbf{r}, t)$ is obtained from the current density operator $\hat{J}(t)$ acting on the Kohn-Sham orbitals

$$\mathbf{j}(\mathbf{r}, t) = \sum_j \langle \varphi_j(t) | \hat{J}(t) | \varphi_j(t) \rangle. \tag{80}$$

Substituting this into the flux equation, one can express the photoemission intensity as [30]

$$I(\mathbf{k}) \propto \sum_j \left| \int_0^T dt \oint_{\mathbf{S}} d\mathbf{s}\, \langle \gamma_{\mathbf{k}}(t) | \hat{J}(t) | \phi_j(\mathbf{r}, t) \rangle \right|^2. \tag{81}$$

Thus, the intensity can be interpreted as a measure of the photoelectron flux that has successfully traversed the detector, providing insight into the electronic structure of the system. This framework enables a comprehensive understanding of photoemission processes, linking the theoretical formulation directly to observable quantities in experiments.

2.4 Group Theory and Transition Dipole Moments

Group theory is an essential tool in chemistry and physics for describing the symmetry properties of molecules and their quantum states. In particular, the set of irreducible representations of a given point symmetry group, the so-called character tables, offer a systematic way to analyze how molecular orbitals, vibrations, and electronic transitions behave under various symmetry operations of a particular point group. Character tables are instrumental in determining which molecular transitions, such as dipole transitions, are allowed, and in classifying molecular orbitals based on their symmetry properties [31, 32].

In this section, we will provide an overview of key concepts such as representations, irreducible representations, and reducible representations, and explain how symmetry and group theory can predict allowed dipole transitions. We will use the C_{2h} point group character table as an example [33].

2.4.1 Representations in Group Theory

In group theory, a representation describes how the symmetry operations of a point group can be mapped to matrices or functions that describe the transformation of objects such as molecular orbitals or vibrational modes. These representations are crucial for characterizing the symmetry of quantum states. A reducible representation can be viewed as a composite of simpler, fundamental components known as irreducible representations, abbreviated as irr. rep. A reducible representation can be broken down into irreducible representations, which represent the most basic symmetry properties of a system and cannot be simplified further.

Consider the character table for the C_{2h} point group in Tab. 4 below

Tab. 1: Character table for the C_{2h} point group from [33].

C_{2h}	E	$C_2(z)$	i	σ_h	Pol. Dir.
A_g	1	1	1	1	
A_u	1	1	-1	-1	z
B_g	1	-1	1	-1	
B_u	1	-1	-1	1	x, y

In this table, C_{2h} denotes the point group of the molecule, describing the symmetry operations that leave the molecule unchanged. For C_{2h}, the symmetry operations are E, the identity operation; $C_2(z)$, a 180-degree rotation around the z-axis; i, inversion through the molecular center; and σ_h, reflection through the horizontal mirror plane. The characters, which are the numbers in the table, e.g. 1, -1, indicate how a molecular orbital or wavefunction behaves under each symmetry operation. A character of 1 means the wavefunction is unchanged by the symmetry operation, while a character of -1 means the wavefunction changes sign. The irreducible representations A_g, A_u, B_g, and B_u represent the symmetry properties of molecular orbitals or transitions. The letters A and B indicate whether the representation is symmetric (A) or antisymmetric (B) with respect to the $C_2(z)$ rotation. The subscripts g (gerade) and u (ungerade) refer to symmetry (g) or antisymmetry (u) with respect to inversion. The *Pol. Dir.* column lists the polarization directions associated with the irreducible representations. For example, z indicates that dipole transitions are allowed along the z-axis for irreducible representation A_u, while x and y indicate dipole transitions are allowed in the xy-plane for B_u. In group theory, the reduction of a reducible representation into its constituent irreducible representations is achieved using mathematical techniques like the orthogonality theorem or projection operators. Each irreducible representation corresponds to a specific symmetry behavior under the symmetry operations of the point group.

2.4.2 Transition Dipole Moment and Allowed Transitions

One of the most important applications of character tables is in predicting whether a particular electronic transition is allowed or forbidden based on symmetry. The transition dipole moment between two quantum states, the initial state Ψ_i and the

final state Ψ_f, is defined by

$$\mu_{fi} = \int d^3r \Psi_f^*(\mathbf{r})\,\hat{\mu}\,\Psi_i(\mathbf{r})\ . \tag{82}$$

In this expression, μ_{fi} is the transition dipole moment between the initial state Ψ_i and the final state Ψ_f. The dipole moment operator $\hat{\mu}$ is typically given by $-e\hat{\mathbf{r}}$, where e is the charge of the electron. For each Cartesian direction, the transition dipole moment can be written as a separate integral, depending on the direction of the dipole moment operator, as

$$\mu_{fi}^x = \int d^3r \Psi_f^*(\mathbf{r})\,(-e\hat{x})\,\Psi_i(\mathbf{r})\ , \tag{83}$$

$$\mu_{fi}^y = \int d^3r \Psi_f^*(\mathbf{r})\,(-e\hat{y})\,\Psi_i(\mathbf{r})\ , \tag{84}$$

$$\mu_{fi}^z = \int d^3r \Psi_f^*(\mathbf{r})\,(-e\hat{z})\,\Psi_i(\mathbf{r})\ . \tag{85}$$

For a dipole transition to be allowed, at least one of these integrals must be non-zero. This occurs if the symmetry properties of the initial state, the final state, and the dipole moment operator along a given direction are compatible according to group theory. In other words, the product of their irreducible representations must contain the totally symmetric irreducible representation of the point group. If the symmetry conditions are not satisfied, the integral will be zero, and the transition will be forbidden by symmetry rules.

In the C_{2h} point group, the dipole moment operator transforms as x, y, or z, which correspond to the B_u and A_u irreducible representations, respectively. Suppose we are analyzing a transition between two states with the following symmetries: the initial state Ψ_i has B_u symmetry, and the final state Ψ_f has A_g symmetry. The dipole moment operator along the x-axis transforms as B_u. Thus, the direct product of the irreducible representations would be

$$B_u \otimes B_u \otimes A_g = A_g, \tag{86}$$

which can be understood through the multiplication of the corresponding rows in Tab. 4. Since the product contains the totally symmetric irreducible representation A_g, this transition is allowed along the x-axis. The symmetry of the initial state, the final state, and the dipole moment operator are compatible, so the transition dipole moment integral will yield a non-zero value, making this transition allowed by symmetry along the x-axis.

3 Results

3.1 Prescreening of Potentially Interesting Molecules

The goal of this section is to develop a computationally efficient prescreening method, which is able to predict excited states characterized by a non-trivial transition density matrix. It is based on properties that are readily available from ground state DFT calculations and involves (i) the symmetry of KS orbitals, (ii) optical transition matrix elements and (iii) energy differences between unoccupied and occupied KS orbitals, respectively.

First, we limit ourselves to molecules in gas phase with less than 40 atoms for computational reasons. Second, as the computationally expensive t-SURFF simulation is restricted to the ALDA functional, we further consider only molecules, if the LDA calculations result in the same ordering of orbitals as calculations employing other functionals. To check this, these results are compared to transition dipole moments and energy differences from B3LYP calculations employing the NWChem code, readily available in the Molecular Orbital Database [34, 35]. Next, due to the Heisenberg uncertainty principle and to exclude degeneracies, large enough energy differences between the states featured in the respective excitation are desirable. Additionally, as the goal of the prescreening is finding candidates for the calculation of momentum maps for the molecules' excited states, we only proceed with excitation profiles if the momentum map features of the contributing unoccupied states are distinguishable enough from each other. Finally, in view of experimental feasibility, we focus on the respective first excitation along the long molecular axis as resulting from the absorption spectra exhibiting a non-trivial excited state transition density matrix.

A table listing all prescreened molecules can be found in appendix A. Out of these molecules tetracene (4A), fluorene, chrysene (4phenacene) and picene (5phenacene) essentially fulfill the stated criteria and are further considered. In addition, sexithiophene (6T) and NTCDA serve as examples for which the chosen level of theory is not enough but are nevertheless included due to their relevance for possible experiments. All molecules are planar $\pi-$conjugated molecules, which are oriented in the $(xy)-$plane with their long molecular axis pointing along the $x-$direction as depicted, e.g. in Fig. 1 for 4A. The displayed character tables are adapted accordingly.

Tetracene

Tetracene ($C_{14}H_4O_6$), a polycyclic aromatic hydrocarbons (PAH), belongs to the class of acenes, consisting of linearly fused benzene rings [36]. It exhibits interesting excited state dynamics in thin film form such as superradiance, exciton fission and triplet recombination [37]. Moreover, tetracene single crystals find application as organic field-effect transistors [38, 39]. POT for tetracene on Ag(110) has revealed two highest occupied molecular orbital emissions, which correspond to different molecular species, indicating the coexistence of charged and uncharged states within the film [40].

Tetracene exhibits D_{2h} symmetry (Tab. 2), as it has a center of inversion, three perpendicular C_2 axis and three mirror planes [41, 31]. In this case transitions
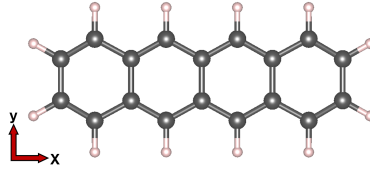
Fig. 1: Geometry of the tetracene molecule.

through x-polarized light, i.e. along the long molecular axis, are allowed if the product of irreducible representations gives B_{2u}. This is the situation for $A_g \leftrightarrow B_{2u}$, $B_{1g} \leftrightarrow B_{3u}$, $B_{2g} \leftrightarrow A_u$ and $B_{3g} \leftrightarrow B_{1u}$ transitions. These symmetry selection rules are in accordance with the transition dipole moments in Fig. 2. Here, the transition dipole strength is represented as circle areas positioned on a grid with the valence band states ordered from top to bottom and the conduction band states from left to right. Note that here and in the following, the highest occupied molecular orbital (HOMO) is abbreviated as H, while the lowest unoccupied molecular orbital (LUMO) is abbreviated as L. The labels $H - 1$, $H - 2$, $H - 3$, and so forth refer to the lower lying valence states, whereas $L + 1$, $L + 2$, $L + 3$, and so on denote the next higher conduction states. Therefore, the H→L transition is situated in the top left corner. Additionally, the orbital energy differences are colour-coded where dark blue indicates small energy differences, while dark red large ones. Panel (a) shows the result based on database orbitals calculated with the B3LYP functional, whereas in panel (b) states from an OCTOPUS LDA calculation are used. Both approaches agree and lead to the same excitation profile, mainly consisting of a H → L+2 ($B_{3g} \rightarrow B_{1u}$) and a H-2 → L ($B_{3g} \rightarrow B_{1u}$) transition. Both of these transitions have similar dipole strengths of 3.2-3.4 eV·Å for both functionals, but, as expected, larger energy differences of 4.3-4.5 eV for B3LYP compared to 3.0-3.2 eV for LDA. Therefore, tetracene is a promising example for which two different valence band state momentum maps appear at kinetic energies corresponding to ionization potentials of different conduction band states, which represents an actual entangled state [42].

Tab. 2: Character table for the D_{2h} point group from [33] and 4A orbitals belonging to a certain irr. rep.

| D_{2h}	E	C_{2z}	C_{2y}	C_{2x}	i	σ_{xy}	σ_{xz}	σ_{yz}	Pol. Dir.	Orbitals
A_g	1	1	1	1	1	1	1	1		
B_{1g}	1	1	-1	-1	1	1	-1	-1		
B_{2g}	1	-1	-1	1	1	-1	-1	1		
B_{3g}	1	-1	1	-1	1	-1	1	-1		H, H-2
A_u	1	1	1	1	-1	-1	-1	-1		
B_{1u}	1	1	-1	-1	-1	-1	1	1	z	L, L+2
B_{2u}	1	-1	-1	1	-1	1	1	-1	x	
B_{3u}	1	-1	1	-1	-1	1	-1	1	y	
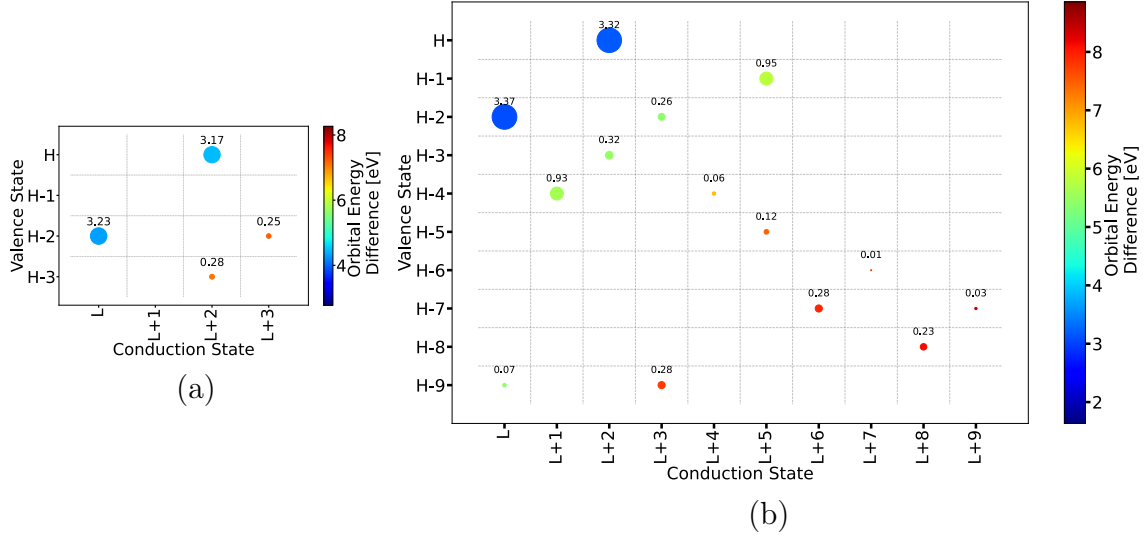
Fig. 2: Transition dipole moments in x direction in eV·Å as circle areas calculated via Eq. 82 with colour-coded energy differences and orbitals from (a) readily available database B3LYP [34] and (b) OCTOPUS LDA ground state calculations for 4A.

Fluorene

Fluorene ($C_{13}H_{10}$) is another member of the polycyclic aromatic hydrocarbon family and consists of a five-membered cyclopentane ring fused with two benzene rings [43]. Also, the electronic properties of fluorene and its heteroanalogues are characterized by π-conjugation [44]. They act as donors in photoactive materials containing donor-acceptor-donor structures [45], are the base for click-polymers for dye-sensitized solar cells [46] and organic field-effect transistors in form of liquid-crystalline polymers [47]. Moreover, two photon absorption [48] by the means of TD-DFT and valence and Rydberg electronic transitions [44] have been studied for fluorene.
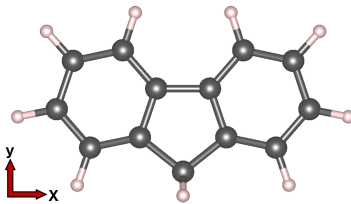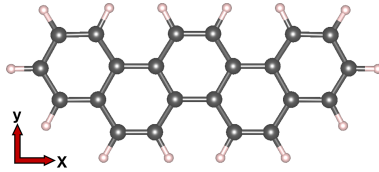

Fig. 3: Geometry of the fluorene molecule.

It has a C_{2v} point group symmetry (Tab. 3), because of a two-fold rotational axis and two vertical mirror planes [31, 32]. This means that transitions through x polarized light are allowed if the product of the irr. reps. gives B_g, which is the case for $A_g \leftrightarrow B_g$ and $A_u \leftrightarrow B_u$. This aligns with the transition dipole moments in Fig. 4 below for the B3LYP (panel (a)) as well as the LDA states (panel (b)), showing non-vanishing values for H $\rightarrow$ L, H $\rightarrow$ L+1, H-2 $\rightarrow$ L+1 (all $A_u \rightarrow B_u$) as well as H-1 $\rightarrow$ L+2 ($B_u \rightarrow A_u$) transitions. As the energy difference between the H and L and the and L+1 energies are comparable, it can be assumed that these will contribute to the lowest-lying excitation, with the H-1 $\rightarrow$ L+2 and H-2 $\rightarrow$ L+1 transitions making

28

up the next higher excited state. Therefore, the photoemission angular distribution (PAD) for the first exciton in fluorene is expected to be proportional to the Fourier transform of a coherent sum of the L and L+1.

Tab. 3: Character table for the C_{2v} point group from [33] and fluorene orbitals belonging to a certain irr. rep.

| C_{2v}	E	$C_2(y)$	$\sigma_{v(xy)}$	$\sigma_{v(yz)}$	Pol. Dir.	Orbitals
A_g	1	1	1	1	y	
A_u	1	1	-1	-1		H, H-2, L+2
B_g	1	-1	1	-1	x	
B_u	1	-1	-1	1	z	H-1, L, L+1

(a)

(b)
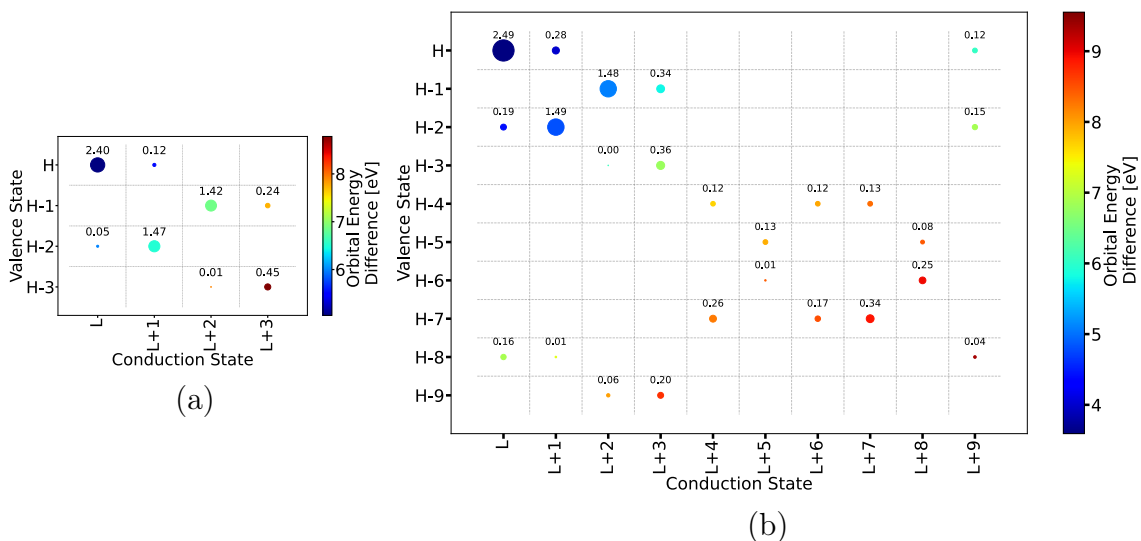
Fig. 4: Transition dipole moments in x direction in eV·Å as circle areas calculated via Eq. 82 with colour-coded energy differences and orbitals from (a) readily available database B3LYP [34] and (b) OCTOPUS LDA ground state calculations for fluorene.

Chrysene

Chrysene ($C_{13}H_{10}$), a tetracene isomer, thus also composed of four benzene rings, but arranged in a zigzag manner and part of the phenacene class [49]. It can be used as a blue fluorescent emitter in organic light-emitting diodes (OLEDs), with some derivatives showing deep blue emissions and high quantum efficiency [50, 51]. However, it also poses environmental and health risks as it may be phototoxic and photogenotoxic under UVB radiation [52] and contains carcinogenic properties and environmental persistence due to low solubility [53]. First principle calculations have revealed that it undergoes a red-shift under pressure [54], and the time-dependent density functional based tight binding (TD-DFTB) method has been applied to investigate electronic relaxations, revealing that the brightest excited state in chrysene decays faster compared to tetracene [55].

With a two-fold rotational axis (C_2), a mirror plane perpendicular to the C_2-axis, that lies in the plane of the molecule and a center of inversion, it has C_{2h} point group symmetry (Tab. 4) [31, 56]. The corresponding character table is
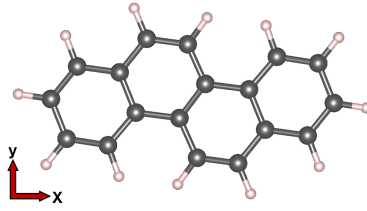
Fig. 5: Geometry of the chrysene molecule.

Tab. 4: Character table for the C_{2h} point group from [33] and chrysene orbitals belonging to a certain irr. rep.

C_{2h}	E	$C_2(z)$	i	σ_h	Pol. Dir.	Orbitals
A_g	1	1	1	1		
A_u	1	1	-1	-1	z	H, H-1
B_g	1	-1	1	-1		L, L+1
B_u	1	-1	-1	1	x, y	

The transitions in Fig. 6 exhibiting the strongest dipole moment with the lowest energy differences of 4.2-5.1 eV for B3LYP and 2.9-3.8 eV for LDA are H → L, H → L+1, H-1 → L and H-1 → L. These are allowed per x polarization according to C_{2h} symmetry because they are of $A_u \rightarrow B_g$ kind, as the direct product of these irr. rep. and gives B_u. Here, it needs to be noted that H → L+1 shows a stronger dipole moment than H → L, while H-1 → L shows a stronger one than H-1 → L+1. This indicates that for the first excitation two PADs appear at different kinetic energies, that both show features of the L and L+1 PAD, however, differing regarding the main contribution. Additionally, by comparing Fig. 6 panel (a) with panel (b) it is visible that the ordering of the L+3 and L+4 is interchanged for the two applied functionals. However, transitions involving these states are expected to not considerably contribute to the lowest lying excitation due to weak transition dipole moments and low energy differences compared to the aforementioned H and H-1 transitions.
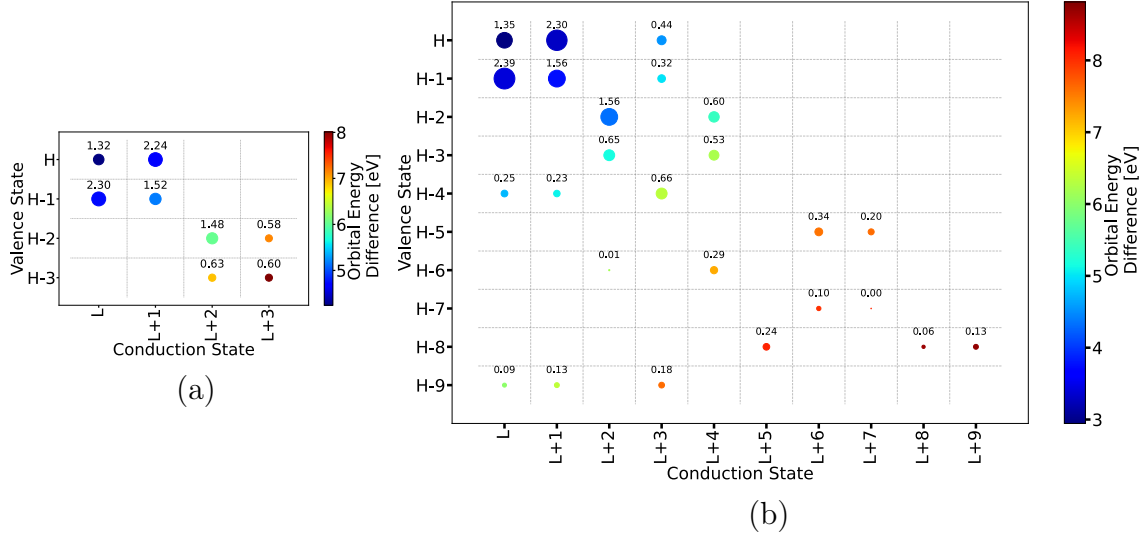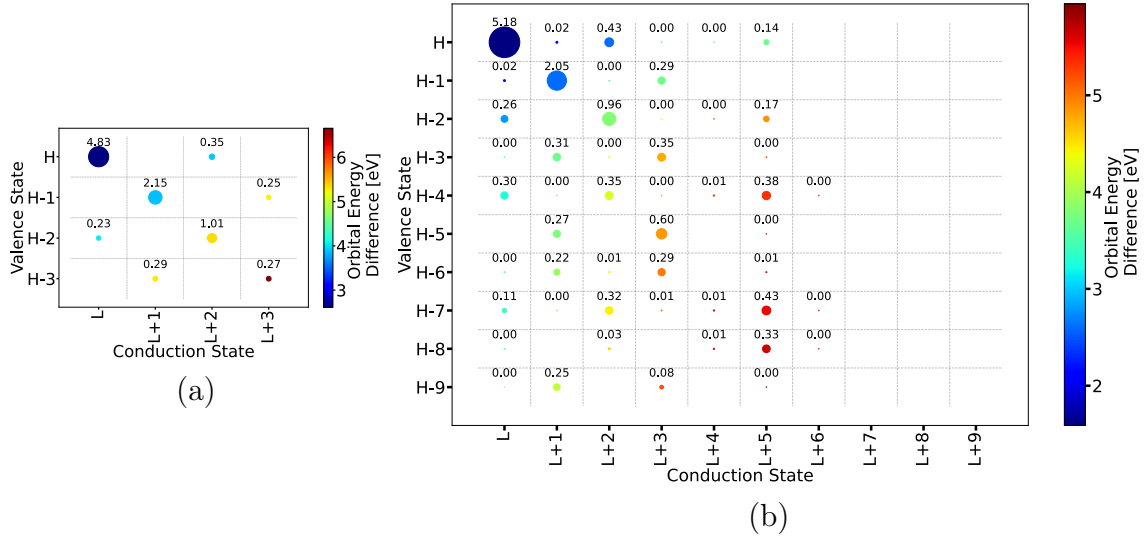
Fig. 6: Transition dipole moments in x direction in eV·Å as circle areas calculated via Eq. 82 with colour-coded energy differences and orbitals from (a) readily available database B3LYP [34] and (b) OCTOPUS LDA ground state calculations for chrysene.

Picene

The five-ring phenacene member, picene, has the chemical formula $C_{22}H_{14}$ and is an isomer of pentacene [49]. It is a versatile material in electronic and optoelectronic applications such as field-effect transistors (FETs) using alkyl-substituted picene demonstrating high field-effect mobility [57]. Additionally, picene nanocrystalline thin films doped with pentacene exhibit efficient energy transfer from picene to pentacene, resulting in intense photoluminescence from pentacene, which could be exploited in applications such as microwave amplification by stimulated emission [58]. It was used as an example for the simulation of angle-resolved photoemission spectroscopy (ARPES) intensity maps by approximating the final state as a plane wave [2] and POT was applied to a picene multilayer on an Ag(110) multilayer deconvoluting the free frontier orbitals of picene [59, 60].

Fig. 7: Geometry of the picene molecule.

It has C_{2v} point group symmetry (Tab. 5) due to a two-fold rotational axis and two vertical mirror planes [31, 56]. The transitions discussed in the following are all of $A_u \leftrightarrow B_u$ kind and thereby allowed via x polarization. Panel (a) as well as (b) of Fig. 8 are dominated by the H → L transition as it exhibits the strongest transition dipole together with the lowest difference in orbital level energies. Additionally, the next strongest allowed transitions are H-1 → L+1, H-1 → L+2, H-2 → L+1 and H-2 → L+2 with energy differences ranging from 4.6 eV to 5.7 eV for B3LYP

Tab. 5: Character table for the C_{2v} point group from [33] and picene orbitals belonging to a certain irr. rep.

C_{2v}	E	$C_2(y)$	$\sigma_{v(xy)}$	$\sigma_{v(yz)}$	Pol. Dir.	Orbitals
A_g	1	1	1	1	y	
A_u	1	1	-1	-1		H-1, H-2, L
B_g	1	-1	1	-1	x	
B_u	1	-1	-1	1	z	H, L+1, L+2

and from 3.3 eV to 4.1 eV for LDA. This suggests that the lowest lying picene excitation mainly consists of the H $\rightarrow$ L transition and that a higher lying one has contributions similar to the chrysene case. Namely, two momentum distributions composed of features associated with the L+1 and L+2, but varying in intensity and appearing at two different kinetic energies.
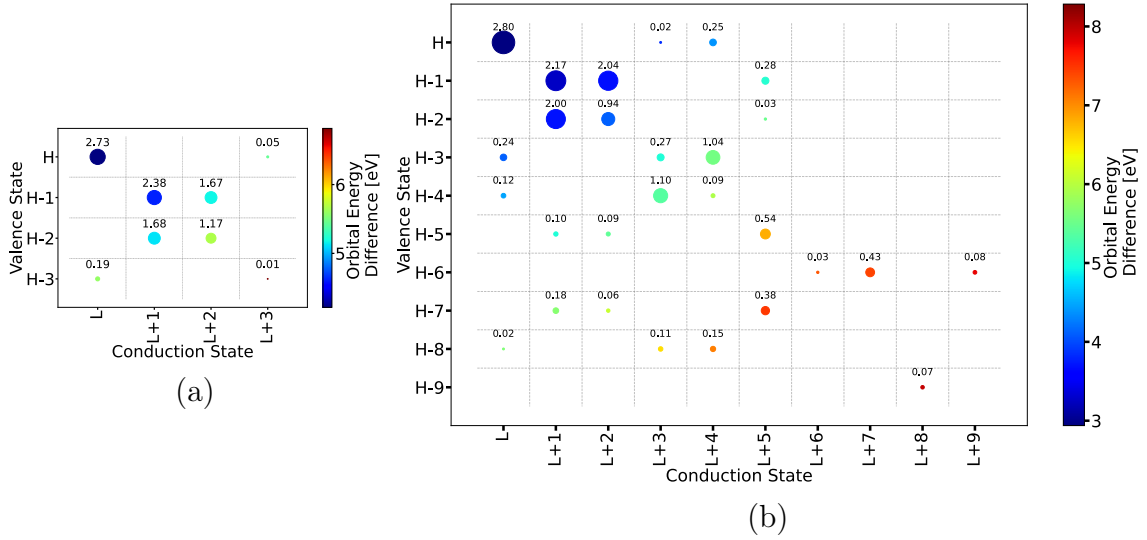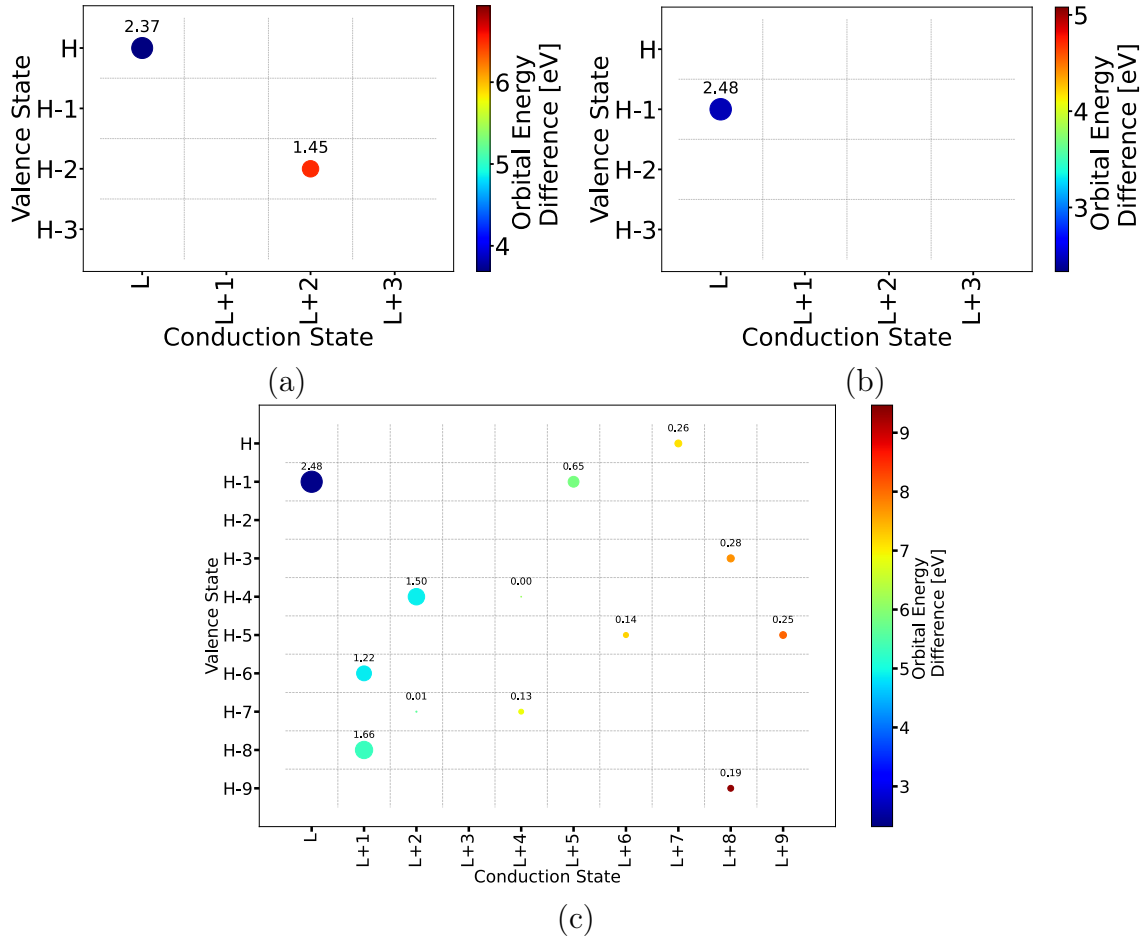

Fig. 8: Transition dipole moments in x direction in eV·Å as circle areas calculated via Eq. 82 with colour-coded energy differences and orbitals from (a) readily available database B3LYP [34] and (b) OCTOPUS LDA ground state calculations for picene.

Sexithiophene

Sexithiophene is an organic semiconductor with optical and electronic properties controlled by its π-conjugation [61], whose UV-visual absorption spectrum is characterized by a few distinct peaks [62]. 6T thin films in particular find application in organic photovoltaic cells [63]. As it can be seen in Fig. 9, it consists of 6 planar thiophene, C_4H_4S, rings and its molecular formula is $C_{24}H_{14}S_6$.
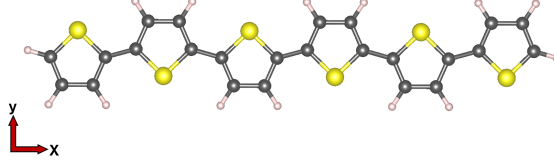
Fig. 9: Geometry of the sexithiophene molecule.

Sexithiophene belongs to the C_{2h} symmetry group (Tab. 6) as it has a mirror plane perpendicular to the two-fold rotational axis C_2 [62, 64]. For dipole-allowed optical transitions, which are polarized in the $(xy)-$plane, the product of initial and final states must belong to the irreducible representation B_u. This implies that the permitted transitions involve A_g and A_u or B_g and B_u states, respectively, as initial and final states. These selection rules are consistent with the transition dipole moments for the long molecular axis illustrated in Fig. 10, where panel (a) is based on database orbitals calculated with the B3LYP functional and panel (b) on an OCTOPUS LDA calculation. Here it can be seen that the H $\to$ L ($B_g \to A_u$) and H-1 $\to$ L+1 ($A_u \to B_g$) transitions show the strongest transition dipole moments with additional, but weaker, contributions from H-2 $\to$ L, H-3 $\to$ L+3 (both $B_g \to A_u$) and H $\to$ L+2, H-2 $\to$ L+2 (both $B_g \to A_u$) for both functionals. Therefore, similar to tetracene, the excitation profile for 6T promises to represent an entangled state.

Tab. 6: Character table for the C_{2h} point group from [33] and 6T orbitals belonging to a certain irr. rep.

C_{2h}	E	$C_2(z)$	i	σ_h	Pol. Dir.	Orbitals
A_g	1	1	1	1		
A_u	1	1	-1	-1	z	H-1, L, L+2, L+3
B_g	1	-1	1	-1		H, H-2, H-3, L+1
B_u	1	-1	-1	1	x, y	

Fig. 10: Transition dipole moments in x direction in eV·Å as circle areas calculated via Eq. 82 with colour-coded energy differences and orbitals from (a) readily available database B3LYP [34] and (b) OCTOPUS LDA ground state calculations for 6T.

NTCDA

1,4,5,8-naphthalenetetracarboxylic dianhydride (NTCDA) is an organic semiconductor exhibiting a wide band gap, which makes it transparent in visible range and useful as an exciton blocking layer in organic photovoltaic devices [65]. In the context of POT NTCDA has been used as an example to show that understanding photoemission intensities requires going beyond the molecular orbital picture, as imaging experiments show Dyson orbitals [3]. It contains a naphthalene ring system, which consists of fused C6 aromatic rings [66]. Its molecular formula is $C_{14}H_4O_6$ and the geometry can be seen in Fig. 11 below.
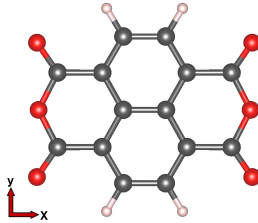
Fig. 11: Geometry of the NTCDA molecule.

As it contains three mutually perpendicular symmetry planes as well as three C_2 rotational axes, whose crossing point is a center of symmetry, it belongs to the D_{2h} point group (Tab. 7) [31, 67]. Transitions along the long molecular axis (x direction) for this point group are electronically allowed if the direct product of the representations of the electronic states has B_{2u} symmetry [33]. This is in accordance with the transition dipole moments shown in Fig. 12. Here it needs to be noted that for panel (a) states calculated with the B3LYP functional are used, whereas panel (b) is based on the PBE and panel (c) on the LDA functional. This explains the different ordering of the outer valence orbitals and in particular the

Tab. 7: Character table for the D_{2h} point group from [33] and NTCDA orbitals belonging to a certain irr. rep.

D_{2h}	E	C_{2z}	C_{2y}	C_{2x}	i	σ_{xy}	σ_{xz}	σ_{yz}	Pol. Dir.	Orbitals (PBE, LDA)	Orbitals (B3LYP)
A_g	1	1	1	1	1	1	1	1			
B_{1g}	1	1	-1	-1	1	1	-1	-1			
B_{2g}	1	-1	-1	1	1	-1	-1	1		L, L+5	L
B_{3g}	1	-1	1	-1	1	-1	1	-1		H-6, H-8, L+2	L+2
A_u	1	1	1	1	-1	-1	-1	-1		H-1	H
B_{1u}	1	1	-1	-1	-1	-1	1	1	z	H-4, L+1	H-2
B_{2u}	1	-1	-1	1	-1	1	1	-1	x		
B_{3u}	1	-1	1	-1	-1	1	-1	1	y		

change in π- or σ-character for the HOMO, as discussed in [3]. This underlines the importance of the choice of functional for ExPOT [Eq. 63], to correctly explain the contributing particle-hole interactions and momentum map features. However, the apparent transitions are consistent with respect to the symmetry rules from Tab. 7 as the H-1 $\rightarrow$ L transition for PBE and LDA and the H $\rightarrow$ L transition for B3LYP are of $A_u \rightarrow B_{2g}$ kind. Moreover, the additional transitions in Fig. 12 are electronically allowed with the H-1 $\rightarrow$ L+5 transition being of $A_u \rightarrow B_{2g}$, H-4 $\rightarrow$ L+2 of $B_{1u} \rightarrow B_{3g}$ and H-6 $\rightarrow$ L+1 and H-8 $\rightarrow$ L+1 of $B_{3g} \rightarrow B_{1u}$ character. As the states involved in these transitions are also energetically close, NTCDA is interesting for further Casida calculations.

Fig. 12: Transition dipole moments in x direction in eV·Å as circle areas calculated via Eq. 82 with colour-coded energy differences and orbitals from (a) B3LYP and (b) PBE ground state calculations from [34] and (c) OCTOPUS LDA ground state calculations for NTCDA.

3.2 Optical Response

In this section, we describe and compare two different ways to obtain optical absorption spectra of the investigated molecules together with convergence test results for these methods. The convergence plots are only shown for 4A, as the results for the other molecules do not deviate significantly. Additional results for the remaining molecules can be found in Appendix B.

On the one hand, we employ RT-TDDFT where, after a preceding ground state calculation, we perturb the system at an initial time $t = 0$ with a δ-pulse with a pulse strength of 0.01 Å^{-1} that equally excites all optically allowed transitions [68]. The system then evolves for 6.5 fs with a time step of 1.5 as. Regarding convergence, we vary the real space grid point spacing from 0.18 Å to 0.32 Å as well as the radius of the spherical simulation box from 5.0 Å to 12.0 Å. For these tests, we define the convergence criterion to be an energy difference of 0.01 eV for the peak energy of the excitation of interest. We continue to use the obtained spacing and excitation energy values in the subsequent t-SURFF simulation, as it is also performed in the RT-TDDFT realm.

On the other hand, we compute the absorption spectrum by solving Casida's equation [Eq. 50] from LR-TDDFT [25]. To this end, we start from a ground state calculation using the same geometry parameters from the RT-TDDFT calculation and but we perform an unoccupied states calculation with 300 additional states. Note that this value is at least 5 times the number of occupied states of the considered molecules. Based on these states, the optical spectrum together with its decomposition into transitions from electron-hole pairs is obtained. We seek convergence of the spectrum with respect to the Kohn-Sham energy window, i.e. the maximally allowed eigenvalue difference for specifying which occupied-unoccupied transitions will be taken into account, from 18 eV to 38 eV with a convergence threshold defined by an energy difference of 0.01 eV for the targeted peak. The thereby calculated transition density matrix for the m-th excitation $X_{vc}^{(m)}$ quantifies the respective exciton characteristics and renders the calculation of momentum maps via the exPOT approach [Eq. 63] possible. Moreover, note that the calculations include de-excitations beyond the Tamm-Dancoff approximation.

3.2.1 Tetracene

Fig. 13 shows the absorption spectrum of 4A for light polarized along the x-direction upon excitation with a δ-pulse for different grid spacing values ranging from 0.18 Å to 0.32 Å. In panel (a), it can be seen that the spacing values of 0.24 Å and below, the spectra can be considered to be converged even for energetically higher excitations above 10 eV. Panel (b) shows a zoomed-in region around the first prominent absorption peak revealing revealing convergence of the peak with respect to the spacing within 0.01 eV at 4.34 eV. In order to ensure sufficient accuracy in the t-SURFF simulation while keeping the computational cost reasonable, we rely on a grid spacing value of 0.22 Å and select a pump pulse energy of 4.34 eV.

In order to test the robustness of the Casida LR-TDDFT spectrum with respect to the Kohn-Sham energy window, the spectra are calculated for energy windows ranging from 18 eV to 38 eV, which is illustrated in Fig. 15. From panel (a) it is
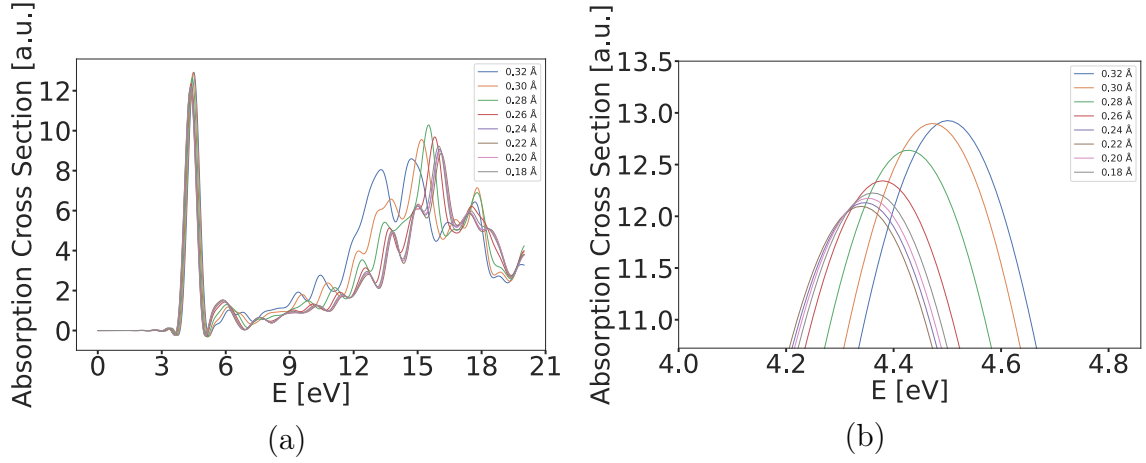
Fig. 13: Convergence of the RT-TDDFT optical spectrum upon excitation with a δ-kick with respect to the grid spacing for 4A for the (a) full energy range and (b) zoomed in on the relevant excitation.
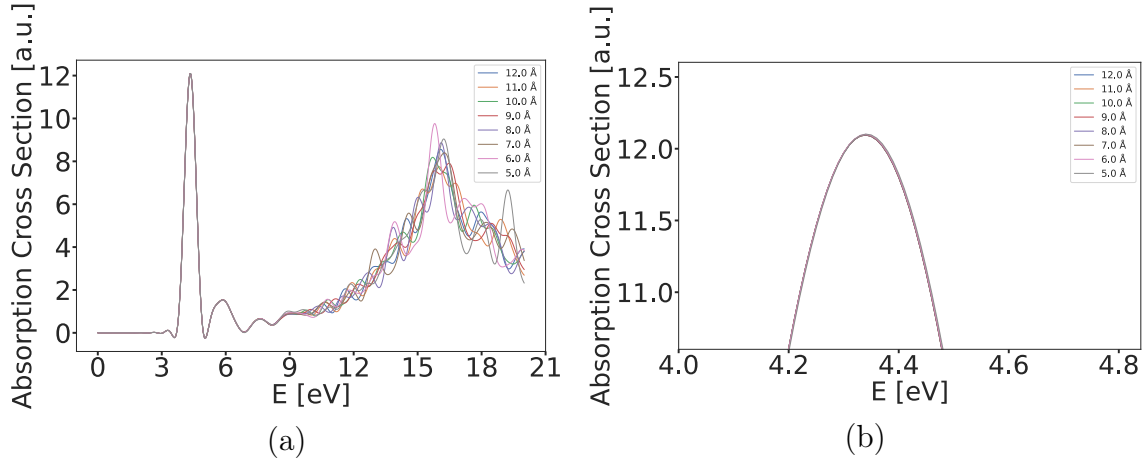
Fig. 14: Convergence of the RT-TDDFT optical spectrum upon excitation with a δ-kick with respect to the simulation box radius for 4A for the (a) full energy range and (b) zoomed in on the relevant excitation.

apparent that all curves are matching closely even beyond the relevant energy range up to 10 eV, with only the 18 eV showing some deviations for transition energies larger than 15 eV on. This disagreement increases from 17 eV onwards with also the 22 eV curve starting to show significant differences. Taking a closer look at the first peak in panel (b), it can be seen that the 30 eV, 34 eV and 38 eV curves align very well at a peak position of 4.34 eV, with the other curves straying notably. Therefore, we proceed with the Casida contributions resulting from the 30 eV energy window calculation for the calculation of momentum maps via the exPOT approach.
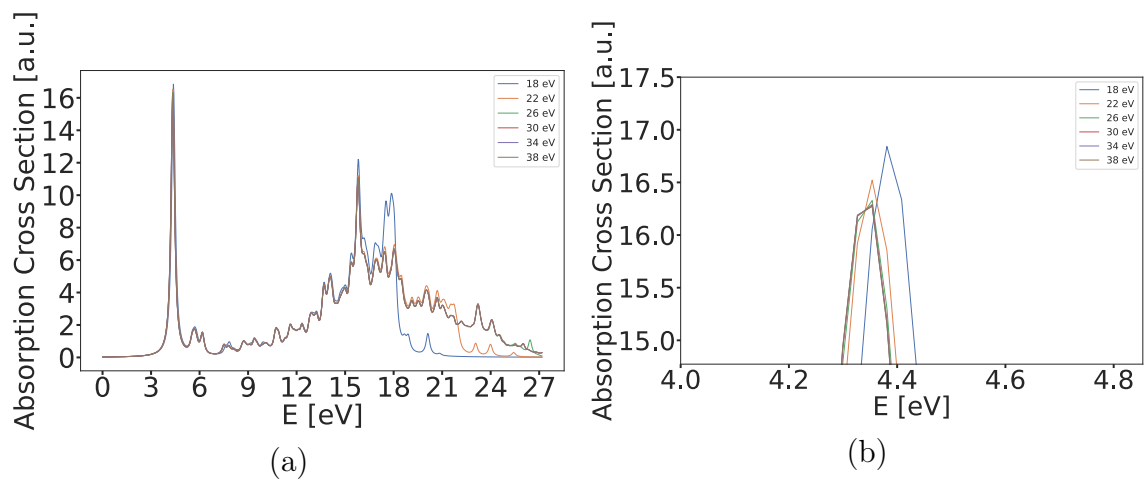
Fig. 15: Convergence of the Casida LR-TDDFT optical spectrum with respect to the Kohn-Sham energy window for 4A for the (a) full energy range and (b) zoomed in on the relevant excitation.

3.3 Momentum Maps

The goal of this section is to simulate photoemission angular distribution maps, so-called momentum maps, for optically excited states. These theoretical predictions are relevant for time-and angle-resolved photoemission experiments, where a pump laser pulse creates an optical excitation and probe pulse kicks out an electron from the molecule.

From the optical absorption spectra discussed in the previous section, the pump pulse energy is obtained using RT-TDDFT, while the associated transition density matrix is derived from LR-TDDFT. This information enables to compare two different theoretical approaches to calculate momentum maps. On the one hand, the predictions of exPOT [7] and on the other hand, the more computationally intensive, but accurate TDDFT simulations implemented in the real-space code OCTOPUS [29] generating PAD maps using the t-SURFF method.

To enhance the comparability between the exPOT and t-SURFF approaches, several steps are taken as outlined in [7]. First, the probe field is chosen in the z-direction, perpendicular to the molecular plane, to minimize potential deficiencies of the plane wave approximation [69]. Second, we use sufficiently long pump pulses to target specific excitons, minimizing energy broadening from ultrashort pulses [70]. Probe pulses are also kept long to achieve good kinetic energy resolution. Lastly, we use the adiabatic local density approximation (ALDA) for the t-SURFF method, as more advanced functionals would be too computationally demanding. However, this restriction does not apply to the exPOT formalism, which can utilize any method that provides a transition density matrix in terms of single-particle orbitals.

3.3.1 Tetracene

We first investigate tetracene, whose optical absorption spectrum is shown in Fig. 16 panel (a). Here we compare the absorption spectra obtained from LR-TDDFT and RT-TDDFT as discussed in Sec. 3.2. We find excellent agreement for the position of the first peak at 4.34 eV for both methods, where the RT-TDDFT position is marked with a red dashed line and the LR-TDDFT one with an asterisk. In panel (b) the absolute squares of the Casida contributions for the considered excitation are shown. These contributions compose the transition density matrix, characterizing the exciton, as obtained by solving Eq. 50. The matrix elements are arranged as colour-coded rectangles on a grid, with the valence states arranged vertically from top to bottom and the conduction states horizontally from left to right. All of the displayed transitions are allowed per the D_{2h} symmetry rules in Tab. 2. It is evident that the first exciton for tetracene is mainly made up of a H $\rightarrow$ L+2 transition, a H-2 $\rightarrow$ L transition and a small contribution from H-2 $\rightarrow$ L+3. Therefore, as can be seen in Eq. 63, it is expected that the momentum maps appearing at the kinetic energies corresponding to the ionization potentials of the H and H-2 resemble the Fourier transforms of the L+2 and L, respectively. Thus, this exciton represents an entangled state.

Before computing the momentum maps from exPOT, we also present the computational details of the t-SURFF approach. With the provided pump pulse energy, the pump-probe laser system is configured as illustrated in Fig. 17. In this laser
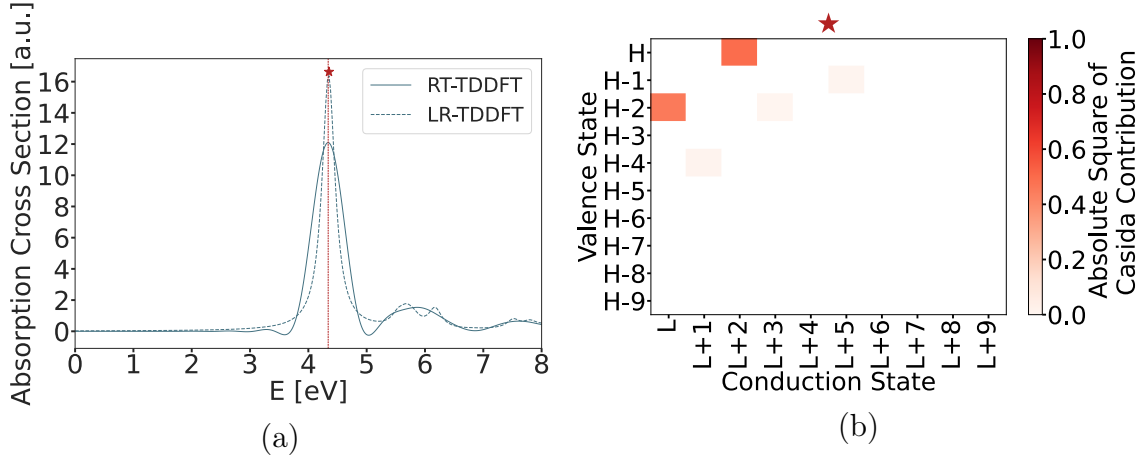
Fig. 16: (a) Converged absorption spectra for 4A calculated with OCTOPUS in RT-TDDFT (full line) and from Casida's formalism within LR-TDDFT (dashed line). The excitation energy used in the pump-probe simulation is marked with a vertical red dashed line, while the Casida excitation energy is marked with a red asterisk. (b) Absolute square of the occupied-unoccupied Casida transition contributions for the excited state marked with a red asterisk.

setup both the pump and probe pulses are Both pulses are shaped with a $\sin^2$-type envelope to ensure smooth on/off switching and are applied simultaneously and with the same pulse duration, e.g. for 25 fs. All pump-probe simulations in this work are based on this configuration, with variations in pulse length applied equally to both pulses for all molecules. Additionally, the pump field energy is adjusted to match the specific excitation studied, while the probe pulse energy remains constant with an energy of 35 eV. Both field amplitudes are set to simulate laser intensities of 10^8 W/cm^2. Throughout the simulations, the pump pulse is always polarized in the x direction, while we use a z-polarized probe pulse. To prevent spurious reflections at the simulation boundaries, a complex absorbing potential (CAP) of the form $i\xi \sin^2 \left(\Theta \left(r - R_0 \right) \frac{\pi}{2R} \right)$ with $\xi = -0.2$ a.u. is introduced, starting at $R_0 = 15$ Å. The flux of electron density is monitored over time through a spherical surface at R_0, allowing us to compute angle- and energy-resolved photoemission intensities numerically.

Fig. 18 shows the angle-integrated photoelectron intensity as a function of the kinetic energy of the photoemitted electrons for tetracene as obtained from the pump-probe simulation with the t-SURFF method. Note that we are using a logarithmic scale for the intensity and that we are comparing the results for three different pulse times, namely 10 fs, 15 fs and 25 fs. The solid vertical lines are positioned at energy levels $\omega - \epsilon_j$ and mark the emissions from the occupied states, i.e. H-2, H-1 and H from left to right. Note that the H-1 and H-2 form a double peak. According to the predictions of the exPOT formalism, one expects also peaks at $\omega - \epsilon_j + \omega_{\text{pump}}$, indicated by the dashed lines. Indeed, the t-SURFF simulation results in peaks at these energies in accordance with the energy conservation in Eq. 63 as well as the transition density matrix in Fig. 16 panel (b).

Regarding the different pulse lengths, it is evident that as the pulse length in-
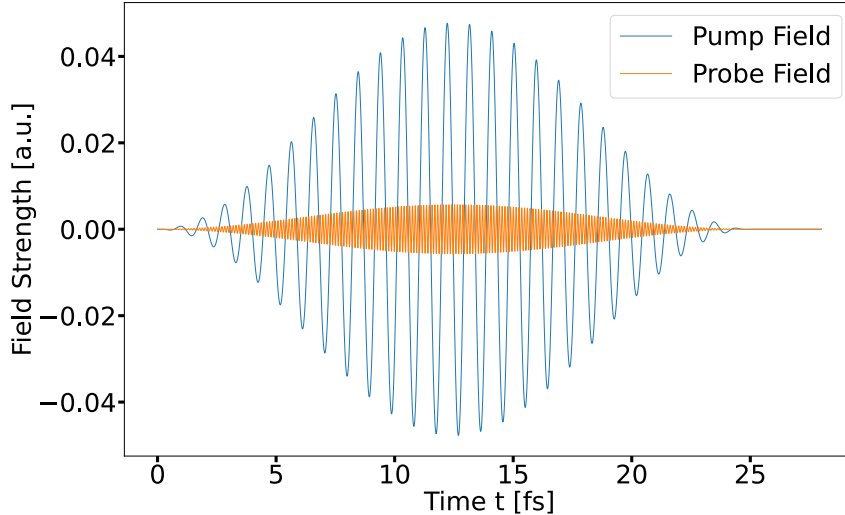
Fig. 17: Example pump-probe laser setup used for photoemission simulations in this work. Pulse duration and intensity are 25 fs and 10^8 W cm^{-2} respectively for both fields. The pump field frequency is tailored according to the excitation under consideration, while the probe pulse frequency remains unchanged attributed to a fixed energy of 35 eV. In this case for tetracene, the pump pulse energy is set to 4.34 eV.

creases, the peaks in the spectrum become progressively narrower. This aligns with the Heisenberg uncertainty principle, from which we expect an inverse relationship between time and energy uncertainty, leading to improved energy resolution with longer pulse durations. Explicitly, from $\Delta E \geq \frac{\hbar}{2\Delta t}$, we obtain energy resolutions of 0.33 eV, 0.23 eV and 0.13 eV for pulse lengths of 10 fs, 15 fs and 25 fs, respectively. In the following, we discuss the impact of the pulse length on the PAD features obtained from the t-SURFF method and compare these maps to the Fourier transforms of the involved occupied and unoccupied states.

Fig. 19 shows the PAD of the occupied state corresponding to ϵ_1, the H or $v = 1$, for the three different pulse lengths (panel (a)-(c)) as well as the Fourier transform of the highest occupied orbital (panel (d)). Note, that the colorbar on the right-hand side applies to all subsequent momentum maps, as the intensities have been normalized. Therefore, the colorbar will be omitted in all further maps for the sake of a more compact presentation. Due to the fact that the H is energetically well-seperated from the lower lying orbitlas, only features associated with the H are visible for all pulse lengths. In the top row (panel (a) - (c)) of Fig. 20 the map appearing at $E_{\text{kin}} = \omega - \epsilon_3$ is depicted. In this case, as the ionization potentials of the H-1, ϵ_2, and the H-2, ϵ_3, are seperated only by 0.2 eV and we therefore expect to observe signatures at both orbitals. In particular, features from the H-1 (Fig. 20 panel (d)) arise at $k_x = 0$ Å, $k_y = \pm 1$ Å and $k_x = \pm 0.8$ Å, $k_y = \pm 1$ Å. These features decrease in intensity with longer pulse lengths due to the enhanced energy resolution, while the features corresponding to the H-2 (Fig. 20 panel (e)) remain unchanged.

Next, we compare the excited state momentum maps from the t-SURFF simulation to the Fourier transforms of the mainly contributing unoccupied states
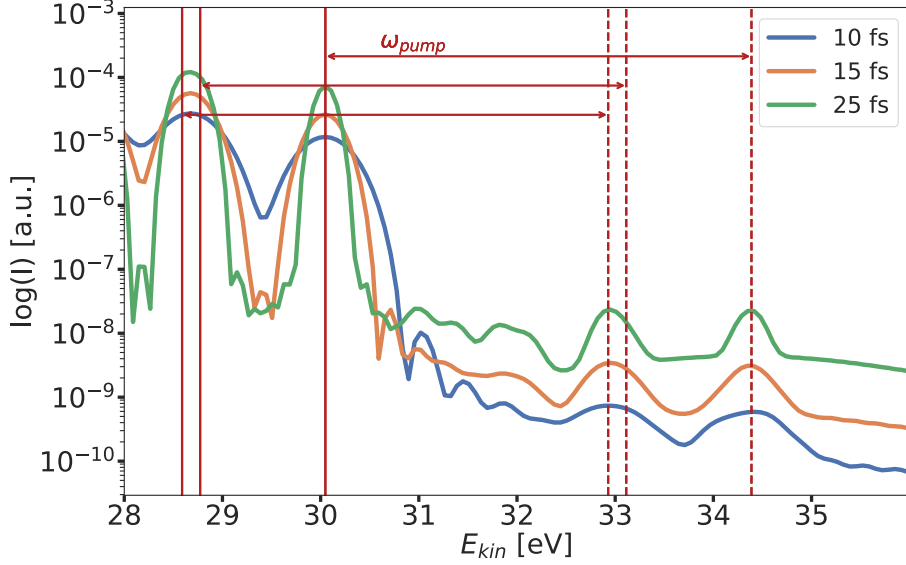
Fig. 18: Total angle-integrated photoelectron intensity from t-SURFF for different pulse durations for 4A. The solid vertical lines mark the energy levels corresponding to the occupied states, while the dashed vertical lines denote the energy levels of the excited states. The horizontal arrows indicate the pump pulse energy $\omega_{\text{pump}} = 4.34$ eV used in the simulation.

in the transition density matrix Fig. 16 panel (b). The PADs corresponding to $E_{\text{kin}} = \omega - \epsilon_1 + \omega_{\text{pump}}$ are depicted in Fig. 21 panel (a)-(c) for the three different pulse lengths, while panel (d) shows the Fourier transform of the L+2. The main features of these maps are consistent for both methods, though some asymmetries are observed in the t-SURFF maps. Notably, as the pulse length increases, the asymmetric patterns evolve, leading to an enhanced intensity in the oval structures at $k_x = 1.5$ Å. This improves the agreement with the L+2 map. Subsequently, the momentum maps evaluated at $E_{\text{kin}} = \omega - \epsilon_3 + \omega_{\text{pump}}$ for the different pulse lengths are presented in Fig. 22 panels (a) to (c). The most intense features in these maps show strong agreement with the Fourier transform of the L in panel (d), while also exhibiting contributions from the L+3 (panel (e)). This observation is consistent with the Casida contributions in Fig. 16 panel (b), which indicates a dominant contribution from the L alongside an additional contribution from L+3. Moreover, it is noticeable that as the energy resolution increases, the intensity of the L+3 features diminishes, whereas the L features stay constant. In the following comparison of methods for obtaining PADs and for the other observed molecules, only the results using a 25 fs pulse length are presented.

Proceeding further, we now compare the t-SURFF result for tetracene to the exPOT approach. The momentum maps in panel (a) of Fig. 23 and Fig. 24 obtained using the t-SURFF method show strong agreement with those derived from the EXPOT and NTO approaches in panel (b) and (c) of both figures. All methods capture the primary features observed in the Fourier transforms of the L+2 in the case of $v = 1$ and L for $v = 3$, respectively. This indicates the presence of an entangled state, consisting of the H $\rightarrow$ L+2 transition contribution of 49%, while the
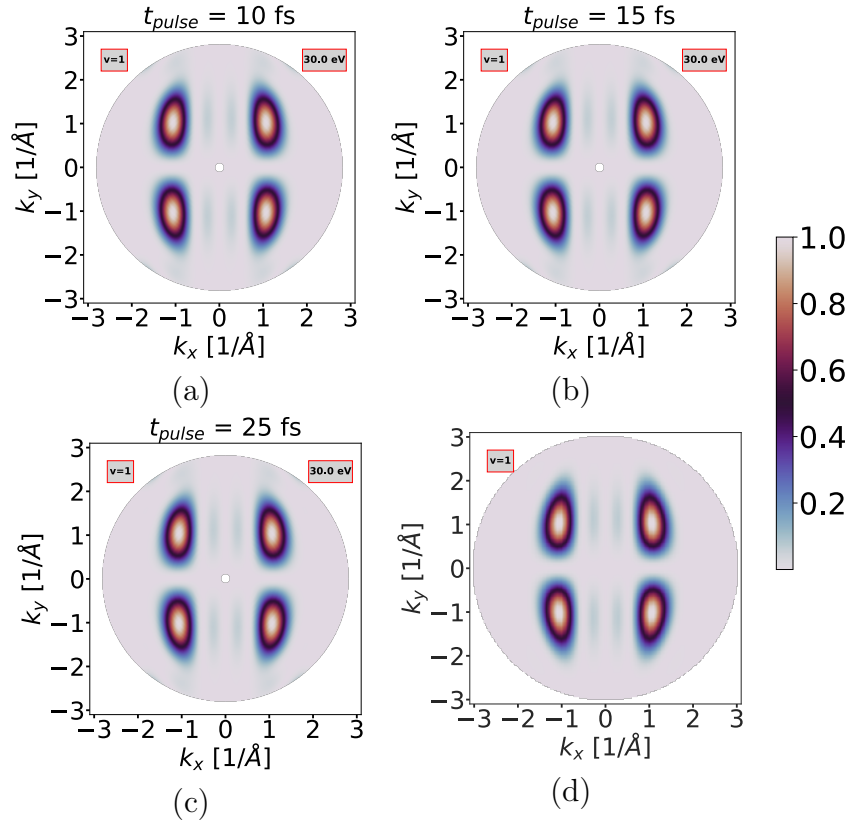
Fig. 19: Comparison of the occupied state momentum maps for tetracene: t-SURFF PAD appearing at $E_{\text{kin}} = \omega - \epsilon_1 = 30.0$ eV for different pulse lengths of (a) 10 fs, (b) 15 fs and (c) 25 fs and (d) Fourier transform of the H.
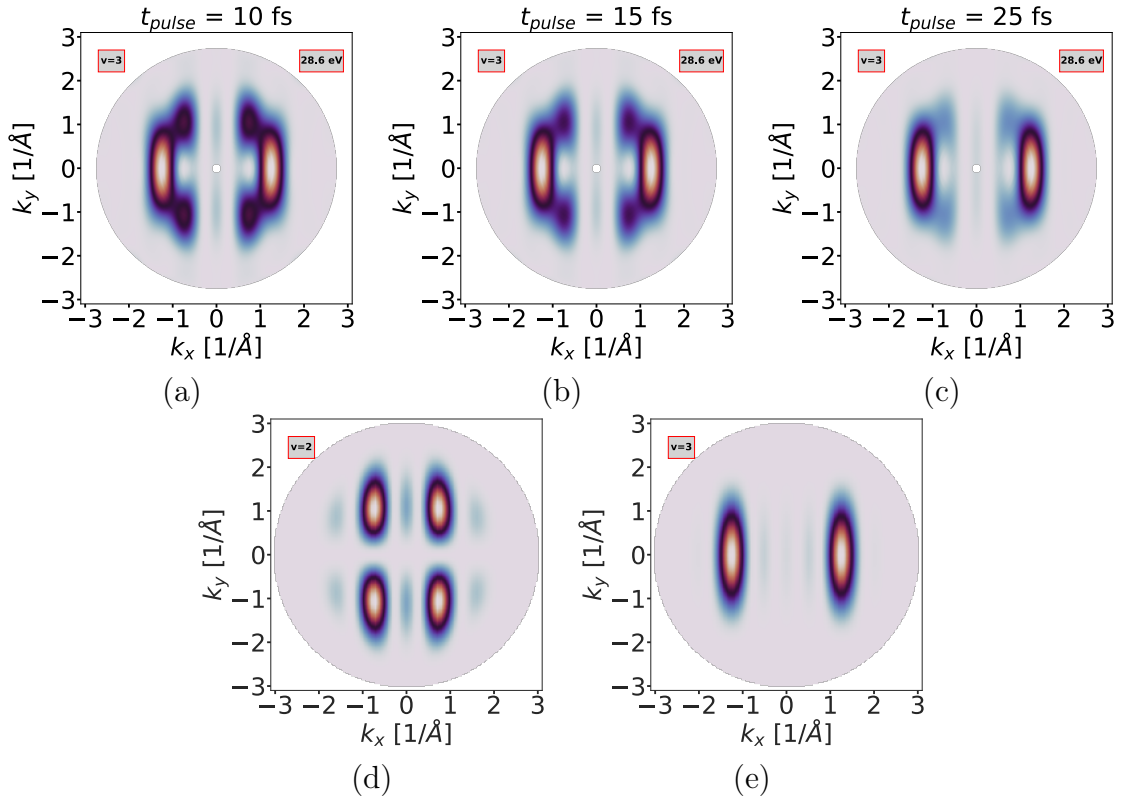
Fig. 20: Comparison of the occupied state momentum maps for tetracene: t-SURFF PAD appearing at $E_{\text{kin}} = \omega - \epsilon_3 = 28.6$ eV for different pulse lengths of (a) 10 fs, (b) 15 fs and (c) 25 fs and Fourier transforms of the (d) H-1 and (e) H-2 for tetracene.
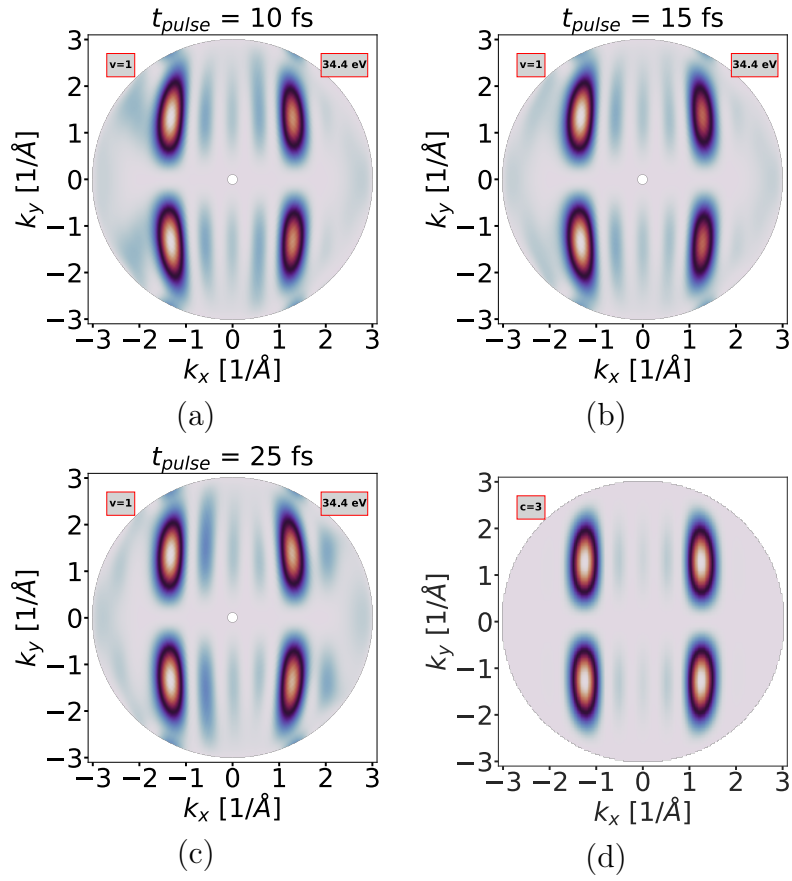
Fig. 21: Comparison of the excited state momentum maps for tetracene: t-SURFF PAD appearing at $E_{\mathrm{kin}} = \omega - \epsilon_1 + \omega_{\mathrm{pump}} = 34.4$ eV for different pulse lengths of (a) 10 fs, (b) 15 fs and (c) 25 fs and Fourier transform of the (d) L+2 for tetracene.
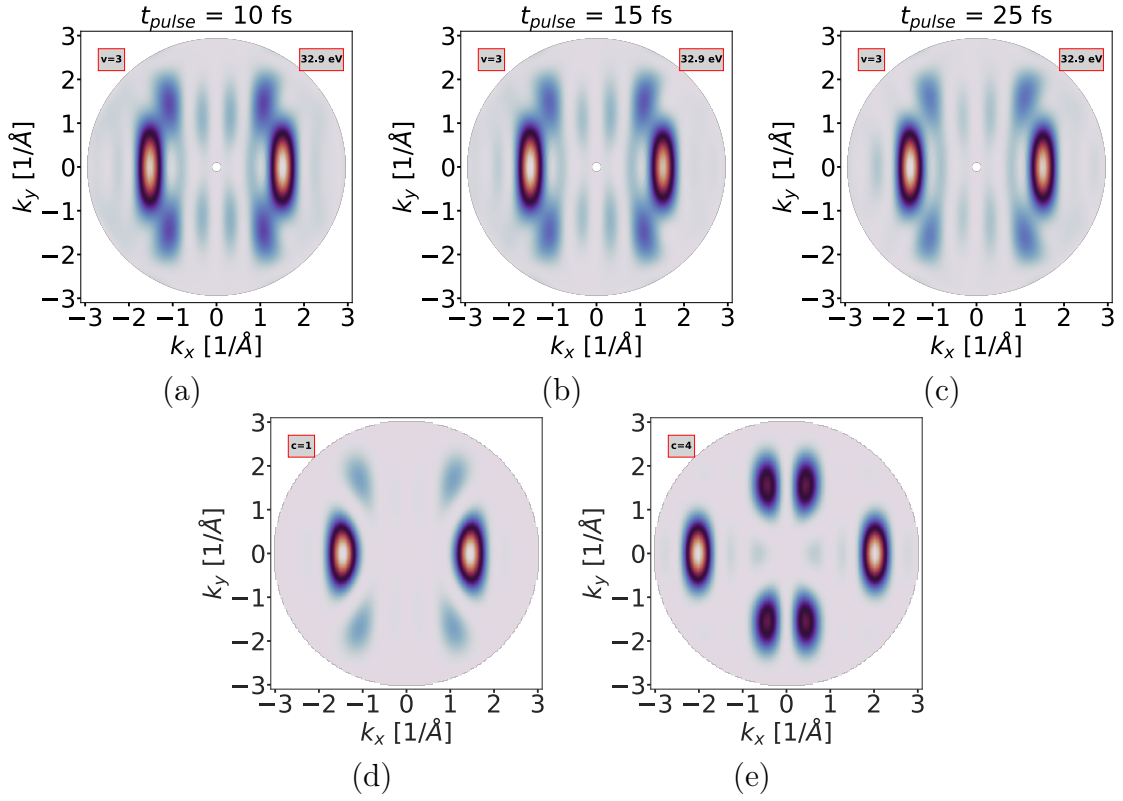
Fig. 22: Comparison of the excited state momentum maps for tetracene: t-SURFF PAD appearing at $E_{\mathrm{kin}} = \omega - \epsilon_3 + \omega_{\mathrm{pump}} = 32.9$ eV for different pulse lengths of (a) 10 fs, (b) 15 fs and (c) 25 fs and Fourier transforms of the (d) L and (e) L+3 for tetracene.

H-2 → L transition contributes by 45%. Additionally, the $v = 3$ map reveals features corresponding to the L+3, driven by the H-2 → L+3 transition. However, this contribution, which is minor at 1%, is not observed in the coherent sum, suggesting that these features diminish with longer pulse durations. In contrast, the incoherent sum maps in panel (d) of Fig. 23 and Fig. 24 show no significant deviations from the other methods, as the dominant single state contributions prevail.
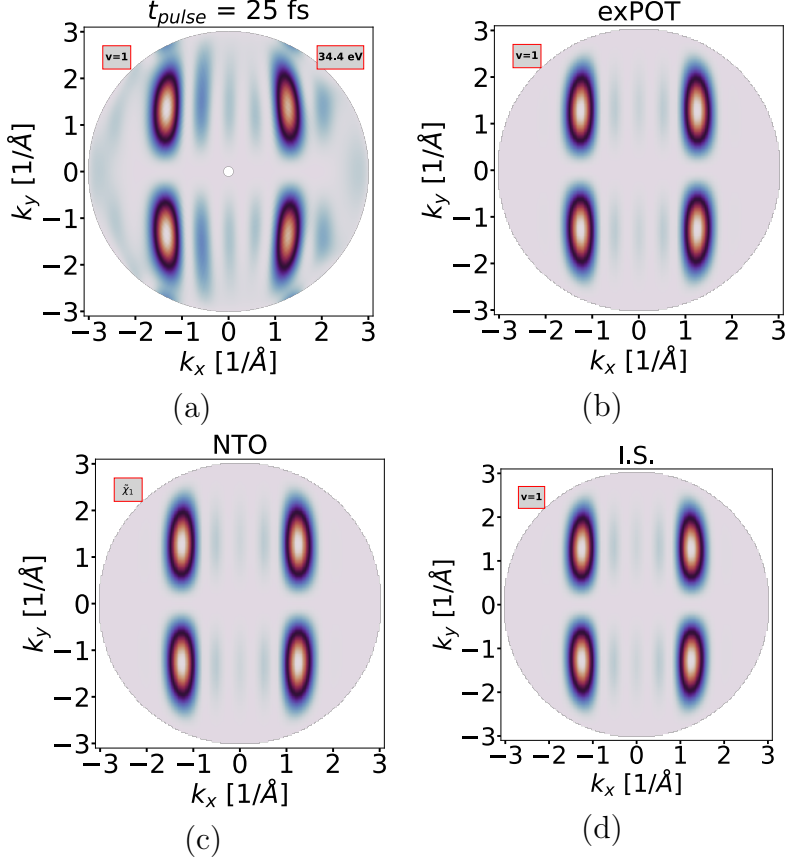
Fig. 23: Comparison of t-SURFF and exPOT momentum maps for tetracene: PADs from (a) t-SURFF evaluated at $E_{kin} = \omega - \epsilon_1 + \omega_{pump} = 34.4$ eV, (b) the exPOT approach [Eq. 63], (c) a single NTO [Eq. 69] and (d) an incoherent summation of the orbital contributions different from the coherent sum present in Eq. 63 for the exPOT formalism.
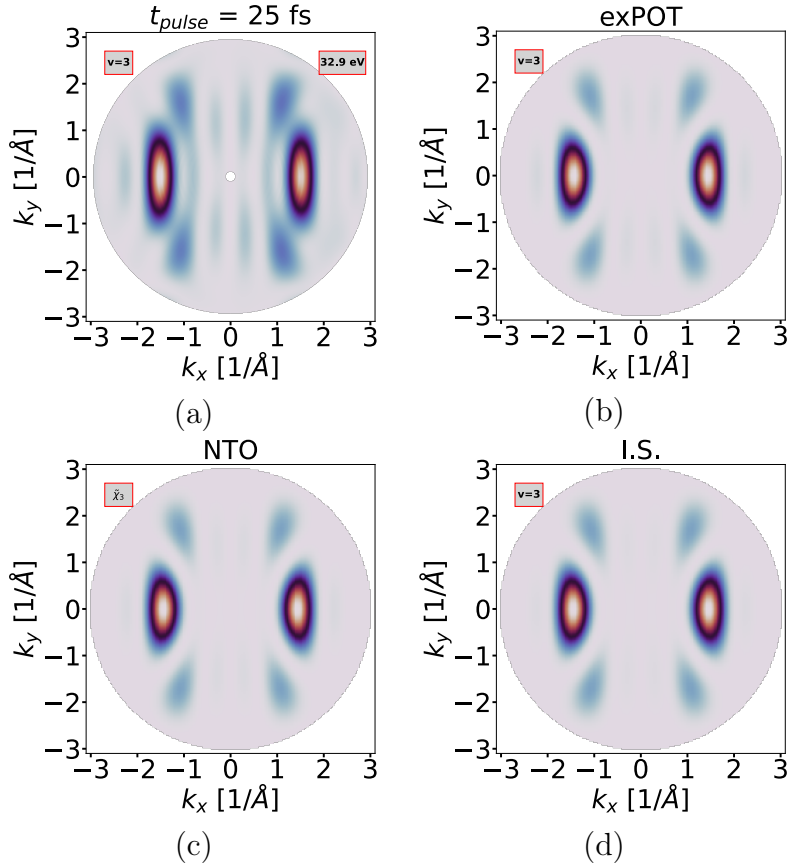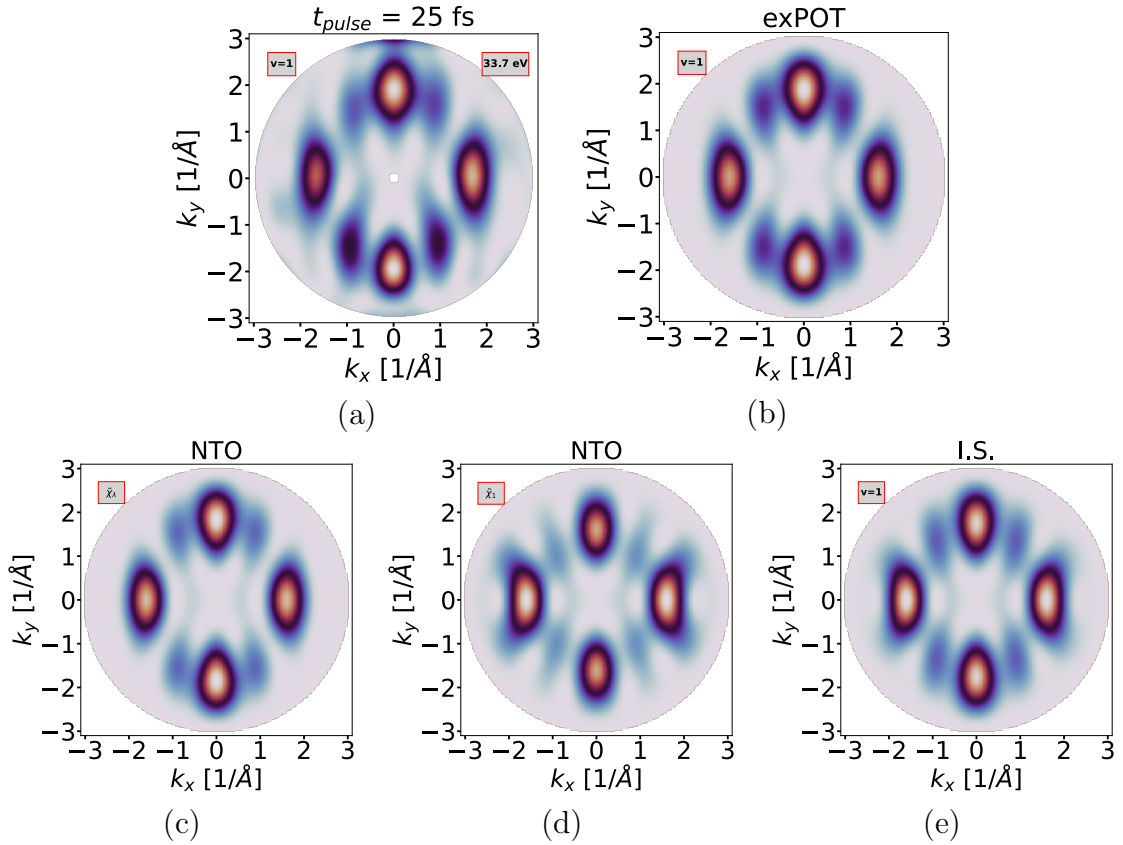
Fig. 24: Comparison of t-SURFF and exPOT momentum maps for tetracene: PADs from (a) t-SURFF evaluated at $E_{\text{kin}} = \omega - \epsilon_3 + \omega_{\text{pump}} = 32.9$ eV, (b) the exPOT approach [Eq. 63], (c) a single NTO [Eq. 69] and (d) an incoherent summation of the orbital contributions different from the coherent sum present in Eq. 63 for the exPOT formalism.

3.3.2 Fluorene

We now focus on the results for fluorene, first discussing a comparison of the absorption spectra obtained from LR-TDDFT and RT-TDDFT shown in Fig. 25 panel (a). Here, we find good agreement between the profiles of the spectra, as both exhibit the two strongest peaks in similar energy ranges. As for the first peak, it can be seen that the position obtained from RT-TDDFT (red dashed line) sits beneath the LR-TDDFT (red asterisk) one. As RT-TDDFT is also employed in the ARPES simulation, we proceed to use the RT-TDDFT value of 4.40 eV for the pump pulse energy. In panel (b) the absolute squares of the Casida contributions for the excitation at 4.48 eV are shown. All of the displayed transitions are allowed per the C_{2v} symmetry rules in Tab. 3. The contributions reveal that the first exciton in fluorene is mainly made up of a H $\to$ L and a H $\to$ L+1 transition. Consequently, in a momentum map of this excited state, we expect to observe a weighted superposition of the L and L+1 at a kinetic energy corresponding to the photohole residing in the H state. The additionally visible H-2 $\to$ L, H-2 $\to$ L+1 as well as the H-3 $\to$ L+3 transitions will be excluded from further analysis as their contributions are significantly smaller compared to the transitions involving the H.
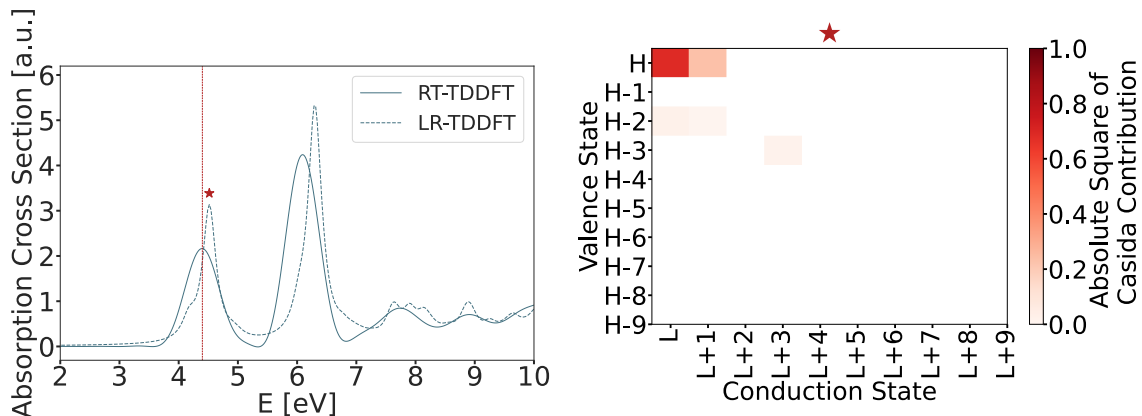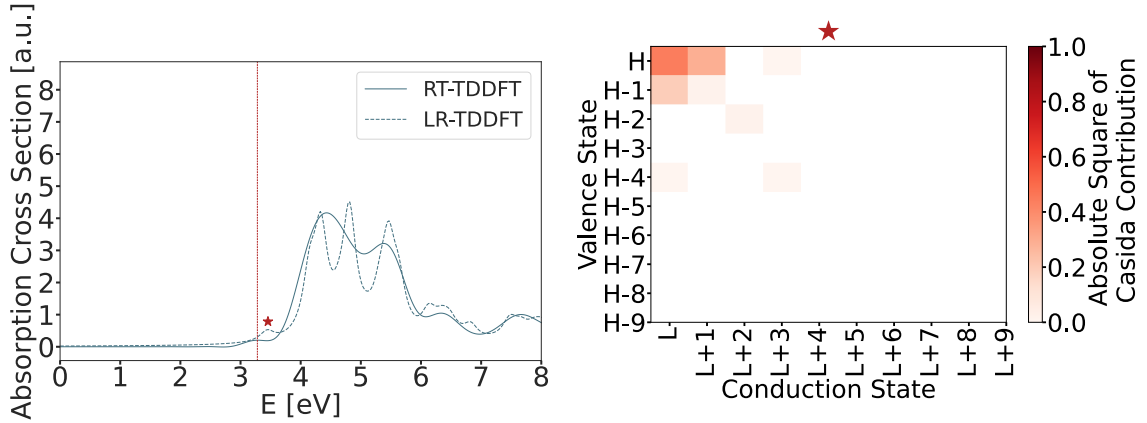

Fig. 25: (a) Converged absorption spectra for fluorene calculated with OCTOPUS in RT-TDDFT (full line) and from Casida's formalism within LR-TDDFT (dashed line). The excitation energy used in the pump-probe simulation is marked with a vertical red dashed line, while the Casida excitation energy is marked with a red asterisk. (b) Absolute square of the occupied-unoccupied Casida transition contributions for the excited state marked with a red asterisk.

Figure 26 presents the kinetic energy photoemission spectrum for fluorene for pulse durations of 10 fs, 15 fs, and 25 fs. As discussed above, we focus on the emission appearing at $E_{\text{kin}} = \omega - \epsilon_1 + \omega_{\text{pump}}$, i.e. the transition associated with the H marked by the rightmost vertical dashed line. As the pulse length increases, we again observe that the peaks in the spectrum become narrower, consistent with the Heisenberg uncertainty principle.

For fluorene, the excitation under consideration leads to an exciton structure consisting of a single hole state and multiple conduction states, a situation labeled as "case (iv)" in the paper by Kern et al. [7]. The Fourier transforms of the two conduction states, L and L+1, which together form the exciton structure involving
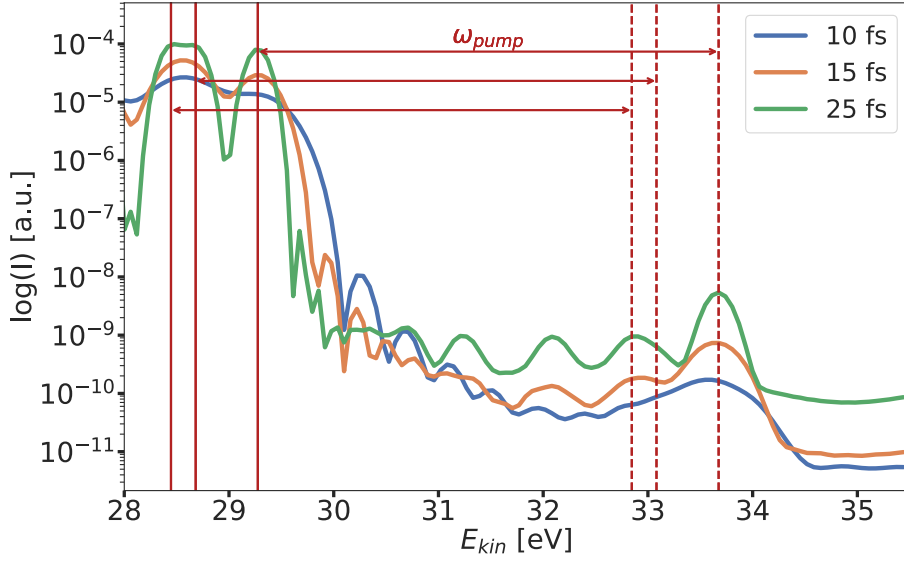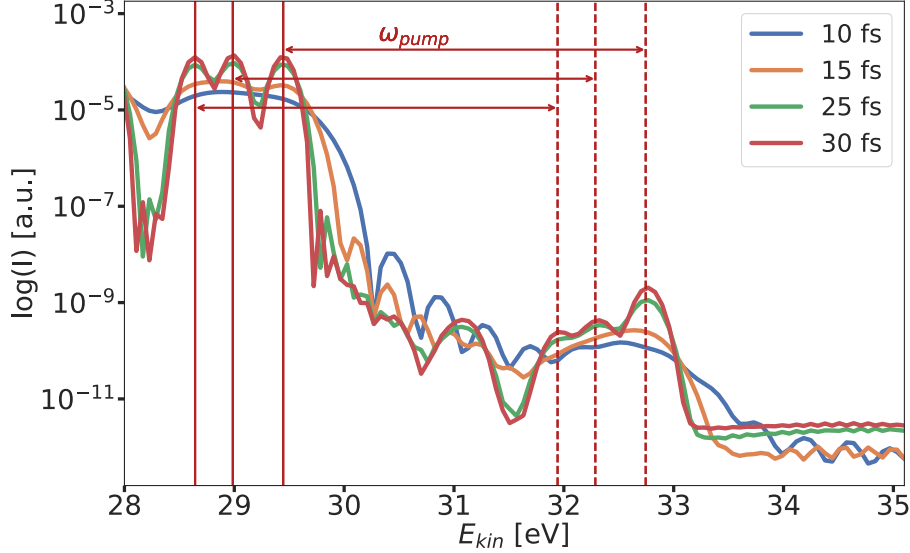
Fig. 26: Total angle-integrated photoelectron intensity from t-SURFF for different pulse durations for fluorene. The vertical solid lines mark the energy levels corresponding to the occupied states, while the vertical dashed lines denote the energy levels of the excited states. The horizontal arrows indicate the pump pulse energy $\omega_{\mathrm{pump}} = 4.40$ eV used in the simulation.

the H state, are shown in Fig. 27. To interpret the patterns seen in the momentum maps in Fig. 28, we analyze the PAD features. Comparing the t-SURFF result in panel (a) to the exPOT result from Eq. 63 in panel (b) and the sum of NTOs from Eq. 69 in panel (c), we observe good agreement in the main features produced by all methods. The PADs are predominantly characterized by contributions from the L state, with additional enhancements at $k_x = \pm 1$ Å corresponding to the L+1 state. This observation is consistent with the Casida analysis, where the H $\to$ L transition accounts for 68% , while the H $\to$ L+1 transition contributes 24%. Notably, accurate reproduction of the intensity drop between $k_y = -0.5$ Å and $k_y = 0.5$ Å requires the coherent sum from the exPOT approach or the sum of the first three NTOs with contributions of 93%, 3% and 2%. This is further confirmed by panel (d) and panel (e), where the mainly contributing single NTO as well as an incoherent sum fail to show this reduction in intensity.
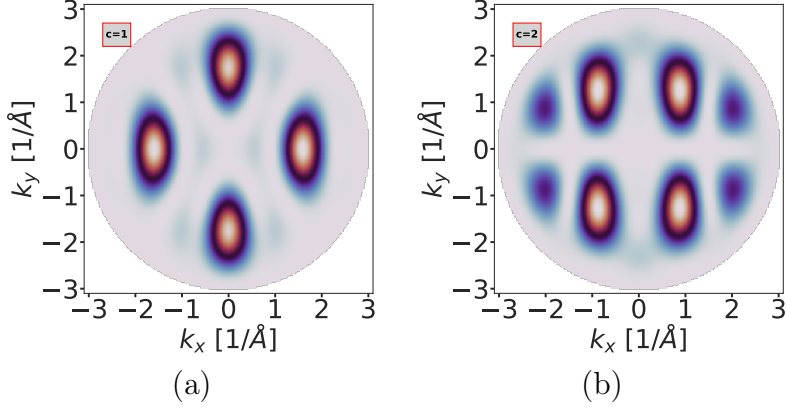
Fig. 27: Fourier transforms of the unoccupied states involved in the $E_{\mathrm{kin}} = \omega - \epsilon_1 + \omega_{\mathrm{pump}} = 33.1$ eV excitation for fluorene: PAD of the (a) L and (b) L+1.

Fig. 28: Comparison of t-SURFF and exPOT momentum maps for fluorene: PADs from (a) t-SURFF evaluated at $E_{\mathrm{kin}} = \omega - \epsilon_1 + \omega_{\mathrm{pump}} = 33.1$ eV, (b) the exPOT approach [Eq. 63], (c) sum of NTOs [Eq. 69], (d) single NTO with the largest contribution λ_1 and (e) an incoherent summation of the orbital contributions different from the coherent sum present in Eq. 63 for the exPOT formalism.

3.3.3 Chrysene

For chrysene, the optical absorption spectrum in Fig. 29 panel (a) reveals an excitation at 3.3 eV for the RT-TDDFT marked by a vertical red dashed line and 3.4 eV for the LR-TDDFT calculation marked by a red asterisk. Despite the relatively low oscillator strength this excitation is further investigated, due to its non-trivial transition density matrix elements shown in Fig. 29 panel (b). We observe that this exciton involves multiple transitions, combining the entangled state character from the tetracene example and the coherent superposition from the fluorene case. Specifically, this excited state is comprised of the H $\to$ L and H $\to$ L+1 transitions, as well as the H-1 $\to$ L and H-1 $\to$ L+1 transitions, though with differing relative contributions. This is comparable to the exciton structure discussed for fluorene, where transitions from the H state to multiple conduction states dominate. Additionally, as seen with tetracene, contributions from lower-lying hole states, e.g. the H-1, create a more complex excitonic structure. Consequently, it is expected that the momentum maps at the kinetic energies corresponding to the ionization potentials of H and H-1 will resemble the Fourier transforms of differently weighted superpositions of the L and L+1 states.

Fig. 29: (a) Converged absorption spectra for chrysene calculated with OCTOPUS in RT-TDDFT (full line) and from Casida's formalism within LR-TDDFT (dashed line). The excitation energy used in the pump-probe simulation is marked with a vertical red dashed line, while the Casida excitation energy is marked with a red asterisk. (b) Absolute square of the occupied-unoccupied Casida transition contributions for the excited state marked with a red asterisk.

Figure 30 displays the kinetic energy photoemission spectrum for chrysene, subject to pulse durations of 10 fs, 15 fs, 25 fs, and 30 fs. The addition of the 30 fs pulse duration leads to an enhanced energy resolution of approximately $\Delta E \approx 0.11$ eV, allowing for a more precise investigation of the emission features. We concentrate on the emissions identified at $E_{\text{kin}} = \omega - \epsilon_1 + \omega_{\text{pump}} = 32.7$ eV and $E_{\text{kin}} = \omega - \epsilon_2 + \omega_{\text{pump}} = 32.3$ eV, corresponding to the transitions linked to the H and H-1 states, respectively, which are marked by the two rightmost red vertical dashed lines. The transition density matrix illustrated in Fig. 29 panel (b) emphasizes the significance of these emissions, as they exhibit the largest contributions. Notably, as the pulse length is extended, the spectral peaks exhibit a tendency to narrow, again aligning

with the Heisenberg uncertainty principle. It is also worth noting that the intensity, relative to that of tetracene and fluorene, is lower by 10 orders of magnitude, which can likely be attributed to a smaller oscillator strength.

Fig. 30: Total angle-integrated photoelectron intensity from t-SURFF for different pulse durations for chrysene. The vertical solid lines mark the energy levels corresponding to the occupied states, while the vertical dashed lines denote the energy levels of the excited states. The horizontal arrows indicate the pump pulse energy $\omega_{\mathrm{pump}} = 3.3$ eV used in the simulation.

For chrysene, the momentum maps given by the Fourier transform of the involved conduction states for both the $v = 1$ and $v = 2$ transitions, namely the L and L+1, are shown in Fig. 31. Specifically, the excited state consists of H $\rightarrow$ L (44%), H $\rightarrow$ L+1 (44%), H-1 $\rightarrow$ L (19%), and H-1 $\rightarrow$ L+1 (2%). Examining the momentum maps in Fig. 32, the t-SURFF result evaluated for $E_{\mathrm{kin}} = \omega - \epsilon_1 + \omega_{\mathrm{pump}}$ = 32.7 eV (panel (a)) aligns well with both the exPOT (panel (b)) approach and the first NTO map (panel (c)), as all methods capture the primary features of the L and L+1 Fourier transforms. However, the incoherent sum show (panel (d)) shows strong accentuations that are absent in the t-SURFF map, underlining the importance of the coherent sum to accurately describe the photoemission distributions. In contrast, for the maps in Fig. 33 for $v = 2$, the agreement between the t-SURFF and exPOT methods is poor. Several factors may contribute to this discrepancy. First, the exPOT formalism, which approximates the final state as a plane wave, does not capture asymmetries as effectively as the t-SURFF method, which does not rely on such an approximation. Second, due to the Heisenberg uncertainty principle, other nearby excitations may contribute to the momentum maps, complicating the analysis, particularly as the asymmetries in the t-SURFF maps and the similarities in the Fourier transforms of the involved conduction states make disentangling these contributions difficult. Additionally, the simultaneous application of pump and probe pulses in the ARPES simulation could introduce a potential source of error, as setups involving delays between the pulses have not been tested in this work. It should also be noted that the overall intensities are lower compared to the previously studied

54

molecules, which may lead to numerical issues becoming more significant. Lastly, the convergence tests for the optical absorption spectra, performed with a relatively short propagation time of 6.5 fs, may have introduced a slight shift in peak positions, potentially leading to an off-resonant excitation in the t-SURFF simulation.

(a) (b)
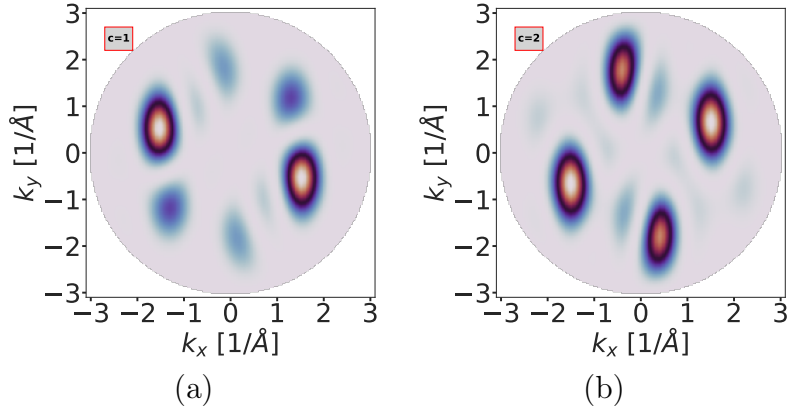
Fig. 31: Fourier transforms of the unoccupied states involved in the $E_{\mathrm{kin}} = \omega - \epsilon_1 + \omega_{\mathrm{pump}} = 32.7$ eV and $E_{\mathrm{kin}} = \omega - \epsilon_2 + \omega_{\mathrm{pump}} = 32.3$ eV excitations for chrysene: PAD of the (a) L and (b) L+1.
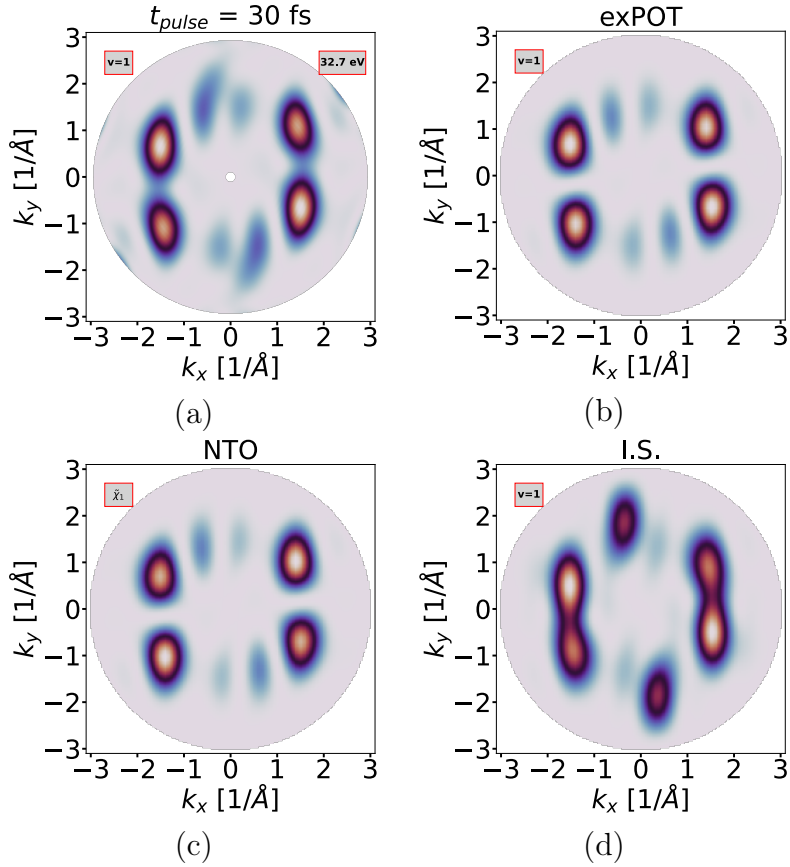
Fig. 32: Comparison of t-SURFF and exPOT momentum maps for chrysene: PADs from (a) t-SURFF evaluated at $E_{kin} = \omega - \epsilon_1 + \omega_{pump} = 32.7$ eV, (b) the exPOT approach [Eq. 63], (c) single NTO [Eq. 69] and (d) an incoherent summation of the orbital contributions different from the coherent sum present in Eq. 63 for the exPOT formalism.
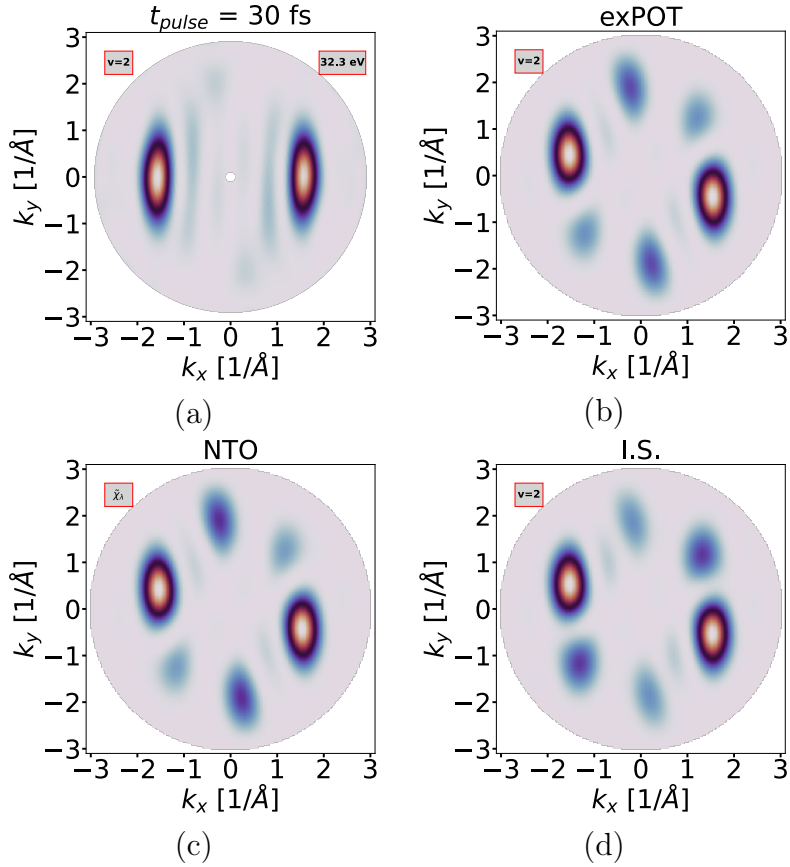
Fig. 33: Comparison of t-SURFF and exPOT momentum maps for chrysene: PADs from (a) t-SURFF evaluated at $E_{kin} = \omega - \epsilon_2 + \omega_{pump} = 32.3$ eV, (b) the exPOT approach [Eq. 63], (c) sum of NTOs [Eq. 69] and (d) an incoherent summation of the orbital contributions different from the coherent sum present in Eq. 63 for the exPOT formalism.

3.3.4 Picene

For picene, the optical absorption spectrum in Fig. 34 panel (a) shows a strong excitation at 4.33 eV for the RT-TDDFT (red dashed line) and 4.26 eV for the LR-TDDFT (red asterisk). This excitation is investigated further, despite not being the first peak in the spectrum, due to its high oscillator strength and the complex exciton structure illustrated by the transition density matrix elements in Fig. 34 panel (b). The involved transitions include H-1 → L+1, H-1 → L+2, H-2 → L+1, and H-2 → L+2, with varying contributions. Similar to tetracene and chrysene, transitions from lower-lying hole states lead to a more complex exciton structure. Therefore, the momentum maps corresponding to the ionization potentials of H-1 and H-2 are expected to resemble the Fourier transforms of weighted superpositions of the L+1 and L+2 states.
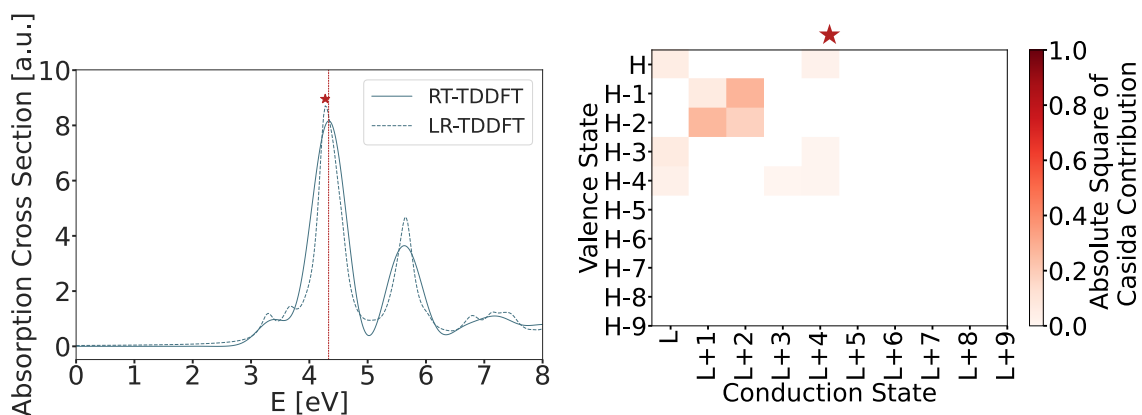
Fig. 34: (a) Converged absorption spectra for picene calculated with OCTOPUS in RT-TDDFT (full line) and from Casida's formalism within LR-TDDFT (dashed line). The excitation energy used in the pump-probe simulation is marked with a vertical red dashed line, while the Casida excitation energy is marked with a red asterisk. (b) Absolute square of the occupied-unoccupied Casida transition contributions for the excited state marked with a red asterisk.

Figure 35 presents the kinetic energy photoemission spectrum for picene, analyzed with pulse durations of 10 fs, 15 fs, 25 fs, and 30 fs. We focus on the emissions observed at $E_{\text{kin}} = \omega - \epsilon_2 + \omega_{\text{pump}} = 33.5$ eV and $E_{\text{kin}} = \omega - \epsilon_3 + \omega_{\text{pump}} = 33.1$ eV, which correspond to transitions associated with the H-1 and H-2 states, respectively, as highlighted by the two leftmost red vertical dashed lines. The transition density matrix depicted in Fig. 34 panel (b) highlights the importance of these emissions, as they account for the largest contributions. Furthermore, with the increase in pulse length, the spectral peaks tend to become narrower, consistent with the principles outlined by the Heisenberg uncertainty principle.

For picene, the momentum maps for the $v = 2$ and $v = 3$ transitions, corresponding to emissions at kinetic energies related to ϵ_2 and ϵ_3, involve contributions from the conduction states L+1 and L+2. The corresponding PADs are shown in Fig. 36. The transitions consist of H-1 → L+1 (7%), H-1 → L+2 (27%), H-2 → L+1 (26%), and H-2 → L+2 (18%). In the case of $v = 2$, the momentum maps in Fig. 37 show good agreement between the t-SURFF results (panel (a)) and the exPOT ap-
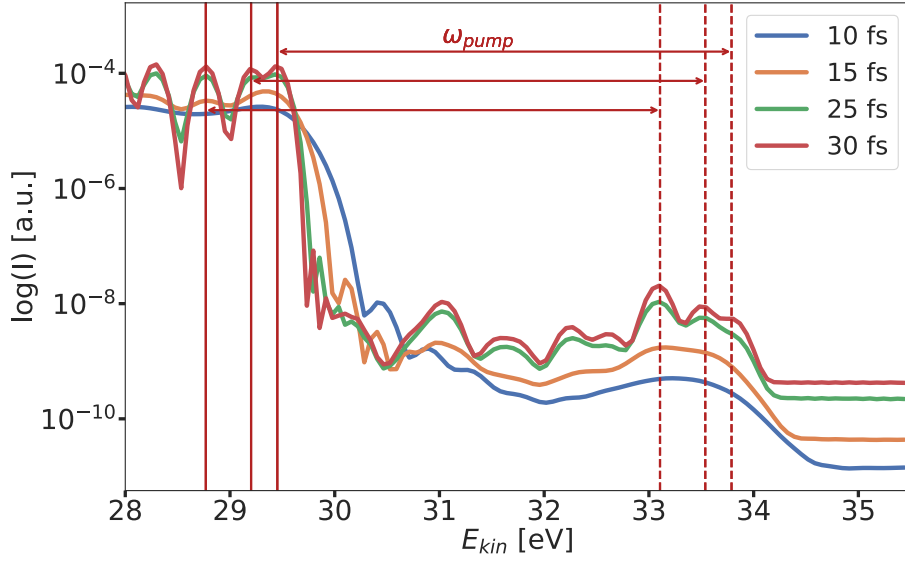
Fig. 35: Total angle-integrated photoelectron intensity from t-SURFF for different pulse durations for picene. The vertical solid lines mark the energy levels corresponding to the occupied states, while the vertical dashed lines denote the energy levels of the excited states. The horizontal arrows indicate the pump pulse energy $\omega_{\mathrm{pump}} = 4.34$ used in the simulation.

proach (panel (b)) as well as the sum of NTOs (panel (c)), as all methods capture the primary overlapping features from the Fourier transforms of the L+1 and L+2 conduction states. However, the incoherent sum (panel (d)) shows clear differences, with noticeable features that are not present in the t-SURFF map, highlighting the importance of coherent summation for accurately capturing the photoemission distributions. For the PADs resulting from the $v = 3$ transition (Fig. 38), the disagreement between the t-SURFF and exPOT methods persists. Possible reasons for this poor agreement are the same as those discussed for the $v = 2$ transition in *chrysene*, including limitations of the exPOT formalism, potential contributions from nearby excitations, and the setup of the pump-probe pulses.
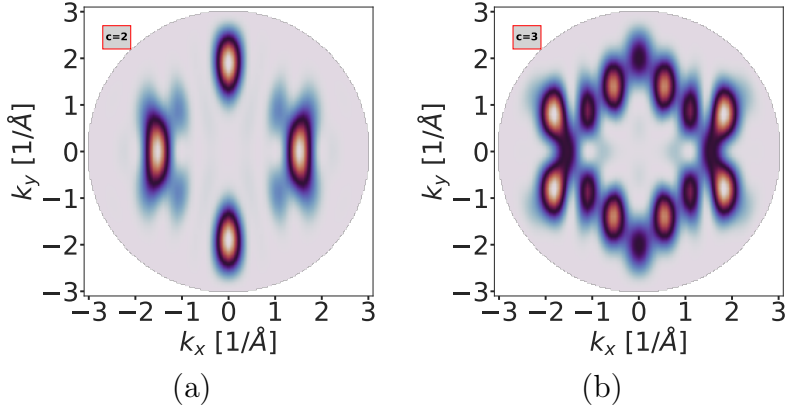
Fig. 36: Fourier transforms of the unoccupied states involved in the $E_{\text{kin}} = \omega - \epsilon_2 + \omega_{\text{pump}} = 33.5$ eV and $E_{\text{kin}} = \omega - \epsilon_3 + \omega_{\text{pump}} = 33.1$ eV excitations for picene: PAD of the (a) L+1 and (b) L+2.
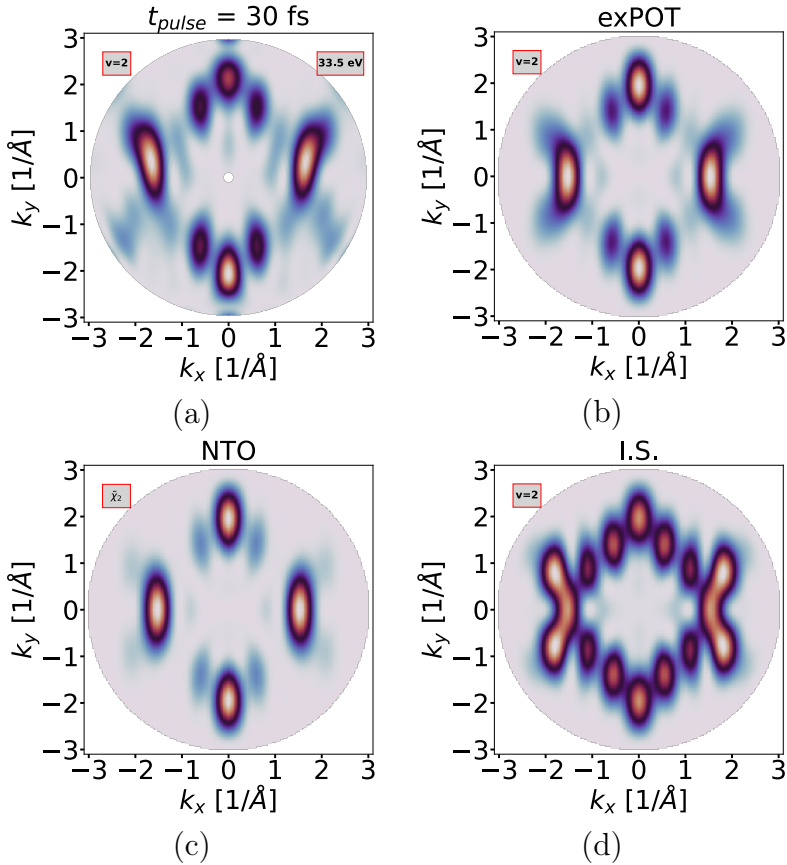
Fig. 37: Comparison of t-SURFF and exPOT momentum maps for picene: PADs from (a) t-SURFF evaluated at $E_{\text{kin}} = \omega - \epsilon_2 + \omega_{\text{pump}} = 33.5$ eV, (b) the exPOT approach [Eq. 63], (c) single NTO [Eq. 69] and (d) an incoherent summation of the orbital contributions different from the coherent sum present in Eq. 63 for the exPOT formalism.
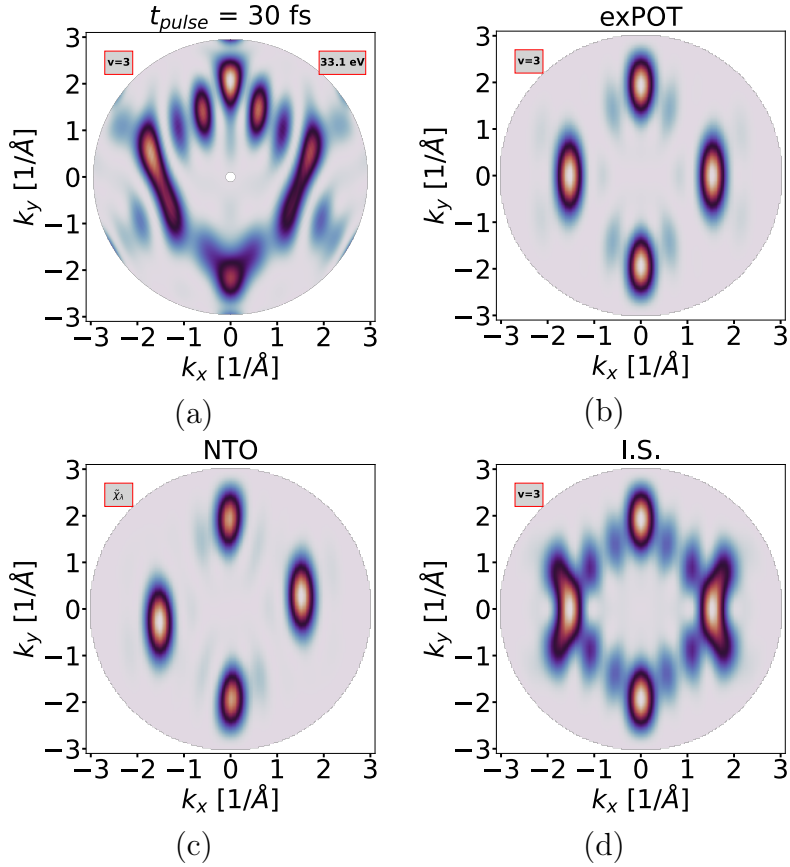
Fig. 38: Comparison of t-SURFF and exPOT momentum maps for picene: PADs from (a) t-SURFF evaluated at $E_{\mathrm{kin}} = \omega - \epsilon_3 + \omega_{\mathrm{pump}} = 33.1$ eV, (b) the exPOT approach [Eq. 63], (c) sum of NTOs [Eq. 69] and (d) an incoherent summation of the orbital contributions different from the coherent sum present in Eq. 63 for the exPOT formalism.

3.3.5 Sexithiophene

The optical absorption spectrum of sexithiophene (6T) ab obtained from TDDFT using the ALDA kernel is characterized by two prominent transitions polarized along 6T's long molecular axis. The first peak visible at 2.01 eV in Fig. 39 is composed of a main contribution from the H $\rightarrow$ L transition of 94% in addition to 3 smaller contributions from H-2 $\rightarrow$ L of 1%, H $\rightarrow$ L+1 of 3% and H-1 $\rightarrow$ L+2 of 1% as shown in panel (a) of Fig. 40. Note that, this result was obtained using a local and frequency-independent LDA kernel when solving Casida's equation [Eq. 50] and when calculating the occupied and unoccupied states. However, the adiabatic LDA functional ALDA, the extension of LDA for time-dependent density, was shown to be insufficient when performing RT-TDDFT calculations for 6T to represent the e-h interactions giving rise to the mixed excitation [71]. The use of ALDA falsely features a second peak in the spectrum at a slightly higher energy. In our case the Casida spectrum from LR-TDDFT features a peak at 2.8 eV in Fig. 39 with a main contribution from H-1 $\rightarrow$ L+1 of 50% depicted in panel (b) of Fig. 40.

To correctly capture the excited state picture of the lowest excitation in 6T it is adviced to use many-body perturbation theory (MBPT) to calculate optical excitations. Hereby, the quasiparticle energies are calculated via the GW approach and solving the Bethe-Salpeter equation (BSE) $H^{BSE}A^\lambda = E^\lambda A^\lambda$ provides excitation energies and wavefunctions of the e-h pairs [72, 73]. GW+BSE leads to exciton contributions of 74% for H $\rightarrow$ L and 20% for H-1 $\rightarrow$ L+1 for the first excitation, while the second peak vanishes. This indicates that the use of LDA splits the lowest excitation into two peaks, due to an incorrect description of correlation effects. This disagreement between the TDDFT and MBPT results stems from the inclusion of the $\hat{H}^{dir}$ term in the effective two-particle hamiltonian $\hat{H}^{BSE} = \hat{H}^{diag} + 2\gamma_x\hat{H}^x + \gamma_c\hat{H}^{dir}$. The diagonal term $\hat{H}^{diag}$ describes single-particle transitions. $\hat{H}^x$ is the repulsive e-h exchange term and includes local field effects. The direct term $\hat{H}^{dir}$ represents the attractive e-h interaction, as it incorporates the short-range Coloumb interaction. The parameters γ_x and γ_c specify whether singlet or triplet excitations are calculated. The result in [71] does not change when the $\hat{H}^x$ term is excluded but it leads to a 100 % H $\rightarrow$ L transition when both, the $\hat{H}^x$ and $\hat{H}^{dir}$ term, are omitted. Therefore, it was concluded that the mixed character of the first exciton in 6T is due to e-h correlation effects described by $\hat{H}^{dir}$. In Casida's equation the e-h correlation can be accounted for via the choice of the XC functional in the kernel in Eq. 52. In the case of 6T the LC-PBE0* functional, a long-range corrected PBE0 hybrid functional with optimally tuned parameters for the inclusion of exact and DFT exchange, is used in [74]. This leads to contributions of 90% for H $\rightarrow$ L and 7 % for the H-1 $\rightarrow$ L+1 transition. Therefore, despite the additional computational cost and the inclusion of long-range exchange interactions in LC-PBE0*, a significant disagreement between TDDFT and MPBT remains.
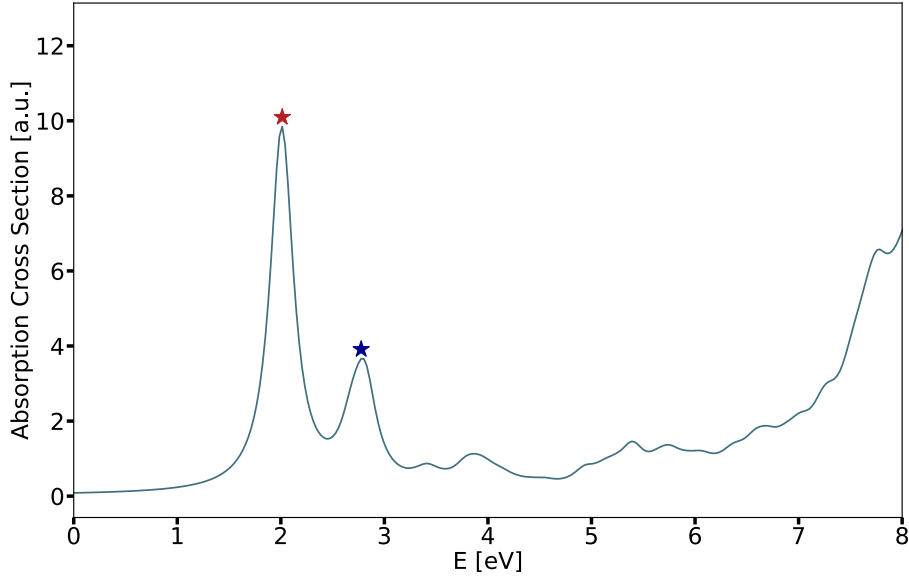
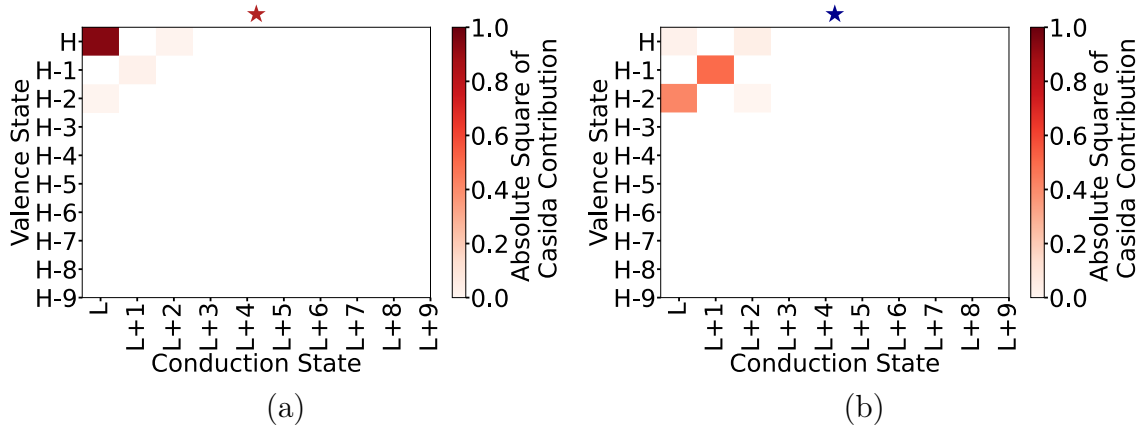Fig. 39: Linear response absorption spectrum for 6T along x direction from Casida formalism.

Fig. 40: Absolute square of the Casida transition density matrix values for 6T for (a) the first peak at 2.01 eV and (b) the second peak at 2.8 eV.

3.3.6 NTCDA

The LDA Casida calculation for NTCDA reveals that most transitions that are present in Fig. 12 panel (c) are contributing to the strongest excitation in the absorption spectrum for the x polarization direction in Fig. 41 (a) at 6.22 eV. The decomposition into electron-hole transitions for this peak can be seen in Fig. 41 (b). The additional H-4 $\rightarrow$ L+4 ($B_{1u} \rightarrow B_{3g}$) transition is also electronically allowed, however the transition dipole moment is relatively small with a value of 0.003 eV·Å and therefore not visible in Fig. 12 panel (c). As this excitation shows PADs at different kinetic energies that consist of the Fourier transform of a coherent sum of different unoccupied states, it would be an interesting example to validate Eq. 63. However, as the LDA functional used in the Casida calculation, the orbital ordering issue remains. A functional that promises to solve this problem is the HSE06, as

63

it incorporates exact HF exchange in the short-range [20]. However, in this particular case the ground state calculation for 48 states with the OCTOPUS code took over 1 day compared to 12 seconds for the LDA functional. Considering that a full pump-probe ARPES simulation based on the LDA functional takes around 1-2 days for molecules of similar size, it has been decided to not further consider NTCDA for the TDDFT calculations.

(a) (b)
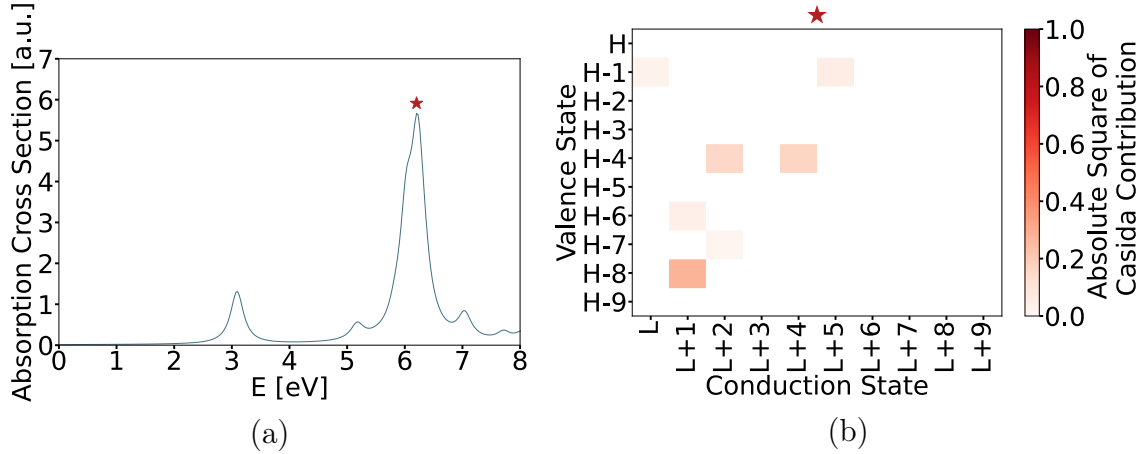
Fig. 41: Casida calculation results for NTCDA: (a) linear response absorption spectrum along x direction and (b) absolute square of the Casida transition density matrix values for the strongest peak at 6.22 eV.

4 Conclusions and Outlook

The goal of this Master's thesis has been to provide further theoretical support for a recently developed approach that extends photoemission orbital tomography (POT) to the description of optically excited states, termed exPOT [7]. This theoretical method promises to provide insight into the connection between momentum maps, as derived from femtosecond pump-probe photoemission experiments, and the spatial structure of excitons in organic molecular systems. To this end, momentum maps computed within exPOT have then been validated by real-time time-dependent density functional theory simulations, thereby confirming that the excited states represent a coherent superposition of multiple single-particle excitations.

In this chapter, we review the core conclusions of this thesis and discuss prospective opportunities for follow-up studies. Initially, we have developed a computationally efficient prescreening method to predict excited states with non-trivial transition density matrices based on ground state DFT properties. This approach has combined the symmetry of Kohn-Sham orbitals, the strength of transition dipole moments, and energy differences between unoccupied and occupied KS orbitals to identify suitable candidate molecules. Out of a series of planar π-conjugated molecules, the prescreening has identified tetracene, fluorene, chrysene, and picene as promising candidates for further analysis. Molecules that have not been further considered have failed the prescreening mainly because the transition density matrix is expected to exhbiti only one single dominant contribution and therefore show no potential for testing the exPOT approach for non-trivial cases. Moreover, they have either shown insufficient energy differences between excited states, making it difficult to avoid degeneracies, or the involved unoccupied states have displayed indistinguishable momentum map features, limiting their suitability for the exPOT approach.

Next, for the chosen set of molecules, optical absorption spectra have been obtained using real-time time-dependent density functional theory (RT-TDDFT), which perturbs the system with a δ-pulse to reveal potential pump pulse energies, and linear response time-dependent density functional theory (LR-TDDFT), which solves Casida's equation to quantify the corresponding exciton characteristics. The convergence of the RT-TDDFT spectrum has been tested with respect to grid spacing and simulation box radius, though not the propagation time, which could improve the agreement between RT-TDDFT and LR-TDDFT spectra due to enhanced energy resolution, particularly for higher-energy excitations. This measure may also result in a shift in the evaluated pump pulse energy values.

Lastly, momentum maps predicted by the exPOT approach have been successfully validated against time-dependent surface flux (t-SURFF) simulations. The extension of the POT formalism to exPOT has revealed that photoemission from bound electron-hole pairs can occur at multiple kinetic energies as seen in the example of tetracene. Additionally, it has been shown that in the case of transitions from a single valence state to several conduction states, as for fluorene, rationalizing the appearing momentum map features necessitates the incorporation of a coherent sum over unoccupied orbitals. In the cases of chrysene and picene, we combine the insight from the tetracene and fluorene examples as we observe excitation profiles

containing emissions at different kinetic energies that involve the same conduction states, however differently weighted. While the momentum maps for higher-lying excitations in chrysene and picene exhibited convincing agreement between the exPOT and t-SURFF approaches, the same level of correspondence has not been achieved for the lower-lying excitations. This difference can be attributed to several factors. This includes the limitations of the plane wave approximation in exPOT, the influence of other energetically close excitations complicating the analysis due to the Heisenberg uncertainty principle, and potential errors introduced by simultaneous pump-probe setups or short propagation times in the convergence tests, possibly leading to off-resonant excitations. Moreover, exPOT has also been formulated using natural transition orbitals (NTOs), which give these quantities direct physical significance in photoemission experiments, as it has already been demonstrated in studies on excitons in buckminsterfullerene thin films [75].

Experimental validation for the molecules treated in this work has not yet been performed, thus this would be of significant interest. However, the challenges faced in preparing high-quality samples and generating stable and distinct excitons in these systems may hinder experimental validation, but future experiments could address these issues by refining sample preparation techniques, optimizing pump-probe setups, or utilizing higher-resolution photoemission methods to capture the predicted momentum maps.

A Appendix A: Prescreened Molecules

This appendix lists all molecules tested in the prescreening described in Sec. 3.1. Molecules highlighted in green represent those that are included and analyzed within the scope of this study. Orange highlights identify molecules that, while not fully explored here, are marked as promising for future investigation. Molecules without any highlighting were excluded as they do not meet the prescreening criteria.

Tab. 8: List of prescreened molecules: Green highlights indicate molecules considered in this work, orange highlights denote those of interest for further evaluation, while unmarked molecules do not pass the prescreening outlined in Sec. 3.1.

#	Molecule Shortname
1	1-hydroxy-benzo-fluoren
2	1P
3	1P_F
4	1T
5	2A
6	2A_F
7	2P
8	2T
9	3-hydroxy-benzo-fluoren
10	3A
11	3A_F
12	3P
13	3phenacene
14	3T
15	4A
16	4A_F
17	4phenacene
18	4T
19	5phenacene
20	5T
21	6T
22	ADF
23	F4TCNQ
24	NTCDA
25	PTCDA
26	TCNB
27	TCNE
28	TCNQ
29	TTF
30	alizarin12
31	alizarin13
32	azulene
33	coronene
34	cytosine
35	fluorene
36	guanine
37	indigo
38	p-ANBP
39	phenazine

B   Appendix B: Additional Optical Spectra Convergence Results

This appendix shows additional optical spectra convergence test results to the ones for tetracene discussed in Sec. 3.2 for the remaining investigated molecules, namely fluorene, chrysene and picene.

Fluorene
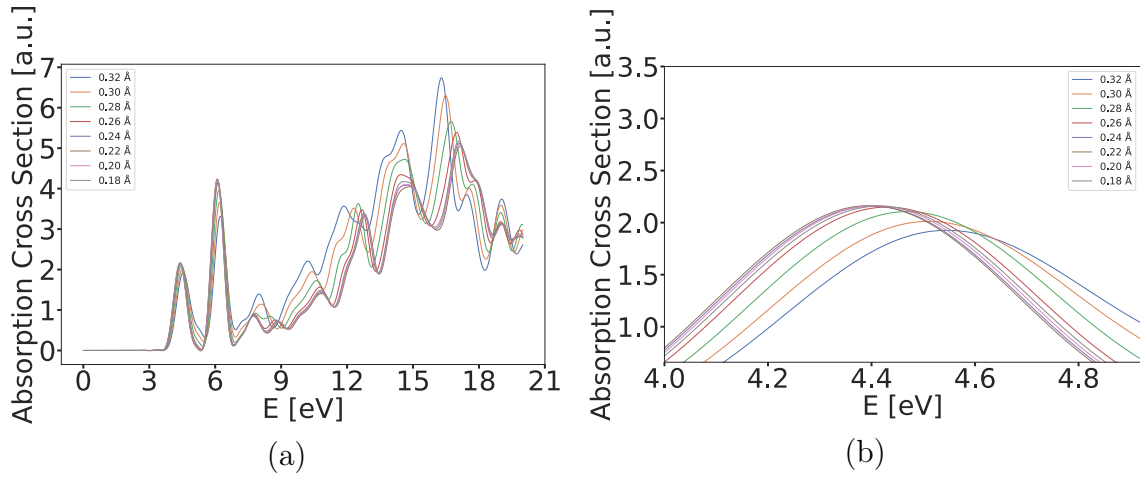
Fig. 42: Convergence of the RT-TDDFT optical spectrum upon excitation with a δ-kick with respect to the grid spacing for fluorene for the (a) full energy range and (b) zoomed in on the relevant excitation.
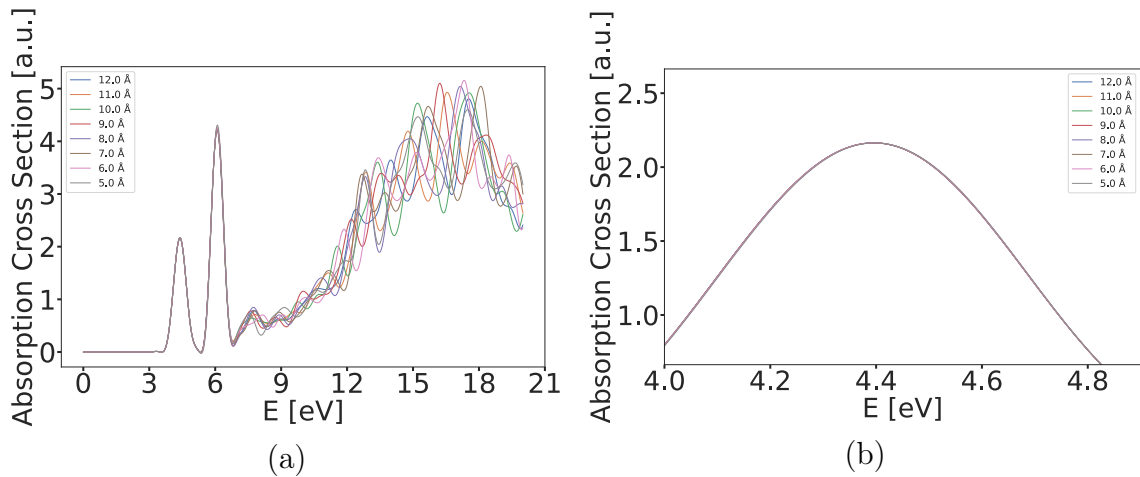
Fig. 43: Convergence of the RT-TDDFT optical spectrum upon excitation with a δ-kick with respect to the simulation box radius for fluorene for the (a) full energy range and (b) zoomed in on the relevant excitation.
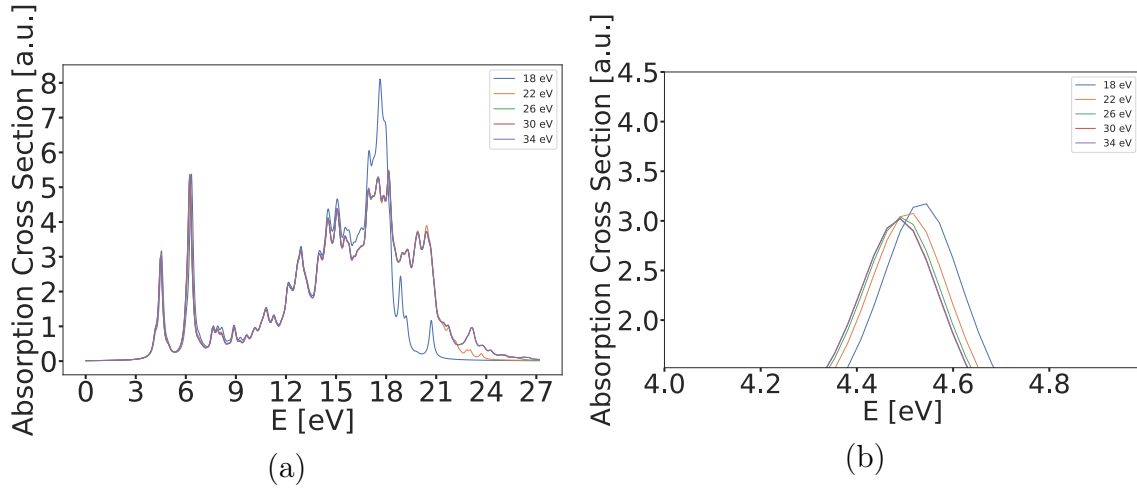
Fig. 44: Convergence of the Casida LR-TDDFT optical spectrum with respect to the Kohn-Sham energy window for fluorene for the (a) full energy range and (b) zoomed in on the relevant excitation.

Chrysene
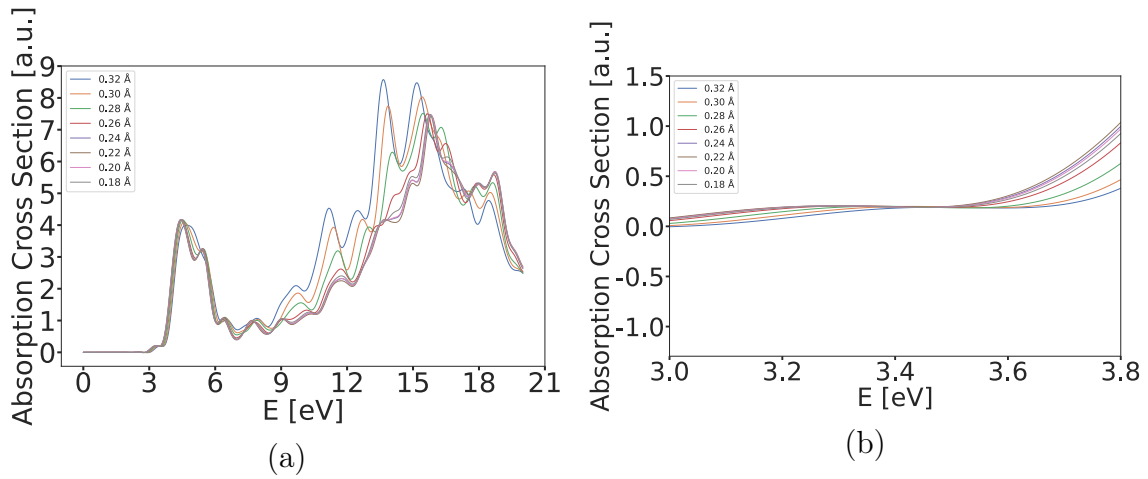
Fig. 45: Convergence of the RT-TDDFT optical spectrum upon excitation with a δ-kick with respect to the grid spacing for chrysene for the (a) full energy range and (b) zoomed in on the relevant excitation.
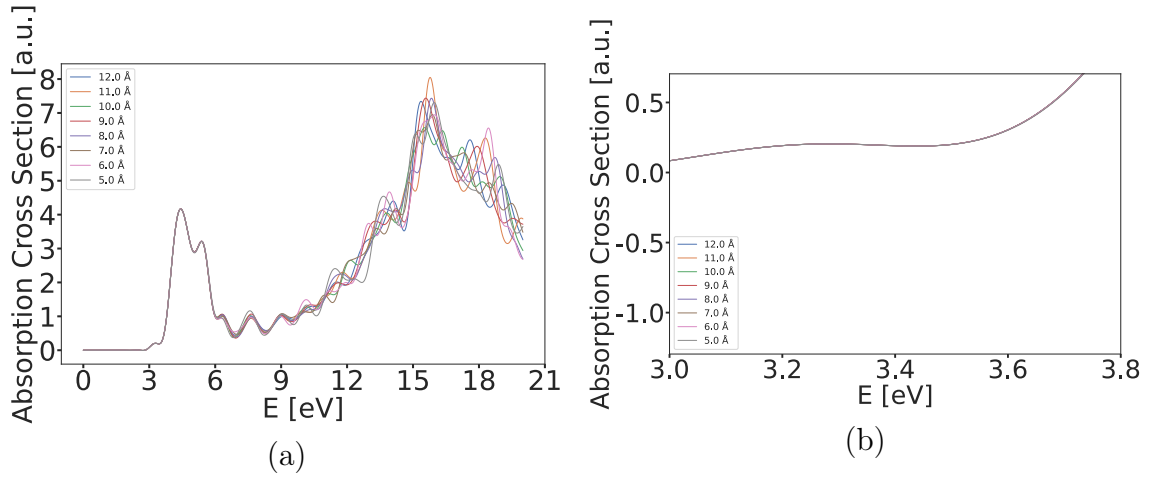
Fig. 46: Convergence of the RT-TDDFT optical spectrum upon excitation with a δ-kick with respect to the simulation box radius for chrysene for the (a) full energy range and (b) zoomed in on the relevant excitation.
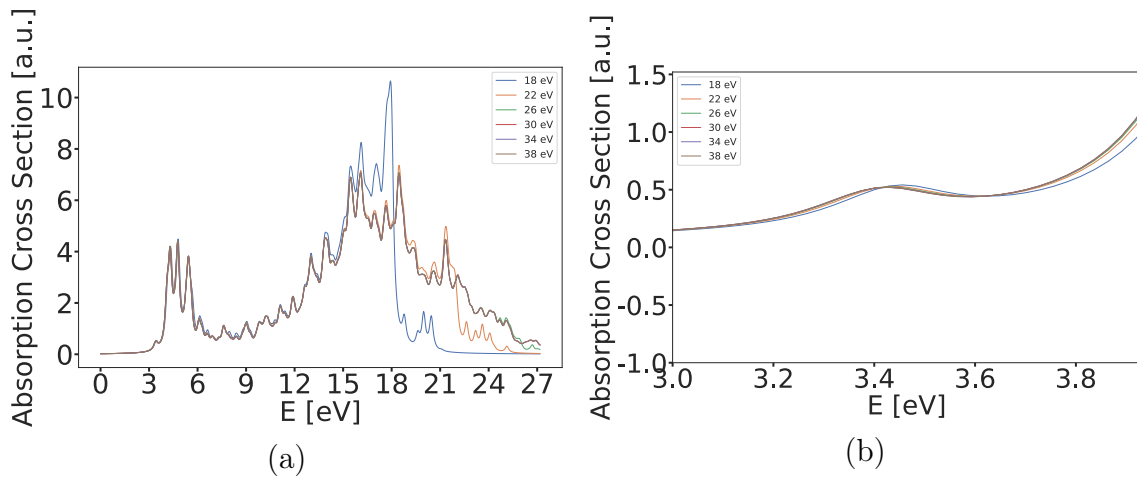
Fig. 47: Convergence of the Casida LR-TDDFT optical spectrum with respect to the Kohn-Sham energy window for chrysene for the (a) full energy range and (b) zoomed in on the relevant excitation.

Picene
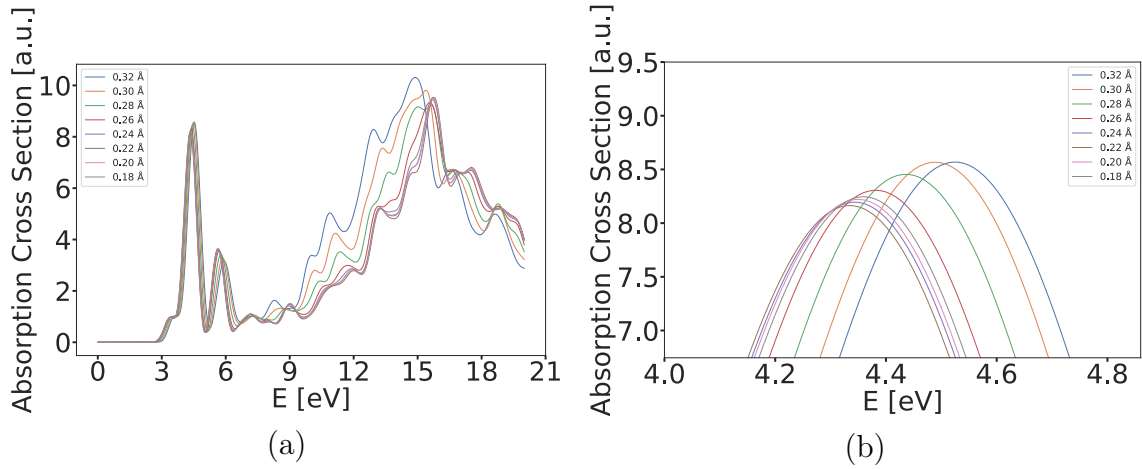
Fig. 48: Convergence of the RT-TDDFT optical spectrum upon excitation with a δ-kick with respect to the grid spacing for picene for the (a) full energy range and (b) zoomed in on the relevant excitation.
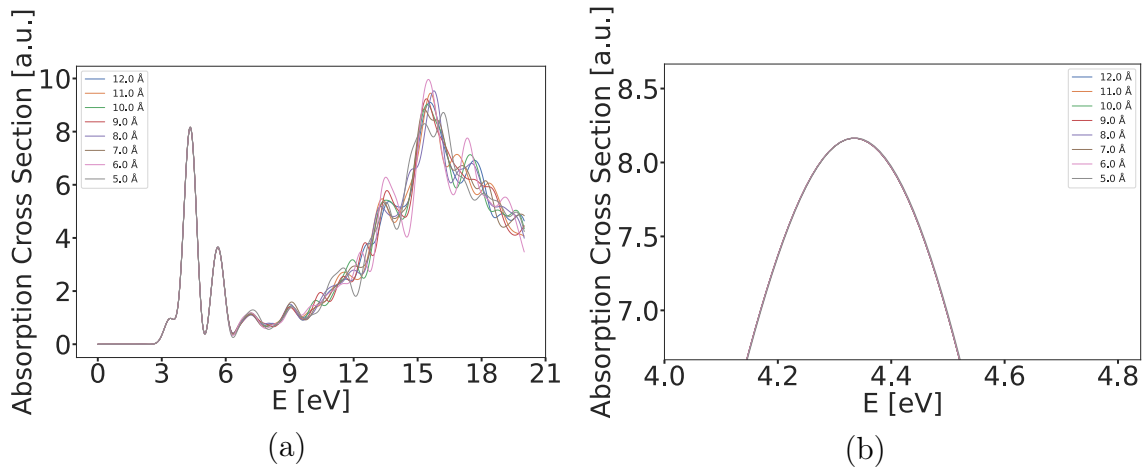
Fig. 49: Convergence of the RT-TDDFT optical spectrum upon excitation with a δ-kick with respect to the simulation box radius for picene for the (a) full energy range and (b) zoomed in on the relevant excitation.

(a)

(b)
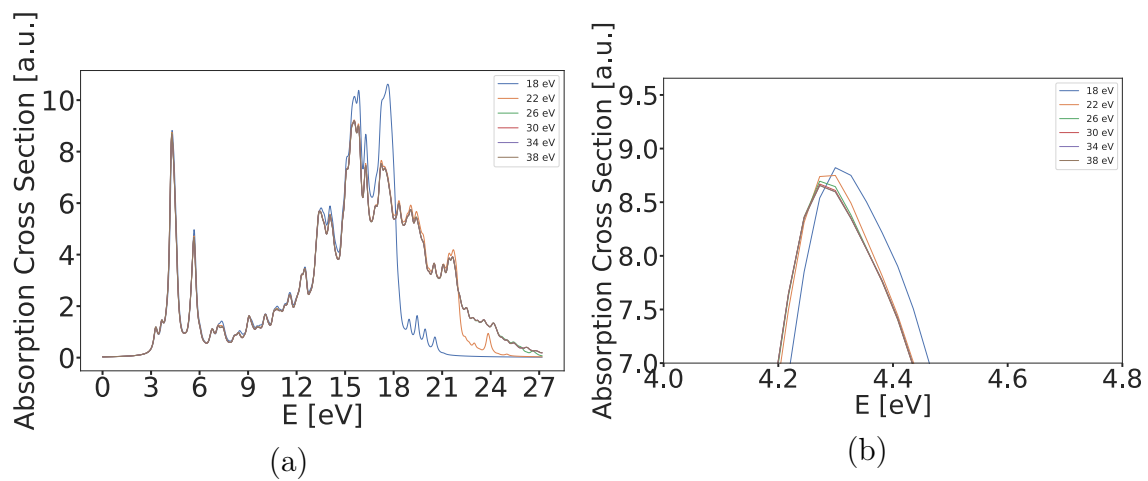
Fig. 50: Convergence of the Casida LR-TDDFT optical spectrum with respect to the Kohn-Sham energy window for picene for the (a) full energy range and (b) zoomed in on the relevant excitation.

List of Figures

List of Tables

References

[1] P. Puschnig, S. Berkebile, A. Fleming, G. Koller, K. Emtsev, T. Seyller, J. Riley, C. Ambrosch-Draxl, F. Netzer, M. Ramsey. *Reconstruction of Molecular Orbital Densities from Photoemission Data.* Science (New York, N.Y.) **326** (2009) 702.
doi:10.1126/science.1176105

[2] P. Puschnig, D. Lüftner. *Simulation of angle-resolved photoemission spectra by approximating the final state by a plane wave: From graphene to polycyclic aromatic hydrocarbon molecules.* Journal of Electron Spectroscopy and Related Phenomena **200** (2015) 193.
doi:https://doi.org/10.1016/j.elspec.2015.06.003. Special Anniversary Issue: Volume 200

[3] M. Dauth, M. Wiessner, V. Feyer, A. Schöll, P. Puschnig, F. Reinert, S. Kümmel. *Angle resolved photoemission from organic semiconductors: Orbital imaging beyond the molecular orbital interpretation.* New Journal of Physics **16** (2014) 103005.
doi:10.1088/1367-2630/16/10/103005

[4] G. Zamborlini, D. Lüftner, Z. Feng, B. Kollmann, P. Puschnig, C. Dri, M. Panighel, G. D. Santo, A. Goldoni, G. Comelli, M. Jugovac, V. Feyer, C. M. Schneider. *Multi-orbital charge transfer at highly oriented organic/metal interfaces.* Nature Communications **8** (2016).

[5] A. Haags, A. Reichmann, Q. Fan, L. Egger, H. Kirschner, T. Naumann, S. Werner, T. Vollgraff, J. Sundermeyer, L. Eschmann, X. Yang, D. Brandstetter, F. Bocquet, G. Koller, A. Gottwald, M. Richter, M. Ramsey, M. Rohlfing, P. Puschnig, F. Tautz. *Kekulene: On-Surface Synthesis, Orbital Structure, and Aromatic Stabilization.* ACS Nano **14** (2020) 15766–15775.
doi:10.1021/acsnano.0c06798

[6] R. Wallauer, M. Raths, K. Stallberg, L. Münster, D. Brandstetter, X. Yang, J. Güdde, P. Puschnig, S. Subach, C. Kumpf, F. Bocquet, F. Tautz, U. Höfer. *Tracing orbital images on ultrafast time scales.* Science **371** (2021) eabf3286.
doi:10.1126/science.abf3286

[7] C. Kern, A. Windischbacher, P. Puschnig. *Photoemission orbital tomography for excitons in organic molecules.* Physical Review B **108** (2023).
doi:10.1103/PhysRevB.108.085132

[8] E. K. U. Gross, R. M. Dreizler, G. E.K.U. Density Functional Theory: An Approach to the Quantum Many-Body Problem, 1991 .
https://api.semanticscholar.org/CorpusID:115933623

[9] D. S. Sholl, J. A. Steckel. Density Functional Theory: A Practical Introduction, 2009 .
https://api.semanticscholar.org/CorpusID:93264228

[10] K. Capelle. *A bird's-eye view of density-functional theory.* Braz. J. Phys. **36** (2002).
doi:10.1590/S0103-97332006000700035

[11] C. Fiolhais. *A Primer in Density Functional Theory*, 2002.

[12] W. Kohn. *Nobel Lecture: Electronic structure of matter—wave functions and density functionals.* Rev. Mod. Phys. **71** (1999) 1253.
doi:10.1103/RevModPhys.71.1253

[13] P. Hohenberg, W. Kohn. *Inhomogeneous Electron Gas.* Phys. Rev. **136** (1964) B864.
doi:10.1103/PhysRev.136.B864

[14] W. Kohn, L. J. Sham. *Self-Consistent Equations Including Exchange and Correlation Effects.* Phys. Rev. **140** (1965) A1133.
doi:10.1103/PhysRev.140.A1133

[15] J. Perdew, K. Schmidt. *Jacob's Ladder of Density Functional Approximations for the Exchange-Correlation Energy.* AIP Conf. Proc **577** (2001).
doi:10.1063/1.1390175

[16] J. P. Perdew, K. Burke, M. Ernzerhof. *Generalized Gradient Approximation Made Simple.* Phys. Rev. Lett. **77** (1996) 3865.
doi:10.1103/PhysRevLett.77.3865

[17] P. J. Stephens, F. J. Devlin, C. F. Chabalowski, M. J. Frisch. *Ab Initio Calculation of Vibrational Absorption and Circular Dichroism Spectra Using Density Functional Force Fields.* The Journal of Physical Chemistry **98** (1994) 11623.
doi:10.1021/j100096a001

[18] A. D. Becke. *Density-functional thermochemistry. III. The role of exact exchange.* The Journal of Chemical Physics **98** (1993) 5648.
doi:10.1063/1.464913

[19] C. Lee, W. Yang, R. G. Parr. *Development of the Colle-Salvetti correlation-energy formula into a functional of the electron density.* Phys. Rev. B **37** (1988) 785.
doi:10.1103/PhysRevB.37.785

[20] J. Heyd, G. E. Scuseria, M. Ernzerhof. *Hybrid functionals based on a screened Coulomb potential.* The Journal of Chemical Physics **118** (2003) 8207.
doi:10.1063/1.1564060

[21] C. A. ULLRICH. *Time-Dependent Density-Functional Theory: Concepts and Applications.* Contemporary Physics **54** (2013) 55.
doi:10.1080/00107514.2012.739657

[22] M. MARQUES, N. MAITRA, F. NOGUEIRA, E. GROSS, A. RUBIO. *Fundamentals of Time-Dependent Density Functional Theory*, Band 837, 2012.
doi:10.1007/978-3-642-23518-4

[23] E. RUNGE, E. K. U. GROSS. *Density-Functional Theory for Time-Dependent Systems.* Phys. Rev. Lett. **52** (1984) 997.
doi:10.1103/PhysRevLett.52.997

[24] K. YABANA, T. NAKATSUKASA, J.-I. IWATA, G. F. BERTSCH. *Real-time, real-space implementation of the linear response time-dependent density-functional theory.* physica status solidi (b) **243** (2006) 1121.
doi:https://doi.org/10.1002/pssb.200642005

[25] M. E. CASIDA. *Time-Dependent Density Functional Response Theory for Molecules*, S. 155–192, 1995.
doi:10.1142/9789812830586_0005

[26] P. WOPPERER, U. DE GIOVANNINI, A. RUBIO. *Efficient and accurate modeling of electron photoemission in nanostructures with TDDFT.* The European Physical Journal B **90** (2016).
doi:10.1140/epjb/e2017-70548-3

[27] R. L. MARTIN. *Natural transition orbitals.* The Journal of Chemical Physics **118** (2003) 4775.
doi:10.1063/1.1558471

[28] L. TAO, A. SCRINZI. *Photo-electron momentum spectra from minimal volumes: The time-dependent surface flux method.* New Journal of Physics - NEW J PHYS **14** (2012).
doi:10.1088/1367-2630/14/1/013021

[29] X. ANDRADE, D. STRUBBE, U. DE GIOVANNINI, A. LARSEN, M. OLIVEIRA, J. ALBERDI-RODRIGUEZ, A. VARAS, I. THEOPHILOU, N. HELBIG, M. VERSTRAETE, L. STELLA, F. NOGUEIRA, A. ASPURU-GUZIK, A. CASTRO, M. MARQUES, A. RUBIO. *Real-space grids and the Octopus code as tools for the development of new simulation approaches for electronic systems.* Phys. Chem. Chem. Phys. **17** (2015).
doi:10.1039/C5CP00351B

[30] U. DE GIOVANNINI, H. HÜBENER, A. RUBIO. *A First-Principles Time-Dependent Density Functional Theory Framework for Spin and Time-Resolved Angular-Resolved Photoelectron Spectroscopy in Periodic Systems.* Journal of Chemical Theory and Computation **13** (2017) 265.
doi:10.1021/acs.jctc.6b00897. PMID: 27981832

[31] I. Hargittai. *Symmetry through the Eyes of a Chemist*, 2009.
doi:10.1007/978-1-4020-5628-4

[32] C. A. Barboza, P. A. M. Vazquez, D. Mac-Leod Carey, R. Arratia-Perez. *A TD-DFT basis set and density functional assessment for the calculation of electronic excitation energies of fluorene*. International Journal of Quantum Chemistry **112** (2012) 3434.
doi:https://doi.org/10.1002/qua.24300

[33] R. C. Maurya, J. Mir. *Molecular Symmetry and Group Theory*. De Gruyter, Berlin, Boston, 2019.
doi:doi:10.1515/9783110635034

[34] P. Puschnig. Organic Molecule Database: a database for molecular orbitals of pi-conjugated organic molecules based on the atomic simulation environment (ASE) and NWChem as the DFT calculator, 2020.
`http://physikmdb.uni-graz.at:5001/`

[35] E. Aprà, E. J. Bylaska, W. A. de Jong, N. Govind, K. Kowalski, T. P. Straatsma, M. Valiev, H. J. J. van Dam, Y. Alexeev, J. Anchell, V. Anisimov, F. W. Aquino, R. Atta-Fynn, J. Autschbach, N. P. Bauman, J. C. Becca, D. E. Bernholdt, K. Bhaskaran-Nair, S. Bogatko, P. Borowski, J. Boschen, J. Brabec, A. Bruner, E. Cauët, Y. Chen, G. N. Chuev, C. J. Cramer, J. Daily, M. J. O. Deegan, T. H. Dunning, M. Dupuis, K. G. Dyall, G. I. Fann, S. A. Fischer, A. Fonari, H. Früchtl, L. Gagliardi, J. Garza, N. Gawande, S. Ghosh, K. Glaesemann, A. W. Götz, J. Hammond, V. Helms, E. D. Hermes, K. Hirao, S. Hirata, M. Jacquelin, L. Jensen, B. G. Johnson, H. Jónsson, R. A. Kendall, M. Klemm, R. Kobayashi, V. Konkov, S. Krishnamoorthy, M. Krishnan, Z. Lin, R. D. Lins, R. J. Littlefield, A. J. Logsdail, K. Lopata, W. Ma, A. V. Marenich, J. Martin del Campo, D. Mejia-Rodriguez, J. E. Moore, J. M. Mullin, T. Nakajima, D. R. Nascimento, J. A. Nichols, P. J. Nichols, J. Nieplocha, A. Otero-de-la Roza, B. Palmer, A. Panyala, T. Pirojsirikul, B. Peng, R. Peverati, J. Pittner, L. Pollack, R. M. Richard, P. Sadayappan, G. C. Schatz, W. A. Shelton, D. W. Silverstein, D. M. A. Smith, T. A. Soares, D. Song, M. Swart, H. L. Taylor, G. S. Thomas, V. Tipparaju, D. G. Truhlar, K. Tsemekhman, T. Van Voorhis, Vázquez-Mayagoitia, P. Verma, O. Villa, A. Vishnu, K. D. Vogiatzis, D. Wang, J. H. Weare, M. J. Williamson, T. L. Windus, K. Woliński, A. T. Wong, Q. Wu, C. Yang, Q. Yu, M. Zacharias, Z. Zhang, Y. Zhao, R. J. Harrison. *NWChem: Past, present, and future*. The Journal of Chemical Physics **152** (2020) 184102.
doi:10.1063/5.0004997

[36] S. S. Zade, M. Bendikov. *Heptacene and beyond: the longest characterized acenes*. Angewandte Chemie **49 24** (2010) 4012.

[37] J. J. Burdett, A. M. Müller, D. J. Gosztola, C. J. Bardeen. *Excited state dynamics in solid and monomeric tetracene: The roles of superradiance and exciton fission.* The Journal of chemical physics **133 14** (2010) 144506.

[38] L. A. Morrison, D. Stanfield, M. Jenkins, A. A. Baronov, D. L. Patrick, J. M. Leger. *High performance organic field-effect transistors using ambient deposition of tetracene single crystals.* Organic Electronics **33** (2016) 269.
doi:https://doi.org/10.1016/j.orgel.2016.03.021

[39] R. Tseng, R. Chan, V. C. Tung, Y. Yang. *Anisotropy in Organic Single-Crystal Photovoltaic Characteristics.* Advanced Materials **20** (2008).

[40] X. Yang, L. Egger, J. Fuchsberger, M. Unzog, D. Lüftner, F. Hajek, P. Hurdax, M. Jugovac, G. Zamborlini, V. Feyer, G. Koller, P. Puschnig, F. S. Tautz, M. G. Ramsey, S. Soubatch. *Coexisting Charge States in a Unary Organic Monolayer Film on a Metal.* The Journal of Physical Chemistry Letters **10** (2019) 6438.
doi:10.1021/acs.jpclett.9b02231. PMID: 31573816

[41] I. A. Fedorov. *First-principles study of band structures of anthracene and tetracene under pressure.* Materials Chemistry and Physics **199** (2017) 173.
doi:https://doi.org/10.1016/j.matchemphys.2017.06.060

[42] F. Plasser. *Entanglement entropy of electronic excitations.* The Journal of Chemical Physics **144** (2016) 194107.
doi:10.1063/1.4949535

[43] A. S. Das, A. R. Nair, A. Sreekumar, A. Sivan. *Approaches to Obtaining Fluorenes: An Alternate Perspective.* ChemistrySelect (2022).

[44] I. Ljubić, A. Sabljić. *CASSCF/CASPT2 and TD-DFT Study of Valence and Rydberg Electronic Transitions in Fluorene, Carbazole, Dibenzofuran, and Dibenzothiophene.* The Journal of Physical Chemistry A **115** (2011) 4840.
doi:10.1021/jp201618a. PMID: 21495706

[45] K. C. Moss, K. N. Bourdakos, V. Bhalla, K. T. Kamtekar, M. R. Bryce, M. A. Fox, H. L. Vaughan, F. B. Dias, A. P. Monkman. *Tuning the Intramolecular Charge Transfer Emission from Deep Blue to Green in Ambipolar Systems Based on Dibenzothiophene S,S-Dioxide by Manipulation of Conjugation and Strength of the Electron Donor Units.* The Journal of Organic Chemistry **75** (2010) 6771.
doi:10.1021/jo100898a. PMID: 20860348

[46] M. A. Karim, Y.-R. Cho, J. S. Park, S. C. Kim, H. J. Kim, J. W. Lee, Y.-S. Gal, S.-H. Jin. *Novel fluorene-based functional 'click polymers' for quasi-solid-state dye-sensitized solar cells.* Chem. Commun. (2008) 1929.
doi:10.1039/B800032H

[47] M. Heeney, C. Bailey, M. Giles, M. Shkunov, D. Sparrowe, S. Tierney, W. Zhang, I. McCulloch. *Alkylidene Fluorene Liquid Crystalline Semiconducting Polymers for Organic Field Effect Transistor Devices*. Macromolecules **37** (2004) 5250.
doi:10.1021/ma049798n

[48] S. Zein, F. Delbecq, D. Simon. *A TD-DFT investigation of two-photon absorption of fluorene derivatives*. Phys. Chem. Chem. Phys. **11** (2009) 694.
doi:10.1039/B808965E

[49] R. Rieger, K. Müllen. *Forever young: polycyclic aromatic hydrocarbons as model cases for structural and optical studies*. Journal of Physical Organic Chemistry **23** (2010) 315.
doi:https://doi.org/10.1002/poc.1644

[50] H. Shin, H. Jung, B. Kim, J. Lee, J. Moon, J. Kim, J. Park. *Highly efficient emitters of ultra-deep-blue light made from chrysene chromophores*. Journal of Materials Chemistry C **4** (2016) 3833.

[51] T.-L. Wu, H. Chou, P.-Y. Huang, C. Cheng, R. Liu. *3,6,9,12-Tetrasubstituted chrysenes: synthesis, photophysical properties, and application as blue fluorescent OLED*. The Journal of organic chemistry **79 1** (2014) 267.

[52] D. Ali, A. S. Verma, F. Mujtaba, A. N. Dwivedi, R. K. Hans, R. S. Ray. *UVB-induced apoptosis and DNA damaging potential of chrysene via reactive oxygen species in human keratinocytes*. Toxicology letters **204 2-3** (2011) 199.

[53] S. S. Vaidya, N. Devpura, K. R. Jain, D. Madamwar. *Degradation of Chrysene by Enriched Bacterial Consortium*. Frontiers in Microbiology **9** (2018).

[54] L. ping Xiao, L. Zeng, X. Yang. *First principles study of the electronic structure and optical properties of chrysene under pressure*. Molecular Simulation **45** (2018) 147 .

[55] E. Posenitskiy, M. Rapacioli, D. Lemoine, F. Spiegelman. *Theoretical investigation of the electronic relaxation in highly excited chrysene and tetracene: The effect of armchair vs zigzag edge*. The Journal of chemical physics **152 7** (2020) 074306.

[56] D. Rai, A. Shukla. A Pariser-Parr-Pople Model Based Study of Optoelectronic Properties of Phenacenes, 2018.

[57] H. Okamoto, S. Hamao, H. Goto, Y. Sakai, M. Izumi, S. Gohda, Y. Kubozono, R. Eguchi. *Transistor application of alkyl-substituted picene*. Scientific Reports **4** (2014).

[58] T. Toccoli, P. Bettotti, A. Cassinese, S. Gottardi, Y. Kubozono, M. A. Loi, M. Manca, R. Verucchi. *Photophysics of Pentacene-Doped Picene Thin Films*. The Journal of Physical Chemistry C (2018).

[59] M. Iwasawa, S. Kobayashi, M. Sasaki, Y. Hasegawa, H. Ishii, F. Matsui, S. Kera, Y. Yamada. *Photoemission Tomography of a One-Dimensional Row Structure of a Flat-Lying Picene Multilayer on Ag(110)*. The Journal of Physical Chemistry Letters **13** (2022) 1512.
doi:10.1021/acs.jpclett.1c03821. PMID: 35133154

[60] T. Huempfner, M. Hafermann, C. Udhardt, F. Otto, R. Forker, T. Fritz. *Insight into the unit cell: Structure of picene thin films on Ag(100) revealed with complementary methods*. The Journal of Chemical Physics **145** (2016) 174706.
doi:10.1063/1.4966200

[61] B. gai Zhai, Y. ming Huang. *Optical Properties and Electronic Structures of Sexithiophene*. Key Engineering Materials **428-429** (2010) 475 .

[62] D. Fichou. *Handbook of Oligo- and Polythiophenes*. Wiley, 1999.

[63] T. Taima, M. Shahiduzzaman, T. Ishizeki, K. Yamamoto, M. Karakawa, T. Kuwabara, K. Takahashi. *Sexithiophene-Based Photovoltaic Cells with High Light Absorption Coefficient via Crystalline Polymorph Control*. The Journal of Physical Chemistry C **121** (2017) 19699.
doi:10.1021/acs.jpcc.7b07953

[64] R. Ameta, S. Ameta. *Chemical Applications of Symmetry and Group Theory*. Apple Academic Press, 2016.

[65] C. Falkenberg, C. Uhrich, S. Olthof, B. Maennig, M. K. Riede, K. Leo. *Efficient p-i-n type organic solar cells incorporating 1,4,5,8-naphthalenetetracarboxylic dianhydride as transparent electron transport material*. Journal of Applied Physics **104** (2008) 034506.
doi:10.1063/1.2963992

[66] X. Han, G. Qing, J. tang Sun, T. Sun. *How many lithium ions can be inserted onto fused C6 aromatic ring systems?* Angewandte Chemie **51 21** (2012) 5147.

[67] C. Braatz, T. Esat, C. Wagner, R. Temirov, F. Tautz, P. Jakob. *Switching orientation of adsorbed molecules: Reverse domino on a metal surface*. Surface Science **643** (2015).
doi:10.1016/j.susc.2015.06.016

[68] K. Yabana, G. F. Bertsch. *Time-dependent local-density approximation in real time*. Phys. Rev. B **54** (1996) 4484.
doi:10.1103/PhysRevB.54.4484

[69] M. Dauth, M. Graus, I. Schelter, M. Wiessner, A. Schöll, F. Reinert, S. Kümmel. *Perpendicular Emission, Dichroism, and Energy Dependence in Angle-Resolved Photoemission: The Importance of The Final State*. Phys. Rev. Lett. **117** (2016) 183001.
doi:10.1103/PhysRevLett.117.183001

[70] D. Popova-Gorelova, J. Küpper, R. Santra. *Imaging electron dynamics with time- and angle-resolved photoelectron spectroscopy.* Phys. Rev. A **94** (2016) 013412.
doi:10.1103/PhysRevA.94.013412

[71] C. Cocchi, C. Draxl. *Optical spectra from molecules to crystals: Insight from many-body perturbation theory.* Phys. Rev. B **92** (2015) 205126.
doi:10.1103/PhysRevB.92.205126

[72] L. Hedin. *New Method for Calculating the One-Particle Green's Function with Application to the Electron-Gas Problem.* Phys. Rev. **139** (1965) A796.
doi:10.1103/PhysRev.139.A796

[73] W. Hanke, L. J. Sham. *Many-particle effects in the optical spectrum of a semiconductor.* Phys. Rev. B **21** (1980) 4656.
doi:10.1103/PhysRevB.21.4656

[74] H. Sun, J. Autschbach. *Electronic Energy Gaps for -Conjugated Oligomers and Polymers Calculated with Density Functional Theory.* Journal of Chemical Theory and Computation **10** (2014) 1035.
doi:10.1021/ct4009975. PMID: 26580181

[75] W. Bennecke, A. Windischbacher, D. Schmitt, J. Bange, R. Hemm, C. Kern, G. D'Avino, X. Blase, D. Steil, S. Steil, M. Aeschlimann, B. Stadtmüller, M. Reutzel, P. Puschnig, M. Jansen, S. Mathias. *Disentangling the multiorbital contributions of excitons by photoemission exciton tomography.* Nature Communications **15** (2024) 1804.
doi:10.1038/s41467-024-45973-x